

University of Alberta

Development Towards a Three-Component Three-Dimensional Micro Velocity Measurement Technique

by

Mona Abdolrazaghi

A thesis submitted to the Faculty of Graduate Studies and Research
in partial fulfillment of the requirements for the degree of

Master of Science

Mechanical Engineering Department

©Mona Abdolrazaghi
Fall 2012
Edmonton, Alberta

Permission is hereby granted to the University of Alberta Libraries to reproduce single copies of this thesis and to lend or sell such copies for private, scholarly or scientific research purposes only. Where the thesis is converted to, or otherwise made available in digital form, the University of Alberta will advise potential users of the thesis of these terms.

The author reserves all other publication and other rights in association with the copyright in the thesis and, except as herein before provided, neither the thesis nor any substantial portion thereof may be printed or otherwise reproduced in any material form whatsoever without the author's prior written permission.

*To my beloved Martin who believed in me, walked with me
in every step of this path, and never left me alone even
when it got so rough*

Abstract

An investigation towards determining the sources of uncertainty of a three-component three dimensional (3C3D) velocity measurement technique has been performed. The concept of the technique is velocity vector calculation based on 3D cross correlation of the intensity volume of positions of particles at a known time interval. Each volume is generated by scanning through depth of a micro-channel with a thin focal plane, capturing images, and stacking them together to build an intensity volume of particles' position. The proposed 3C3D measurement system was used to measure the velocity vector field in mixing, segmented, and porous media micro-flows. It was observed that several system parameters have impact on measurement uncertainty. A Monte-Carlo simulation is developed to investigate the uncertainty affected by these parameters: generating synthetic images of the flow field, applying an extended 3D cross correlation algorithm, followed by a developed 3D elliptical Gaussian peak detection algorithm to calculate flow field.

Acknowledgment

Completing this degree gave me a great opportunity to enhance my knowledge and skills in several academic and non-academic areas. I would like to thank all my professors, colleagues and friends who assisted me in this path. I would like to thank Prof. Larry Kostiuk who provided me the amazing opportunity to lecture Engineering Physics (ENG PHYS 131) in winter 2010 as a principal instructor.

I would like to sincerely thank my mom, Fatemeh Jiriae Sharahi, who inspired me with passion for higher education when I was seven, and my dear supportive dad, Hossein, who taught me to be strong and believe in myself and my opinions. I would like to thank my sister, Azadeh, who is continuously teaching me to tolerate different opinions and my brother, Amir Mohsen, who always opens my eyes to different areas in life and science. I am especially grateful to my lovely partner, Martin Barczyk for his love, patience, support, and encouragement.

TABLE OF CONTENTS

CHAPTER 1: Introduction	1
1.1 Existing 3C3D micro-velocity particle based measurement techniques.....	2
1.2 Ideas behind a new 3C3D mico-velocity measurement system.....	4
1.3 Thesis Organization	6
CHAPTER 2: Experimental set-up and micro-velocity measurement	8
2.1 Introduction.....	8
2.2 Experimental set-up of the proposed 3C3D measurement technique.....	8
2.3 Three-dimensional flow measurements	16
2.3.1 Mixing flow in Tear-Drop channel	16
2.3.2 Two phase flow field	21
2.3.3 Flow in porous media.....	31
2.4 Conclusion	32
CHAPTER 3: Principles of uuncertainty sources of the proposed three-component three-dimensional (3C3D) measurement system	35
3.1 Introduction.....	35
3.2 Review of the uncertainty analysis of measurement systems in the literature	38
3.3 Sources of uncertainty.....	41
3.4 Experiment's conditions:	41
3.4.1 Flow in micro-channel	42
3.4.2 Suspended particles in micro-flow.....	43
3.4.3 Particles in PIV measurement	46
3.5 Experimental set-up:	51
3.5.1 Experimental displacement uncertainty	51

3.5.2 Camera pixel size.....	53
3.5.3 Fluorescent particle Gaussian intensity	53
3.5.4 Pixilation of the particle’s Gaussian intensity	55
3.5.5 Sub-pixel displacement discretization	57
3.5.6 Piezo-electric system	58
3.5.7 Dynamic range in in-plane velocity.....	60
3.5.8 Dynamic range in out-of-plane	64
3.6 Conclusions.....	65
 CHAPTER 4: Perturbation analysis of the proposed Three-component three-	
dimensional (3C3D) measurement system	67
4.1 Introduction.....	67
4.2 Methodology.....	69
4.3 Synthetic intensity volume generation.....	74
4.4 Particle intensity construction.....	74
4.5 Spherical intensity particle.....	78
4.6 Cylindrical intensity particles	79
4.7 Seeded flow field	80
4.8 Three-dimensional cross correlation algorithm	83
4.9 Peak detection	85
4.10 The Monte Carlo simulation	92
4.11 Results.....	94
4.11.1 Effects of particle shape.....	94
4.11.2 Correlation maps	94
4.11.3 Effect of particle diameter	101
4.11.4 Effect of particle density	103
4.11.5 Effect of particle displacement perturbation.....	104
4.11.6 Effect of background noise	105

4.11.7 Effect of noise on optimum particle diameter.....	110
4.11.8 Effect noise on particle density.....	112
4.11.9 Effect of out-of-plane motion	114
4.12 Conclusions.....	116
CHAPTER 5: Conclusions and Future Work.....	119
5.1 Future work.....	124
Appendix A.....	131

List of Tables

Table 2- 1: Specifications of fluorescent tracer experiments ‘particles (Red Fluorescent Polymer Microspheres, Thermo Scientific)	11
Table 3- 1: Objective mass and resonance frequency of Piezo system Jena	61
Table 4- 1: Effect of adding various noise levels to synthetic images on correlation maps ‘peak width for the simulation parameters: $N = 100$, $d_{\tau} = 2.0$ voxel, particle density of 1.1×10^{-3} PPV, $QL = 8$ bits/pixel and $\vec{V} = [10, 0, 0]$ $\mu\text{m/s}$	108

List of Figures

Figure 2- 1: Using the proposed 3C3D technique to (a) image scans in depth (b) constructed intensity volumes by stacking the scanned images	9
Figure 2- 2: Schematic of 3C3D measurement system.....	10
Figure 2- 3: The design of the proposed 3C3D measurement system (a) A solid model of Experimental set-up (b) the current experimental set-up	13
Figure 2- 4: A timing diagram of control signals to trigger the camera in sync with the piezo-objective scanner.....	15
Figure 2- 5: Typical images of the bifurcating flow at a single z-location; (a) raw image, (b) post-processed image ready for correlation with image depth of 8bits/pixels [26].	20
Figure 2- 6: The y component of velocity in pixels from a single volume scan constructed by 100 images and frequency piezo=2 Hz and camera frame rate of 200 fps; (a) Colour map of velocity magnitude (b), streak-lines in 3D [26].	21
Figure 2- 7: Schematic of a segmented flow pattern	22
Figure 2- 8: An image of a bottom plane in a micro-reactor channel (a) the raw image (b) the preprocessed image [36]	27
Figure 2- 9: Planar velocity vector of liquid segment in a single z -plane [36] ...	28
Figure 2- 10: Colour contour images of the out-of-plane component of velocity in a single (A) top plane ($2.5 \mu\text{m}$ above the center of channel) (B) bottom plane ($2.5 \mu\text{m}$ below the center of the channel) [36].....	30
Figure 2- 11: 3C3D velocity vector field in the pore region close to sphere surface employing a 3D cross correlation through two multiple passes that a first pass using a 75% overlaps between interrogation windows with size of $128 \times 128 \times 32 \text{ voxels}$ and the second pass used $64 \times 64 \times 24 \text{ voxels}$ interrogation window with 60% overlaps [39].....	32
Figure 3- 1: Particle intensity displacement projected over the image.....	48
Figure 3- 2: Schematic of the optics of the measurement system.....	54
Figure 3- 3: Sub-pixel planar displacement of particle at definite depth (a) relative origin(0,0,0) (b) (0.25,0,0) pixel (c) (0.5, 0,0) pixel (d) (0.75,0,0) pixel (e) (1,0,0) pixel.....	58
Figure 3- 4: The Gaussian intensity distribution of experimental data obtained from a $1 \mu\text{m}$ particle positioned at depth of $12 \mu\text{m}$ and was discretized by 27 slices that each positioned $1 \mu\text{m}$ apart with the image depth of 8bits/pixels	59
Figure 3- 5: Maximum in-plane velocity by the proposed 3C3D measurement system for $f=200\text{fps}$	63

Figure 4- 1: A conceptual flow map of the Monte Carlo simulation used	70
Figure 4- 2: Schematic of data generate and processing for the Monte Carlo simulation.....	73
Figure 4- 3: (a) Images of a $1\mu\text{m}$ fluorescent particle at $z = -9\mu\text{m}$ below (top) and $z = 23\mu\text{m}$ above focal plane (bottom) (b) constructed 3D Gaussian intensity	75
Figure 4- 4: Gaussian intensity particle (a) 3D shape(b)Image slices at different depths	77
Figure 4- 5: 3D Spherical fluorescent particle.....	79
Figure 4- 6: cylindrical intensity particle.....	80
Figure 4- 7: Two volumes of intensities of the generated particles (Blue: initial, Red: the second positions of the particles).....	82
Figure 4- 8: synthetic images captured at one depth for two intensity volumes (a) 1 st scan (b) 2 nd scan	83
Figure 4- 9: Elliptical Gaussian curve, f , along x -axis fitted at the origin and finding the peak using three-point estimation.....	87
Figure 4- 10: Correlation map in x - y plane for velocity of $[10,0,0]\mu\text{m/s}$ obtained by synthetic images seeded by (a) spherical (b) cylindrical particle intensities at peak x coordinate	96
Figure 4- 11: Correlation maps in y - z plane at detected peak x coordinate for velocity of $[0,0,10]\mu\text{m/s}$ obtained from synthetic images using (a) spherical (b) cylindrical intensity volumes	97
Figure 4- 12: 1D plot of correlation map along depth, z , at x, y detected peak coordinates for velocity of $[0,0,10]\mu\text{m/s}$ for two particle intensity of spherical and cylindrical.....	99
Figure 4- 13 : Correlation maps in x - y plane at detected peak x coordinate for velocity of $[0,0,10]\mu\text{m/s}$ obtained from synthetic images using a 3D Gaussian particle with particle diameter of $d_\tau = 3$ voxel	100
Figure 4- 14: Uncertainty measurement (RMS uncertainty) as a function of particle image diameter, d_τ , with Monte-Carlo simulation parameters: number of simulation runs of $N = 200$, particle density of 1.1×10^{-3} PPV, $QL=8$ bits/pixel, no noise.....	102
Figure 4- 15: Uncertainty measurement (RMS uncertainty) as a function of particle density per voxel (PPV) with Monte-Carlo simulation parameters: $d_\tau = 2.0$ voxel, $QL= 8$ bits/pixel, $N = 200$ and $\vec{V} = [10,0,0]\mu\text{m/s}$, no noise	104
Figure 4- 16: Uncertainty measurement (RMS uncertainty) as a function of perturbed particle image displacement for Monte-Carlo simulation parameters: $d_\tau = 3.0$ voxel, particle density of 1.1×10^{-3} PPV, $QL= 8$ bits/pixel, $N = 200$ and $\vec{V} = [10,0,0]\mu\text{m/s}$, no noise.....	105

Figure 4- 17: Synthetic images at one depth with $d_\tau = 2.0$ voxel (a)without noise and (b): 5% noise	106
Figure 4- 18: Effect of background noise on image intensity signal along one direction for particle image size of $d_\tau = 2.0$ voxel positioned at the center	107
Figure 4- 19: Effect of adding noise to synthetic images on correlation maps in x-y plane (a): without noise (b): with 50% background noise with simulation parameters: $d_\tau = 2.0$ voxel, particle density of 1.1×10^{-3} PPV, QL= 8bits/pixel and $\vec{v} = [10,0,0]$ $\mu\text{m/s}$	109
Figure 4- 20: Effect of adding various noise levels to synthetic images on correlation maps ‘peak reduction along x-axis for simulation parameters: $d_\tau = 2.0$ voxel, particle density of 1.1×10^{-3} PPV, QL= 8bits/pixel and $\vec{v} = [10,0,0]$ $\mu\text{m/s}$	110
Figure 4- 21: Measurement uncertainty (RMS uncertainty) as a function of particle intensity diameter, d_τ , with simulation parameters: $N = 200$, particle density of 1.1×10^{-3} PPV, QL= 8bits/pixel and $\vec{v} = [10,0,0]$ $\mu\text{m/s}$	111
Figure 4- 22: Uncertainty measurement (RMS uncertainty) for various noise levels as a function of particle density per voxel (PPV) with the simulation parameters: $N = 200$, $d_\tau = 2.0$ voxel, QL= 8bits/pixel and $\vec{v} = [10,0,0]$ $\mu\text{m/s}$..	113
Figure 4- 23: Measurement of uncertainty (RMS uncertainty) as a function of out-of-plane displacement with Monte-Carlo simulation parameters: $N = 700$, $d_\tau = 3.0$ voxel, particle density of 1.1×10^{-3} PPV, QL= 8bits/pixel, noise 0%	114
Figure 4- 24: Measurement of uncertainty (RMS uncertainty) as a function of out-of-plane displacement with Monte-Carlo simulation parameters: $N = 700$, $d_\tau = 3.0$ voxel, particle density of 1.1×10^{-3} PPV, QL= 8bits/pixel, noise 5%, 10%, 25%, 50%.....	115

CHAPTER 1: Introduction

There are several three-dimensional (3D) micro flow fields that have the potential to generate a three-dimensional (3D) velocity vector field [1] [2]. This type of flow might be required to enhance mixing, flow separation, or be part of another phenomenon such as dielectrophoretic levitation of particles [2]. There are limited techniques for measuring micro-channel flows with a strong out-of-image-plane motion [3]. Investigating micro-flow fields provides useful information in studying flow motion and the dynamics of suspended particles in the flow to improve mechanical and biological systems and pharmaceutical processes [4]. This could include reducing mixing time and length of the mixing channel, an enhancing oil recovery process in micro-filtration or improving DNA separation process using di-electrophoretic flow field [5]. Therefore, investigating the three dimensional micro-flow fields has motivated the development of a non-invasive, accurate, micro flow field imaging and velocity measurement techniques. Some of the current micro imaging measurement techniques under development that are capable of measuring three component three dimensional (3C3D) velocity are described in the following section.

1.1 Existing 3C3D micro-velocity particle based measurement techniques

Investigation of the velocity vector field of micro-channel flows has been carried out using a number of different techniques in both image acquisition and analysis of data [3]. The flow field is usually seeded with tracer particles that are chosen to be large enough to be observed by the measurement system and small enough to follow the flow. In micro-flow measurement, fluorescent particles are selected as tracer due to avoiding reflection of the surface of the particle as well as high levels of bulk illumination emitted from individual locations of the particles of the region of interest. Image analysis methods that track groups of particles, such as micro-particle image velocimetry (μ PIV), typically measure particle motion only within the image plane [6], [7]. The existing particle based micro-scale velocity measurement techniques including stereo-micro particle image velocimetry (stereo- μ PIV) [8], defocusing [9] and off-focus techniques [10] have been developed to measure the three components of velocity.

To capture the three components of velocity, a stereo imaging configuration based on stereo macro PIV with some differences in the configuration can be used to resolve 3D velocity in a plane. In stereo micro-PIV[11], two or more cameras are located with angle γ (typically $\gamma \approx 10^\circ - 20^\circ$) between each and capture double frame images of the flow field. The illumination is provided by the laser volumetrically to the field of views. This style of illumination causes the large reflection effect; therefore, in order to avoid this

problem, fluorescent particles are seeded in the flow field. There is also a minimum thickness in the laser sheet which is usually larger than the size of micro-channel. The in-plane resolution is defined by the camera pixel size similar to stereo macro-PIV. However, the out-of-plane resolution is defined by the focal plane thickness as oppose to laser sheet thickness in stereo macro-PIV. Focal plane thickness is specified for objective lenses by the manufacturers of the objectives, as well as the other optical characteristics of the measurement system such as magnification and numerical aperture (NA). For an angle $\gamma = 13.8^\circ$, the out-of-plane velocity uncertainty is estimated to be approximately four times higher than in-plane velocity uncertainty [11].

Volume information at discrete locations can be captured using a de-focusing approach to track individual particles in 3D space [9] ,[12]. In this method, a plate with a specified pattern of holes on a mask is placed in the path of the optics that focuses an image onto the camera sensor plane. The out-of-plane distance of a particle, relative to the focal plane of the system is then measured by calculating the distance between the spots created by a single particle. As the pattern of spots from one particle move further from one another, the particle is found further away from the focal plane. This method is, however, limited to low particle density, so that individual particles can be resolved.

Alternatively, off-focus methods can be used with fluorescent particles and the diffraction rings that occur when they are imaged, to determine the three-dimensional particle locations [10], [13], [14]. As particles' distance from the

focal plane increases, diffraction rings around the particle will also increase in size. Calibration can find a linear relationship between the diffraction ring size and the distance from the focal plane, which provides a measure of the out-of-plane particle position.

De-focusing and off-focus techniques are based on tracking individual particles (particle tracking velocimetry, PTV). PTV requires lower particle density and consequently these techniques result in resolving a smaller number of velocity vectors in comparison to tracking group of particles in interrogation region employed in PIV techniques. The limitations of the previous mentioned techniques motivates the idea of developing a new 3C3D measurement technique capable of capturing a higher number velocity vectors using a single camera that provides a larger optical access to the measurement system. In this investigation, a work towards development of this 3C3D measurement system with a single camera is presented.

1.2 Ideas behind a new 3C3D micro-velocity measurement system

This thesis is an exploratory study of a new 3C3D imaging and velocity measurement technique that uses only a single camera to measure the volumetric flow field components. This is based on building the intensity of the seeded particles by scanning through the depth of channel with a thin focal plane and high scanning rate relative to the particles' speed. The captured planar images are stacked into the volumes of intensity. A 3D cross correlation algorithm is applied

to the built intensity volumes that consequently a 3D velocity vector field is obtained. This 3C3D velocity measurement system was employed to measure the 3D flow fields including mixing flow, segmented liquid-bubble flow, and flow in porous media.

Experiments have shown that the proposed 3C3D measurement technique is capable of measuring 3D micro-flow field. However, there exist several issues in order to validate the operation of the technique. The seeded particles fluoresce with a three-dimensional Gaussian intensity that the scanning system captures images of at discrete depths. By stacking these images, the constructed volumetric intensity of a particle appears as a stretched rod of illumination with diffraction rings around it. In this technique, a 3D cross correlation is performed between these constructed rods instead of actual constrained semi-spherical particles.

The first main challenge of this technique is understanding the accuracy of correlating these intensity volumes appearing as a rod of illumination in three dimensional flow measurements. In addition, the nature of scanning through depth and constructing an intensity volume by stacking the slices introduces a distortion in time that intensity volume is constructed. That is due to a time difference between every successive slice during the scanning in depth.

This thesis describes the development of the proposed 3C3D technique. This includes 3D μ -flow field measurement, and validation of the operation of the system using a computational measurement uncertainty analysis using Monte-Carlo simulation using synthetic images of the flow field. There exist several

parameters that can be involved in establishing the accuracy of the measurement system including camera frame and piezo system operating frequencies, particle size, density, and camera white noise in capturing the images. Therefore, in this study, the effect of each parameter is investigated.

1.3 Thesis Organization

The study towards development of the proposed 3C3D technique explains using the technique in measuring several micro-flow fields and observing potential sources of uncertainty in the system, then performing an uncertainty analysis computationally. Therefore, this thesis is documented as follows:

Chapter 2: Experimental set-up and micro-velocity measurement: This chapter contains the description of the proposed 3C3D system's experimental set-up and 3D micro-flow measurement using the 3C3D measurement system. In this chapter, the proposed 3C3D measurement system is experimentally used to measure the volumetric micro-flow field velocity vector field in a mixing flow, segmented bubble-liquid micro-flow, and flow in porous media. Consequently, motivation of uncertainty analysis of this 3C3D measurement system and determining the dynamic range and resolution of the 3D velocity vector field is presented.

Chapter 3: Principles of uncertainty sources of the proposed three-component three-dimensional (3C3D) measurement system: The principle of uncertainty analysis of the proposed 3C3D technique along with the sources of uncertainty in

3C3D velocity measurement including experimental set-up, experimental conditions and processing algorithm are explained in this chapter. Also, a study through determining the maximum and minimum measurable velocity using the proposed 3C3D measurement system is discussed.

Chapter 4: Perturbation analysis of the proposed three-component three-dimensional (3C3D) measurement system: This chapter is devoted to computational perturbation uncertainty analysis of the proposed 3C3D measurement technique using a Monte-Carlo simulation. A set of synthetic images of the flow field are generated and the velocity vector field is calculated using the developed 3D cross correlation algorithm followed by an extended 3D-elliptical Gaussian peak detection. The perturbation analysis is applied to compute the uncertainty of the system related to the parameters of the measurement including particle diameter, particle density, background intensity noise, and out-of-plane displacement.

Chapter 5: Conclusions and future work: The goal of this thesis is to present a working measurement system by known characteristics in terms of the measurement parameters that in this chapter a discussion of this observation is provided, as well as the potentials of the further work towards the development of the proposed 3C3D measurement technique.

Appendix A: This includes the MATLAB code of the developed normalized three-dimensional cross correlation algorithm.

CHAPTER 2: Experimental set-up and micro-velocity measurement

2.1 Introduction

In this chapter, an overview of the proposed 3C3D technique and the experimental set-up are presented. In addition, a discussion in applying the 3C3D measurement system to measure the 3D micro-flow field including mixing flow, segmented flow, and flow in micro-porous media is presented. An aim of this chapter is to identify areas and parameters of the systems that affect the experimental accuracy and dynamic range of the measurement system.

2.2 Experimental set-up of the proposed 3C3D measurement technique

The motivation for development of the proposed 3C3D technique is in capturing the volumetric positions of the seeded particles at a discrete time interval. These subsequence volume scans are cross-correlated using a 3D algorithm to track groups of particles in the flow and generate a velocity vector field. The main challenge of this approach is generating the above mentioned intensity volumes of the seeded particles. In order to achieve this, the focal plane of an infinity-corrected microscope objective is rapidly scanned through the volume of the micro-channel and camera images a 2D slice of the field containing seeded

particles in the flow at defined z -locations shown in Figure 2- 1 (a). The captured time series of slices is reorganized into a volume data set and the 3D intensity locations of particles are constructed as shown in Figure 2- 1 (b).

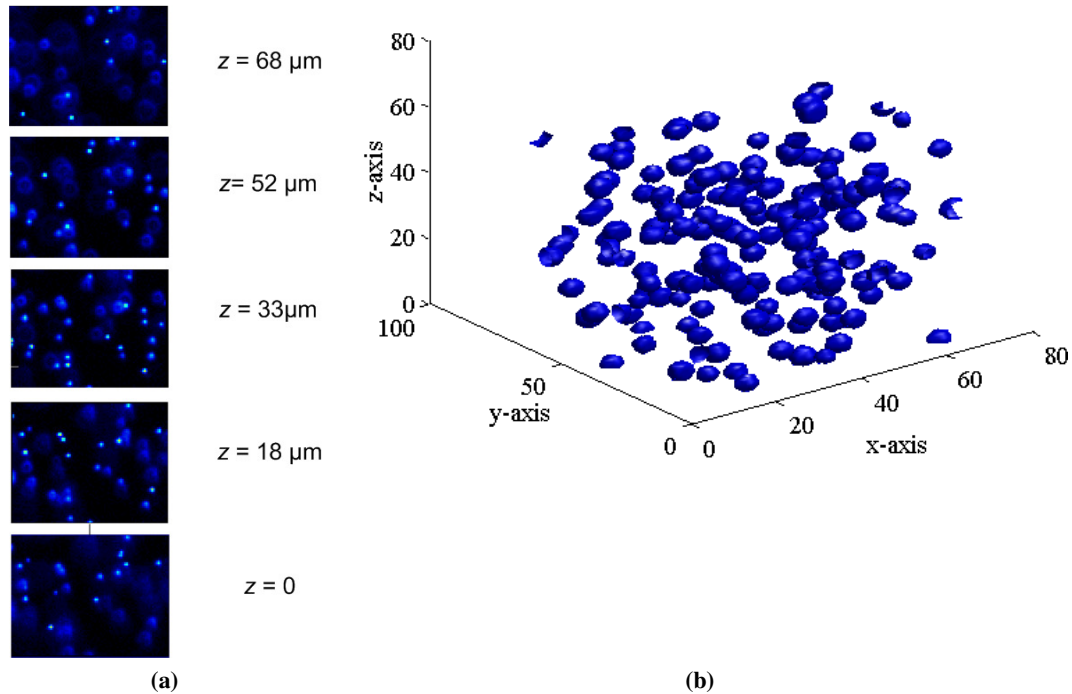


Figure 2- 1: Using the proposed 3C3D technique to (a) image scans in depth (b) constructed intensity volumes by stacking the scanned images

A schematic of 3C3D measurement system similar to an epi-illumination micro-PIV system is shown in Figure 2- 2. Epi-illumination of the region-of-interest will allow access from only one side of the micro-channel for an unobstructed view. This is important in micro-channel flows that use techniques such as dielectrophoresis that require an electrode array to be patterned on one side of the channel. This would interfere with the view for illumination/observation from both sides.

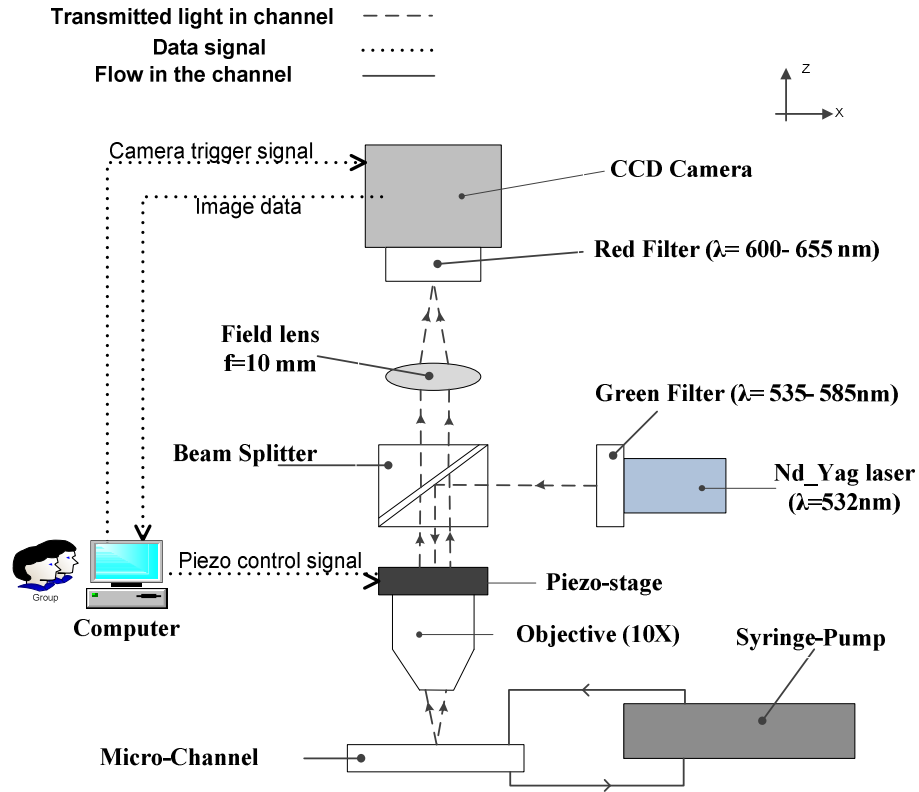


Figure 2- 2: Schematic of 3C3D measurement system

The experimental fluid flow is de-ionized water and fluorescent particles are used for tracking the flow. These are used to remove any reflections in the system, as well as having the benefit of reducing particle size to sub-micron to reduce disturbance in the flow field with high fluorescent light for the field of view. The illumination of system is provided by a CW laser light source that the laser wavelength matches the wavelength of the excited fluorescent particles. The laser used in the experiments is an Nd-YAG laser with wavelength of $\lambda = 532(+/-1) \text{ nm}$ (LRS-0532-PFW-02000-01, Laserglow Technologies). The fluorescent seed particles are Rhodamine coated in latex that fluoresce at

wavelength range of 600nm (Red Fluorescent Polymer Microspheres, Thermo Scientific), the specification is given in Table 2- 1 . This type of fluorescent particles are particularly being used due to having a higher wavelength than laser excitation wavelength which results in providing spectral separation of the laser and fluorescence signals in the collected images.

Table 2- 1: Specifications of fluorescent tracer experiments ‘particles (Red Fluorescent Polymer Microspheres, Thermo Scientific)

Manufacturer	Thermo Scientific
Model	R100
Absorption wavelength	532nm
Emission wavelength	612nm
Size	1 μ m
Material	Polystyrene
Density	1050 kg/m ³
Refractive index	1.59
Nominal size distribution	<5%

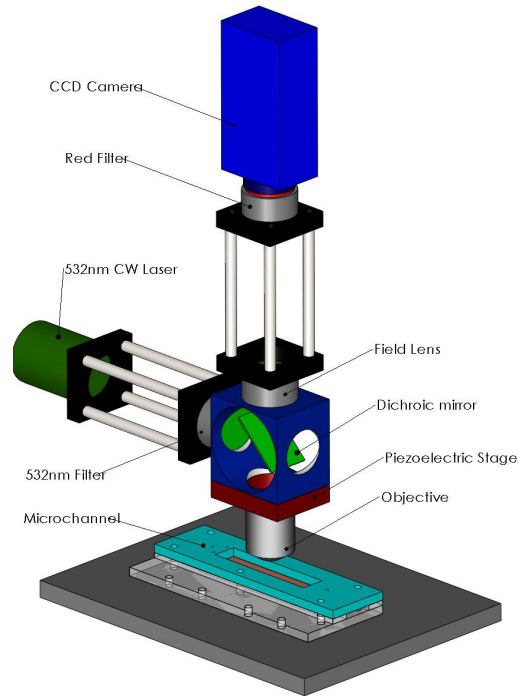
There exist two filters and a dichroic mirror in the measurement system to allow the fluorescent signal to pass through to the camera and to reduce other background noise and increasing the signal to noise ratio. Laser line green filter is used to allow the 85% of the laser light with wavelengths between 535-585 nm.

This filter also ensures that any other light that might be received by the particles is in the range of exciting the fluorescent particles. The dichroic mirror is positioned with the angle of 45° normal to path of the light. This mirror reflects the wavelength of light below 600nm to the micro-channel. A red filter in front of camera allows only the fluorescent signal (wavelengths 600-655 nm) from particles to be transmitted to the camera.

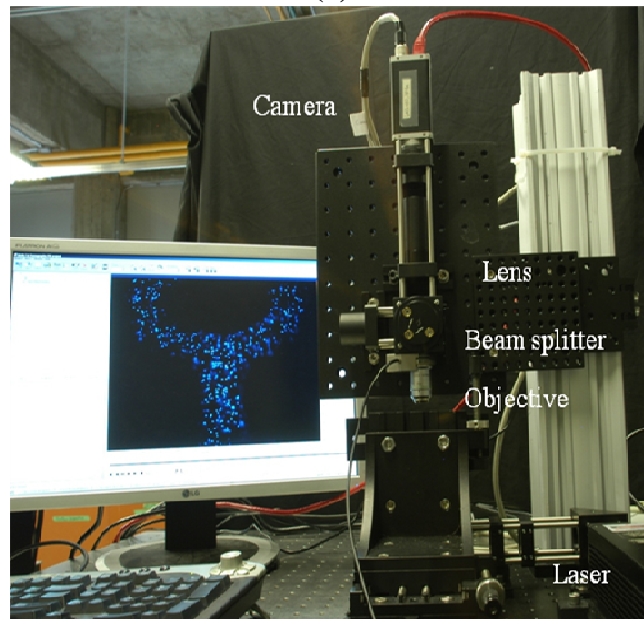
The technique in determining the depth position of the particles flowing in the micro-channel is provided by a piezo electric stage (PZ100, Piezosystem Jena Inc). The piezo is connected to infinitely-corrected objective (Apo-Plan 10x, Olympus with long focal plane of 10.6 mm) that moves a thin focal plane ($\approx 8 \mu\text{m}$ through the depth of channel (z)). The planar images (x - y) are collected at discrete z locations by locking the camera trigger signal to the voltage signal controlling the position of piezo stage. This arrangement allows movement of the focal plane of up to $100\mu\text{m}$. An 8-bit CCD camera (Pioneer piA640-210gm, Basler Vision Technologies) with a sensor size of 640×480 pixels, capable of capturing the images at 210 fps using the full resolution is employed in this system. The field of view of the system with the above mentioned optics is $\approx 400 \times 300 \mu\text{m}^2$.

A solid model (SolidWorks Corp 2010) of the design of the system in Figure 2- 3(a) shows the 3D schematic of this measurement system. However, the current design of the system is shown in Figure 2- 3 (b). The reason for

changing this set-up is for providing more illumination directly to the micro-channel without losing any energy through dichroic mirror.



(a)



(b)

Figure 2- 3: The design of the proposed 3C3D measurement system (a) A solid model of Experimental set-up (b) the current experimental set-up

In every scan of the region-of-interest, images are collected at the same z position to allow quantitative reconstruction of particle positions. To achieve this, timing signals that lock camera acquisition to a precise position of the piezoelectric stage were used. A timing synchronization diagram in Figure 2- 4 shows the relationship between the camera trigger signals and piezo control signal used to position the stage. A pulse train has been used as a trigger signal for image acquisition and a saw tooth control signal for controlling the position of the piezoelectric stage. The total number of images (N) is collected over a single ramp of the stage to produce a single scan of the focal plane through the volume of interest. However, in order to reduce the effect of the abrupt transition of piezo position, a round saw tooth control signal is used during the experiment. However, the round saw tooth trigger signal of piezo stage reduces the effective number of the collected images describing a volume in a single scan. Acquiring the images and generating and synchronizing the control signals are performed through custom software (LabWindows CVI 9.0, National Instruments).

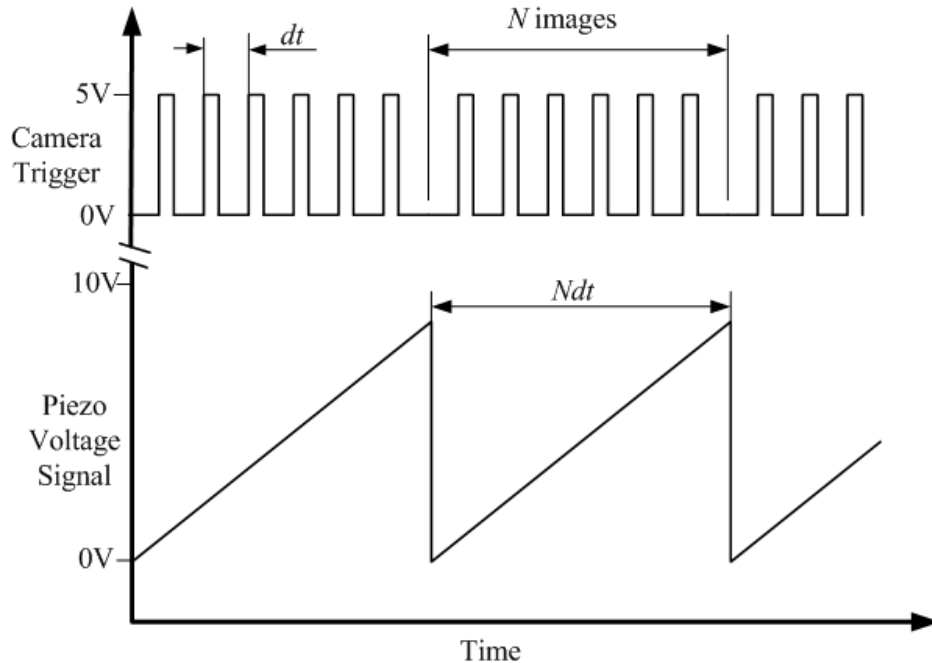


Figure 2- 4: A timing diagram of control signals to trigger the camera in sync with the piezo-objective scanner

The sequence of images is reconstructed into a single volume. Two consecutive scanned intensity volumes are cross-correlated using a series of image processing to improve the collected intensities of the particles, followed by a 3D cross correlation algorithm to track groups of particles in the flow using commercial software (DaVis 7.4 and DaVis 8.06, LaVision GmbH).

Image processing is applied to the collected images built the intensity volumes. The background noise is removed first by a non-linear Gaussian filter by subtracting the sliding minimum of the image intensity over a window size of 3×3 pixels and then using a linear filter to subtract the rest of noise (typically 50 levels). Then, the intensity of the images improved by multiplying the intensity of the images by a constant intensity (usually 30 levels intensity), and smoothing the image intensity by the Gaussian intensity 3×3 pixels .

The cross correlation is performed between every interrogation volumes in three passes with a predefined overlap (typically 50%) between every neighbor interrogation volumes. This process is carried out through three different decreasing size of the interrogation window, and eventually peak detection is performed and the velocity vector field is obtained. The advantage of running the process with three decreasing size of interrogation window is in refining the velocity vector field in smaller regions and increasing the number of the velocity vectors.

2.3 Three-dimensional flow measurements

The proposed 3C3D measurement system was used to measure the flow field in three types of micro-flows including a tear-drop mixing flow, a segmented flow and flow in porous media.

2.3.1 Mixing flow in Tear-Drop channel

Mixing of fluids at the micro-scale can be achieved using active or passive approaches. In active mixing, the mechanism is an external force that agitates the flow to stir and mix it. Mixer design methods based on the active approach use external forces such as dielectrophoretic [15] or centrifugal motion. Piezoelectric actuators (PZT) have been used to stir flow by actuating an oscillating diaphragm [16]. Mixing the fluid based on electro-hydrodynamic (EHD) forces is performed for fluid flows with different electrical properties by inducing an electric field to

the flow field [15]. Magneto-hydrodynamic (MHD) has also been used for mixing fluids using Lorenz forces produced by applying a DC voltage to magnetic field [17]. Pressure perturbations can be developed by stretching and folding the flow with a design that uses a side channel that generates chaotic advection and improves mixing flow [18]. All the above mixing processes can generate a 3D flow that is a function of the applied forces [1].

Passive micro-mixers are based on properties of the flow injection (time-position) and channel geometry. These mixers have higher reliability and less cost relative to active mixers [19]. There are three main methods of passive mixing; fluid lamination, planar mixing, and chaotic mixing. In fluid lamination mixing, the mixer increases the material interface through fluid lamination [19]. The planar mixing channels are 2D channels [20] design and are mostly circular in shape [21]. These channels are specially designed for relatively high Reynolds numbers ($Re=100$) and they work poorly at low Reynolds numbers. Chaotic mixers have a 3D design and enhance fluid mixing by generating chaotic advection. Chaotic advection in 2D (active mixer) or 3D (passive mixer) is a time-periodic flow. Some other techniques for mixing are based on utilizing surface tension [22] such as serpentine channels. Serpentine or twisted channels are applied in mixing based on chaotic advection and at a moderate Reynolds number to create a 3D flow field. However, at low Reynolds number ($Re < 1$), a 2D velocity vector field is often observed in which no chaotic advection can be generated. Chaotic advection can only be achieved in low Reynolds numbers

using certain channel designs, such as tear-drop channels [23] where there is a sequence of flow splitting and recombining. The aim in this design is to reduce the mixing length of the flow. Both segmented flow in serpentine channels and mixing flow in tear-drop channels generate 3D flow field that is due to the nonlinear behavior of the flow which has been observed in direct numerical simulation [24]. Inherent in each of these approaches to enhance mixing is an aim to introduce all three components of the flow.

Description of the flow channel

To explore the experimental technique, a tear-drop mixing micro-channel (FC_Sw11, Micronit Company Enschede, The Netherlands) is studied. This channel has been used for generating a mixing field [1] that has strong velocity components in all three directions [25]. This is a triple-layer micro-mixer chip where the flow is divided and recombined in the $x-y$ plane and flows between three levels in the z -plane. This chip can be used for mixing flows with Reynolds numbers ($Re < 100$) and Peclet numbers (10^5). The mixing technique is based on splitting and recombining the two streams of fluid using several mixing channels located at different levels. The micro-mixer chip used here is made of borosilicate glass with channel width of $200\ \mu\text{m}$ and channel depth of $150\ \mu\text{m}$ with trapezoid cross section. For the size of the chip used, it has a total internal volume of $1\ \mu\text{l}$.

Data processing and results

A typical gray level data image (0-255 levels) from a single plane (a single z -level) using a false RGB colour map is shown in Figure 2- 5(a), where particles are flowing from bottom-to-top. Particles appear as bright pixels, typically accompanied by a halo of fluorescent noise. Image preprocessing is required to be applied to the images so that the background noise is reduced and sharp particle intensity is determined. Masking is used to remove all noise and other data where no flow is present. In order to remove background noise and increase image contrast, a 10 level intensity deduction from images followed by a peak normalization of a range of 30 pixels is performed. Pixel intensities were then increased 20 times to increase contrast. The resulting image is shown in Figure 2- 5(b), which highlights particles at discrete locations. Raw images were saved in a time series and were re-constituted into a volume record of the particles positions from individual scans. These volumes were then cross-correlated using a 3D algorithm with commercial software (DaVis 7.4, LaVision GmbH). The correlation is performed in three passes with decreasing correlation window sizes ($64 \times 64 \times 64$, $64 \times 64 \times 32$ then $32 \times 32 \times 32$, each with 75% overlap).

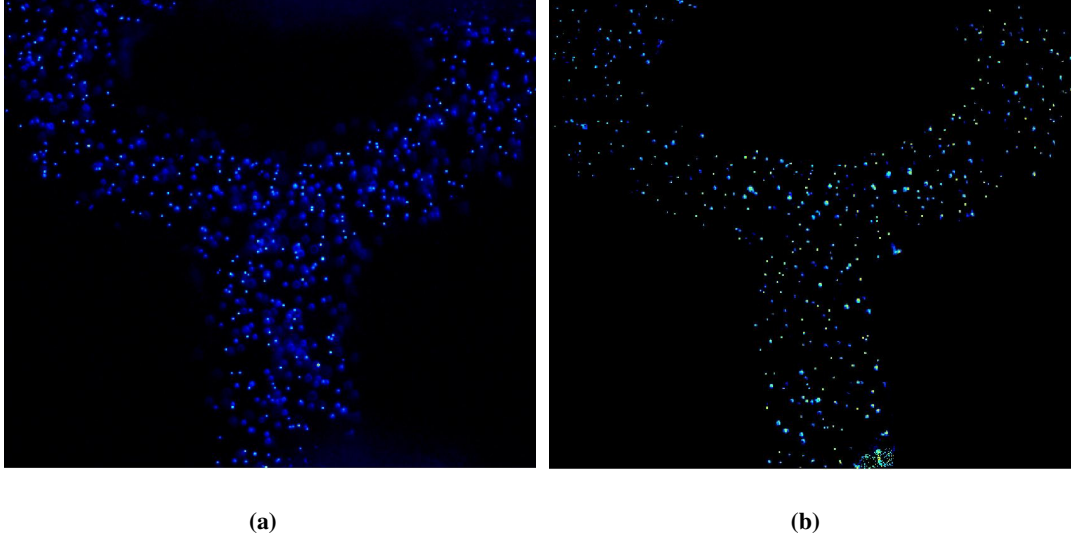
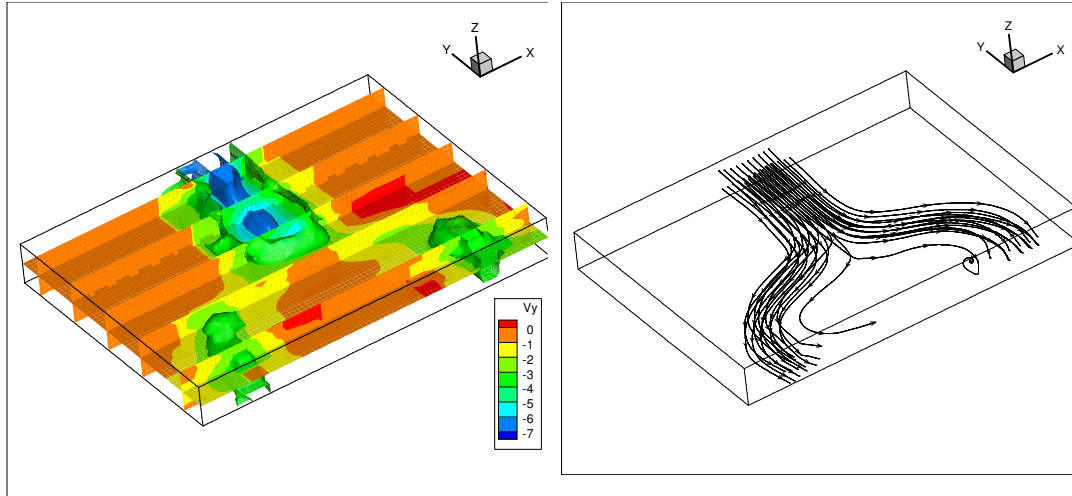


Figure 2- 5: Typical images of the bifurcating flow at a single z-location; (a) raw image, (b) post-processed image ready for correlation with image depth of 8bits/pixels [26].

A computed velocity field from a single volume scan of data is shown in Figure 2- 6. Here, the flow is from top-left to bottom-right. In Figure 2- 6(a), a colour contour map of the y-component of velocity in pixels shows a high velocity region at the centre of the channel before the bifurcation. There is a decrease in net velocity after the bifurcation to maintain volume flow rate. The 3D nature of the flow is shown as streaklines in Figure 2- 6(b). From this single scan, a near-instantaneous representation of the 3D flow field is captured [26].



(a)

(b)

Figure 2- 6: The y component of velocity in pixels from a single volume scan constructed by 100 images and frequency piezo=2 Hz and camera frame rate of 200 fps; (a) Colour map of velocity magnitude (b), streak-lines in 3D [26].

2.3.2 Two phase flow field

In micro-fluidic flow scenarios, segmented flow is a unique situation of two phase flow where the flow is divided into discrete regions of typically gas and liquid. Liquid segments are interconnected through menisci in the channel corners and thin liquid films are apparent at the walls [27]. An example schematic of the segmented flow is shown in Figure 2- 7. No-slip at the wall is typically [28], but not always observed [28] in micro-channel flows. As a liquid segment translates forward, the zero-slip condition results in a transport of fluid along the channel centerline at approximately twice the bulk velocity of the segment to maintain the continuity. As a result, the liquid flow is three-dimensional in nature with high vorticity, which can be a valuable phenomenon in micro-fluidic applications where

fast mixing is required. Cross-stream mixing in single phase micro-channel flows is typically dominated by diffusion only because the Reynolds number is low.

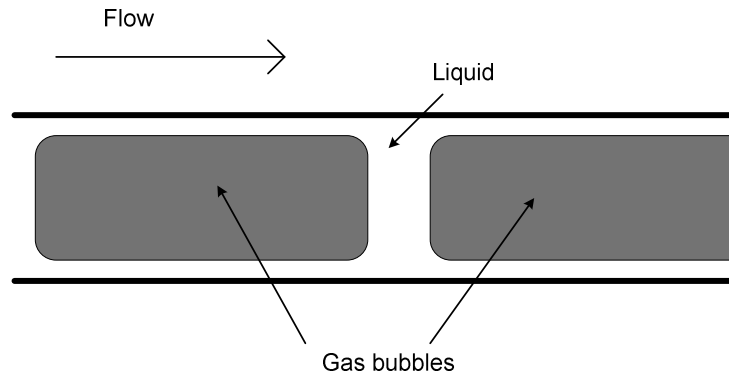


Figure 2- 7: Schematic of a segmented flow pattern

Flow patterns in two phase flows can be divided into five different main types; bubbly, wedging, slug, annular, and dry flows [27]. Each mode presents itself depends on liquid and gas flow rates and fluid and channel properties. Often these flows are characterized by the value of the parameter α described by:

$$\alpha = \frac{Q_L}{Q_L + Q_G} \quad (2- 1)$$

Here, Q_L is the flow rate of liquid and Q_G is the flow rate of gas and the parameter α describes the ratio of liquid volume flow rate to the total volume flow rate. Starting from α equal to unity, the transition from bubbly to wedging occurs at $\alpha \sim 0.75$. The wedging to slug transition is at $\alpha \sim 0.2$ and the slug annular transition happens at $\alpha \sim 0.04$. For $\alpha \sim 0.005$, the annular to dry transition is observable [27]. In order to investigate a segmented flow pattern inside of the gas-

liquid bubbles, either slug or wedging flow needs to be generated. Therefore, the value of α has to be between 0.2 and 0.75.

Experimental techniques for studying multi-phase flow at the micro-scale have been developed in various spatial and temporal resolutions. Microscopy techniques, such as bright field, fluorescent, and confocal microscopy have been used to measure the 2D, and 3D components of the velocity. In the fluorescent microscopy category, the phase distribution and the fluid interface in 2D is obtained by fluorescently labeled particles in the liquid phase of the segmented flow with spatial resolution $\sim 1\ \mu\text{m}$. In this method, the entire depth of the micro-channel is illuminated by the laser, and a camera captures the images synchronized with laser. The temporal resolution has been up to 7 ns, by using a pulsed Nd:YAG laser. Bright field microscopy is a popular option with direct optical access to the micro-channel that provides 2D information of the flow field. The spatial resolution of this method is $\sim 1\ \mu\text{m}$ and the temporal resolution is varied between 0.2 – 33 ms[29].

Temporal resolution can be enhanced by utilizing a high speed digital camera and by replacing the light source of microscope with a stroboscopic source [29]. Confocal microscopy is the other method that measures the flow velocity in 2D. In order to measure 3D velocity vector field, the planar images are captured in slices through the volume. However, due to the low 3D temporal resolution of this technique, confocal microscopy has limited application in 3D measurement of segmented flow [29].

Tomographic techniques such as nuclear magnetic resonance imaging (MRI) are both powerful, though expensive, means to acquire 3D velocity vector field. It has been especially used for flow fields that direct optical access is not available. For example, measuring the flow field inside of monolith reactors [30]. X-ray tomographic microscopy (XTM) is another technique to measure 3D flow velocity vector field. The obtained spatial resolution for a 10^3 mm volume is $4\ \mu\text{m}$, however, the temporal resolution varies between 10 min-2 hrs. This technique has had applications in biomedical multiphase flow such as bone marrow, and cells [31], [32].

Total internal reflectance (TIR) sensor is a method for measuring flow velocity in 1D. This technique is mainly useful for a channel where optical access to the flow is not available. The approach is limited to 1D and has limited applicability to investigating segmented flows [33], [34].

Velocity measurement techniques based on PIV offer an opportunity to experimentally investigate the complex flow field of a segmented flow. In the first developed micro-PIV system for studying segmented flow [35], the field-of-view was illuminated by Nd:YAG pulsed laser and images were captured with a CCD camera. In this experiment, 2D recirculation motion was observed in streamline contours of a segmented flow. This method is considered a challenging approach to observe this type of flow due to the different refractive indices of light at the interface of the two phases of the flow. At the micro-scale, the formation of the micro-bubbles is dependent on surface tension and the regularity of the surface of

the channel. Therefore, μ PIV is a more suitable method to study the multi-phase flow in the body of the liquid slug rather than the liquid-gas interface in a micro-scale segmented flow [35].

Description of the flow channel

A serpentine micro-reactor (R50.332.2: B5130-8155:B4, Micronit Company Enschede, The Netherland) has been used to generate the segmented flow with the cross section of the inverted “D”. The liquid and gas are injected into separate inlets that feed the serpentine channel. Both liquid and gas flow rates are controlled using separate syringe pumps (PHD 2000, Harvard Apparatus). The channel is $w = 150 \mu\text{m}$ wide, $h = 20 \mu\text{m}$ depth and 332 mm long and has an internal volume of $0.28 \mu\text{l}$. To track the flow, $1 \mu\text{m}$ fluorescent tracer particles (Red Fluorescent Polymer Microspheres, Thermo Scientific R0100) are seeded into the liquid stream.

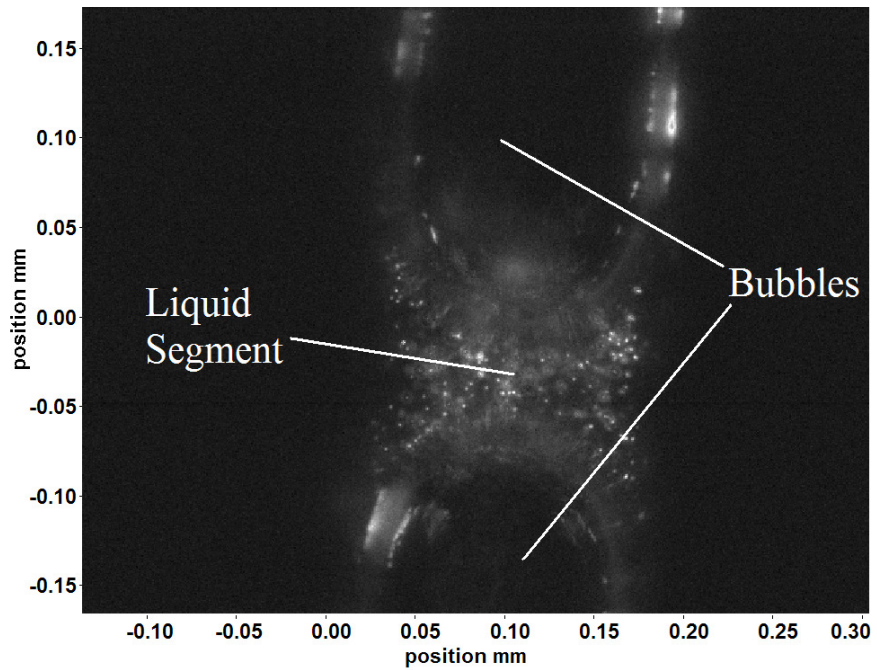
Data processing and results

The liquid flow generated by the syringe pump, with the velocity of the $0.01 \mu\text{l/hr}$ and the gas flow rate $1 \mu\text{l/hr}$ which results in $\alpha \sim 0.01$ that is a slug segmented flow. These low flow rates were chosen because of the limited frame rate on the camera. A set of 1000 images camera frame rate of 200 fps giving 100 images per scan with a scanning frequency of 2 Hz were captured. Figure 2- 8(a) illustrates a raw image at a single z-level of the segmented flow that flow passes

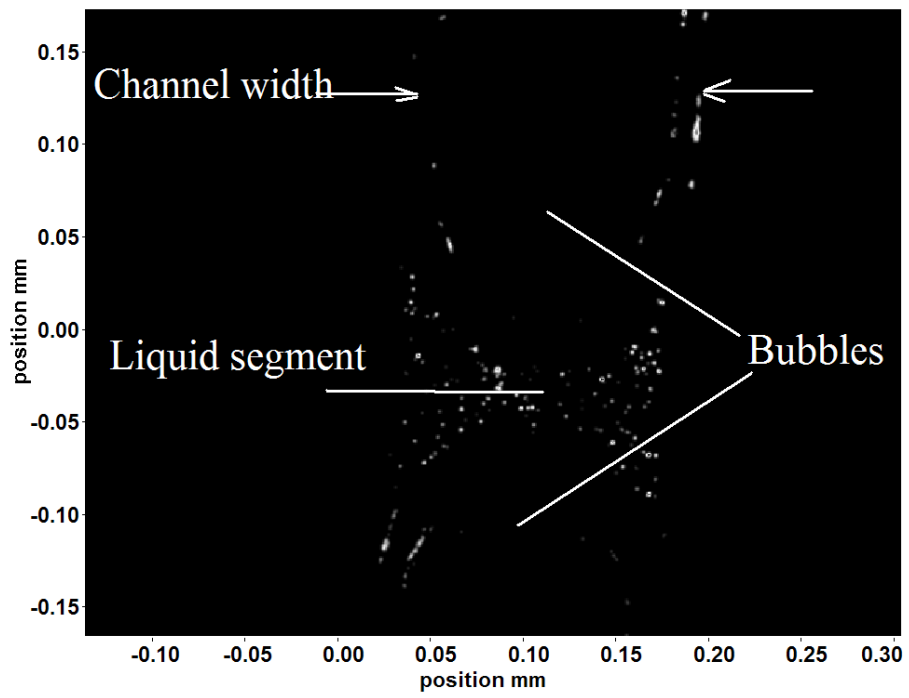
through two generated bubbles in the channel. The sharp bright particles are in focus and the particles surrounded with the halo are out of focus, or in other words are not located on the same z plane. The image processing was carried out in commercial software, (DaVis 8.0.0, LaVision GmbH) to sharpen tracer particle images. The corresponding processed image is shown in Figure 2- 8(b).

Several sets of image pre-processing were performed to remove the background noise and increase the image intensity. First, the background noise is removed by subtracting the sliding minimum of the image intensity over a window size of 3×3 pixels. The rest of the noise was removed by a high pass linear filter with the constant factor of 50 intensity to increase contrast in the image. The image intensity was increased by the factor of 15 counts to increase the contrast in the image. As a last preprocessing step, a Gaussian linear filter for normalization of the image intensity was applied to produce Figure 2- 8(b).

As the images are stored in a time series, the images were re-ordered into single volume scans. These are then interleaved into double frame volumes for correlation processing. The double frame volume is processed using a 3D cross-correlation algorithm to determine particle displacements in 3D (LaVision DaVis 8.0 GmbH). The correlation was performed in four passes with decreasing correlation window sizes; two passes with $64 \times 64 \times 32$ with overlap of 50% then two more passes with $32 \times 32 \times 24$, with 70% overlap.



(a)



(b)

Figure 2- 8: An image of a bottom plane in a micro-reactor channel (a) the raw image (b) the preprocessed image [36]

Figure 2- 9 shows an example vector field of the flow from the mid-plane of the flow channel. The flow near the walls has a higher velocity than the flow at the center of the channel. This result is confirmed by continuity that for the constant mass flow rate, as the cross section area reduces the flow field velocity increases and vice versa. In the case shown here, the bubbles remain stationary in the flow and liquid passes around the bubbles. It is observed that flow treats the immobile bubble as a rigid surface with a slip boundary condition.

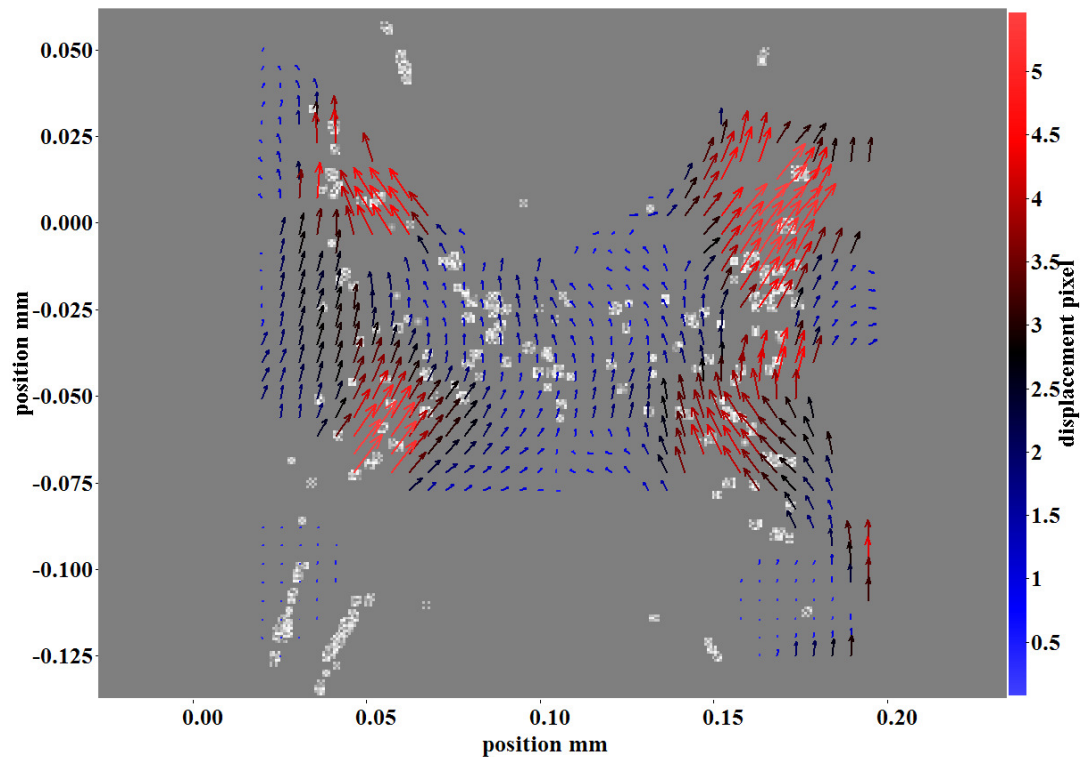
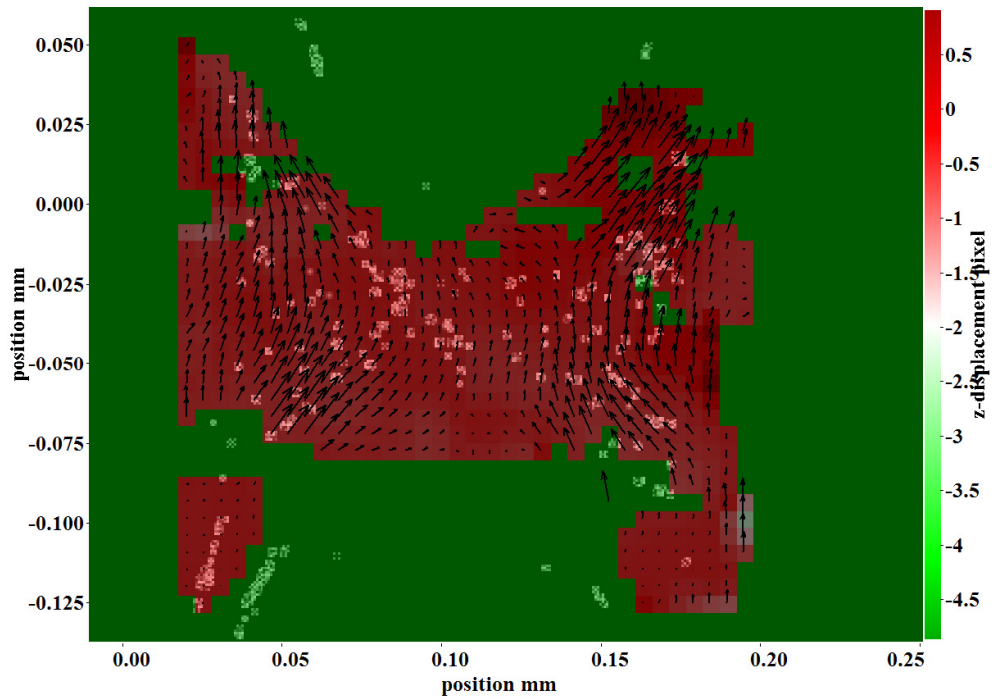
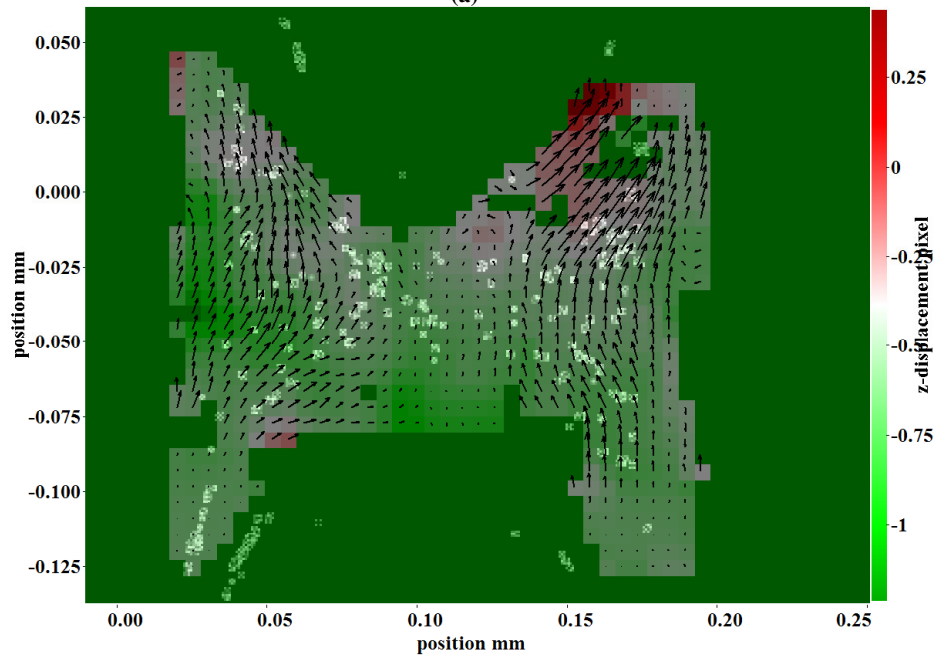


Figure 2- 9: Planar velocity vector of liquid segment in a single z -plane [36]

Figure 2- 10 shows the out-of-plane component of the velocity with overlaid in-plane vectors at a top plane in Figure 2- 10 (a) and the bottom plane in Figure 2- 10 (b) of the flow channel. The sign of the out-of-plane component of the flow velocity at the top measured plane ($2.5 \mu\text{m}$ above the center of the channel) is positive indicating that the flow is passing over the top of the bubble. A corresponding opposite sign is observed in bottom most measured ($2.5 \mu\text{m}$ below the center of the channel) plane. This flow field indicates that the flow finds its way around the stationary bubble. As the bubbles are stationary, the flow accelerates into the shape between gas bubbles. The flow then separates to pass over the bubble in a 3D motion. Highest velocities are seen where the flow passes between the gas bubble and the wall of the channel [36].



(a)



(b)

Figure 2- 10: Colour contour images of the out-of-plane component of velocity in a single (A) top plane (2.5 μm above the center of channel) (B) bottom plane (2.5 μm below the center of the channel) [36]

2.3.3 Flow in porous media

Understanding flow field in porous media provides useful information in oil recovery from reservoir and fuel cells that fluid flow passes through a porous matrix. The three-dimensional nature of the flow in porous media [37] motivates the idea of measuring the velocity vector field using the proposed 3C3D measurement technique.

The micro-channel used in this experiment is made of acrylic based photopolymer plastic (Fullcure, 720) with 16 μm layers. The internal dimensions of each channel are 14.5 \times 4.5 \times 4.5 mm³. Micro-glass beads of nominal size 400 μm are packed in the micro-channel. The flow is seeded with fluorescent tracing particle of 2 μm size (Thermo scientific, R0200) that flows through channel and filters using a syringe pump (PHD 2000, Harvard Apparatus) to drive the flow into the flow cell at a flow rate of 1 $\mu\text{l}/\text{min}$. Optimum seeding density is obtained by adding 2 ml of an aqueous solution of tracing particle to 20 ml of de-ionized water [38].

The 3C3D system scanned through the depth five times and captured 100 images in each scan. Each set of images in one scan built a volume of intensity of particles and individually processed by subtracting a background noise of through using a non-linear subtract sliding minimum algorithm. The intensity of the images are increased 40 times and uniformed by using a 3 \times 3 Gaussian smoothing filter. An instantaneous vector plot generated after post processing of data from two scans is shown in Figure 2- 11 [39].

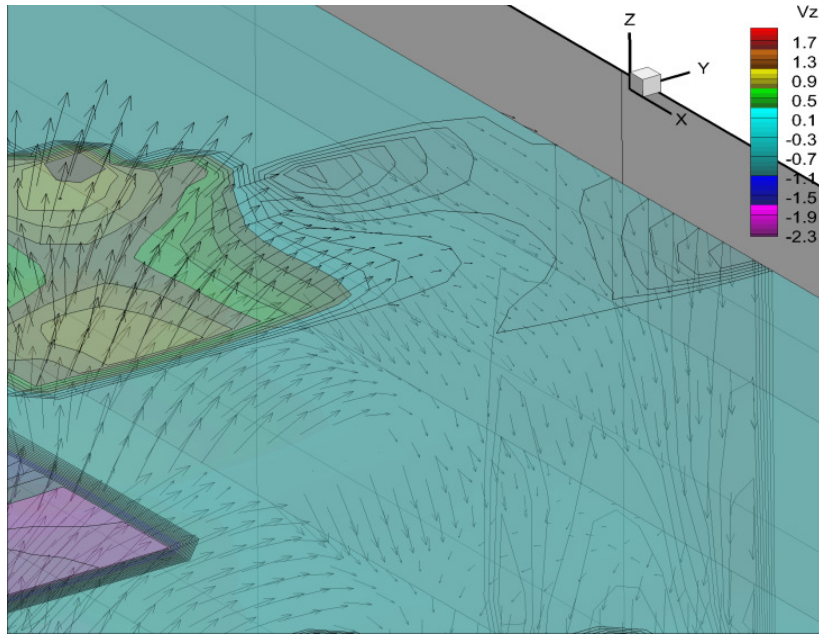


Figure 2- 11: 3C3D velocity vector field in the pore region close to sphere surface employing a 3D cross correlation through two multiple passes that a first pass using a 75% overlaps between interrogation windows with size of $128 \times 128 \times 32 \text{ voxels}$ and the second pass used $64 \times 64 \times 24 \text{ voxels}$ interrogation window with 60% overlaps [39]

Cross flow is observed in the micro porous region and the magnitude of velocity is found to be higher in the pore region. The third component of velocity is found to be higher in magnitude in the pore region compared to the densely packed regions. Such intricate flow structures which are observed experimentally within the micro porous media are believed to be reported for the first time through using the proposed 3C3D velocity measurement system.

2.4 Conclusion

This proposed 3C3D measurement system consists of a high speed CCD camera captures planar (x,y) images at discrete depth in the micro channel using a piezoelectric system that scans through depth (z -direction) with a thin focal plane

of an infinity corrected objective. The captured images in a single volume build the volumetric position of the intensity of the seeded fluorescent particles. Next, a 3D cross correlation algorithm is applied to the corresponding volumes built with the definite time interval in between that results in obtaining the near instantaneous three-dimensional velocity vector field.

In this chapter, an investigation in measuring the three-component three-dimensional of the velocity in micro-channel including mixing, segmented and porous media flow fields using the proposed 3C3D technique has been performed. The work highlights the potential use of this approach as a suitable technique for measuring the 3D flow field inside of the micro-channel using a relatively simple optical set-up. The advantage of this approach over conventional PIV is that it is tomographic in nature and can be used to resolve the three-components of the flow velocity over a volume. Also this technique can potentially resolved a large number of velocity vectors in comparison to the previous developed techniques, defocusing and off-focus methods.

In studying the flow motion in mixing channel, there was an optical distortion in the motion of the flow from one layer to another; this was due to the geometry of the channel. The possible solution for this case was matching refractive index of the fluid flow with the micro-channel refraction index.

In studying the segmented flow, the micro-channel should be hydrophobic to reduce the friction to the wall. There is also an effect of Brownian motion that needs to be studied particularly for sub-micron particle size at low speed flows.

A number of issues related to the impact of system specification of measurement uncertainty need to be resolved. The proposed 3C3D technique operates based on 3D cross correlation of the intensity volumes built by the scanned images. The first question in this technique is how well the cross correlation works on the intensity volumes. The intensity volumes built by scanning system are captured as a stretched bar of illumination due to diffraction rings and the scanning concept. There are also other parameters that are involved in measurement uncertainty that are required to be investigated. That includes tracer particle diameter, density, and the effect of background noise in 3D cross correlation of the intensity volumes. In addition, the parameters that involved in the maximum velocity range and spatial resolution of flow field is required to be described by the specification of the optics and imaging in the proposed 3C3D measurement system. This is related to the piezo-electric frequency and camera frame rate.

In chapter 3 a further exploration in investigating the related parameters involved in uncertainty analysis of the proposed 3C3D velocity measurement system is discussed. In chapter 4, a computational analysis is performed that discusses about the measurement uncertainty related to the above mentioned parameters of the study.

CHAPTER 3: Principles of uncertainty sources of the proposed three-component three-dimensional (3C3D) measurement system

3.1 Introduction

This chapter describes the principal of the uncertainty analysis as well as the sources of uncertainty in the proposed 3C3D imaging and velocity measurement technique. The discussion includes the physics of the flow in micro-channel as well as tracer particles in the micro-flow. This chapter is dedicated to raise the appreciation of a more in-depth understanding of the micro-velocity measurement and the complexity of modeling and simulation of this type of flow field.

The uncertainty contains the range at which a measurement is uncertain with a percentage of reliability. $x_{measured}$ is the measured value of the quantity x in the experiment, with associated uncertainty, u_x . The range of value of x with the odds of 20:19 (95% reliability) can be estimated by [40]:

$$x = x_{measured} \pm u_x \quad (3- 1)$$

In the proposed 3C3D velocity measurement system, x is the flow field velocity that is determined within the range of uncertainty of the measured value.

The observed uncertainties in the proposed 3C3D measurement system are classified in three categories as follows [40]:

- ***Systematic (Biased) uncertainty:*** This type of uncertainty is constant and is mostly related to the instrumental conditions. It is described by (mean-biased uncertainty) such as mis-calibration of the system magnification affecting the cross correlation algorithm in resolving the sub-pixel displacement.
- ***Residual (Random) uncertainty:*** This uncertainty changes by the experimental conditions repeatedly and varies randomly. It is uncontrollable as oppose to biased uncertainty and includes uncertainties due to various density or captured particle intensity diameter.
- ***Outliers:*** Those parts of results (calculated velocity vectors of flow field) which are numerically distant from the rest are called outliers. For a PIV correlation technique this could be where a small correlation peak exists due to insufficient data point such as a region of low particle density (eg. near the channel walls)

There are two approaches to determine the systematic and residual uncertainties in the system: experimental approval using a known flow field and computational techniques by deriving a formulation or running numerous simulations. In the experimental approach, a reliable known velocity (or displacement) of the real flow field such as recorded images from the uniform

flow field is used to determine the uncertainty of the system by comparing the analyzed result with the known input data. In this approach, the accuracy of the measurement system is determined for the definite experimental set-up parameters such as the definite laser illumination power, camera white noise, seeded particle diameters and density which this limits the determined accuracy to the specified conditions of the experiment and this would be the disadvantage of this approach.

Computational procedures have the advantage of being able to investigate the effect of every single parameter on the output result (velocity vector) through individual control of each parameter. There are two computational techniques to compute the uncertainty value; the *analytical method* [40] and *sequential perturbation* [40]. Both techniques are based on a *Root-Sum-Squared (RSS)* [40] estimate that is discussed in this chapter.

For the analytical method, a formula for the uncertainty is derived and the uncertainty analysis over every parameter is performed individually. The data reduction calculation in the analytical approach is dependent on the single driven formula and the computation might result in a complex calculation due to the forward computation. Conversely, the sequential perturbation technique is computationally simpler that might result in a less exact estimation of uncertainty. However, it will end in developing a model for data reduction. This technique starts with generating a flow field using synthetic images of the randomly seeded

particle in the flow and investigating the effect of the input variable and its perturbation on a calculated velocity. The disadvantage of this technique is being computationally expensive due to high number of simulations, $O(1000)$, for each parameter.

This chapter is devoted to discussing some of the sources of the uncertainty in the proposed 3C3D measurement system and estimating some of these uncertainties analytically. The uncertainty calculation is also extended in Chapter 4 using perturbation numerical analysis.

3.2 Review of the uncertainty analysis of measurement systems in the literature

Determining the uncertainty of any measurement system is the principle stage in validating and improving the approach. For three component velocity vector measurement including stereo PIV [8] and tomographic PIV [41], the uncertainty analysis was performed for various stage of the velocity measurement technique. The accuracy of the particle reconstruction in tomographic PIV was performed using several reconstruction algorithms and using synthetic image simulation technique [41].

For velocity measurement using micro-PIV [42], a synthetic image generation of the flow field seeded with 3D Gaussian intensity particles for measuring the velocity vector field was carried out using the laser sheet

illumination in the depth of channel in 3D2C velocity measurement [42]. In this study, Couette, Poiseuille, separated and mixing flow field were also simulated followed by estimating the measurement uncertainty of in-plane displacement velocity.

A 3C3D scanning technique that uses a scanning technique and the continuity equation to determine the out-of-plane component of the velocity was reported the uncertainty of the system. The uncertainty of this technique was estimated to be less than 3% using computational analytical method [43]. In addition, synthetic image generation and numerical perturbation analysis was performed earlier to estimate the uncertainty of the approach [44]. These studies suggest the importance of computational approach by developing synthetic images of the flow field towards uncertainty determination in the measurement system. The rest of this chapter is focused on the discussion of the sources of uncertainty in the proposed 3C3D measurement.

The data reduction computation can be expressed as measuring the value R obtained from measured quantity, x_i [45]:

$$R = f(x_1, x_2, \dots, x_n) \quad (3-2)$$

where R is the function of the related parameters, x_1, x_2, \dots, x_n . According to *Root-Sum-Squared* uncertainty, the uncertainty of R can be calculated with respect to the uncertainty of every quantity, x_i as follows:

$$u_R = \sqrt{\left[\left(\frac{\partial R}{\partial x_1} u_1 \right)^2 + \left(\frac{\partial R}{\partial x_2} u_2 \right)^2 + \dots + \left(\frac{\partial R}{\partial x_n} u_n \right)^2 \right]} \quad (3-3)$$

where δx_i is perturbation of the parameter x_i with related uncertainty of u_i .

Perturbation analysis based on fundamental theorem of calculus is developed to equation (3- 4):

$$\frac{\partial R}{\partial x_i} = \lim_{\Delta x_i \rightarrow 0} \left[\frac{R(x_i + \Delta x_i) - R(x_i)}{\Delta x_i} \right] \approx \frac{R(x_i + \delta x_i) - R(x_i)}{\delta x_i} \quad (3-4)$$

If uncertainty $u_i \approx \delta x_i$, then

$$\left[\frac{\partial R}{\partial x_i} \delta x_i \right]^2 \approx \left[\frac{R(x_i + \delta x_i) - R(x_i)}{\delta x_i} \delta x_i \right]^2 = [R(x_i + \delta x_i) - R(x_i)]^2 \quad (3-5)$$

Therefore, the uncertainty in R due to perturbation in x_i can be estimated by:

$$u_{R_i} \approx [R(x_i + \delta x_i) - R(x_i)]^2 \quad (3-6)$$

and the total uncertainty of the system is described with the following equation:

$$u_R \approx [u_{R_1}^2 + u_{R_2}^2 + \dots + u_{R_n}^2]^{1/2} \quad (3-7)$$

For strongly nonlinear $R(x_1, x_2, \dots, x_n)$, the above formula does not imply an accurate estimate of the uncertainty. The total uncertainty in the system, u_{total} , is calculated as:

$$u_{total}^2 = \sum_i u_i^2 \quad (3-8)$$

This equation describes that the total uncertainty in the measurement system that is the summation of the calculated uncertainty for every dependent parameters in the measurement.

3.3 Sources of uncertainty

There are three main sources of uncertainty in velocity measurement using the proposed 3C3D system which include the experimental conditions, the set-up of the experiment and the processing algorithm used to assess data. Some of these uncertainties are biased in the system that caused systematic uncertainties such as mis-calibration. Random uncertainties can vary in each experiment and examples include the seeded particle shape, size, and density and image background noise. The uncertainty estimation due to processing algorithm is described in Chapter 4 using perturbation analysis.

3.4 Experiment's conditions:

In particle based measurement techniques, there is a random uncertainty in the measurement due to the condition of fluid flow and seeded particles in the flow that changes from each experiment to another. In this section, the uncertainties due to using seeding particles in flow velocity measurement are discussed.

3.4.1 Flow in micro-channel

The experimental flow was water with mean molecular spacing $\delta_{mean} \approx 0.3 \times 10^{-9} m$ and this flow is seeded with fluorescent particles whose parameters given in Table 2-1. For the standard cross section of the channels used in the experiment the calculated hydraulic diameter was $L=27\mu m$ in the Tear-Drop channel and $L=107\mu m$ in serpentine channels. The order of molecular spacing over the hydraulic diameter ($\frac{\delta}{L} \approx O(100000) \leq 3 \times 10^{-5}$) at STP situation where the continuity equation holds [4]:

$$\nabla \cdot \vec{V} = 0 \quad (3-9)$$

The flow in the micro-channel is usually assumed to be Stokes flow due to the low velocity and small geometry of the channel. Reynolds number (Re) is calculated by:

$$Re_d = \rho V_0 d_p / \mu \quad (3-10)$$

where ρ , μ , and V_0 are density, viscosity, and average velocity of the flow field.

d_p is the diameter of the seeded particles in the flow.

The Stokes number (Stk) of the flow can be calculated by:

$$Stk = \tau V_0 / d_p \quad (3-11)$$

where τ is particle respond time. In the experiments, the velocity is usually in the

order of 10^{-6} $\mu\text{m/s}$ and particle diameter was around $1\mu\text{m}$. The response time for the particle is the time that particle responds to the flow changes and it is calculated by:

$$\tau_p = \frac{d_p^2 \rho_p}{18\mu} \quad (3-12)$$

where ρ_p is particle density.

The order of the relation time in the experiments is calculated to be in the order of $O(10^{-9})$ seconds. This response time is much smaller than the time scale of the measurement system ($\Delta t = 5\text{ms}$) in the current set-up of the system that camera operated 200fps, capturing 100 images in one scan of piezo with frequency of 1Hz. The calculated Re and Stk , numbers are in order of $O(10^{-6}) \ll 1$ and $O(10^{-9}) < 0.1$ respectively. Therefore, this shows that the experimental flow can be characterized as Stokes flow. Hence, the conservation of momentum is reduced to the form of Stokes equation:

$$\nabla p = \mu \nabla^2 \vec{V} \quad (3-13)$$

3.4.2 Suspended particles in micro-flow

There exist several forces on a suspended tracer particle in the flow that knowing these forces and the order of these can be useful in estimating the uncertainty in velocity measurement in PIV calculations. The body forces, \vec{b} , include gravity,

buoyancy, as well as the surface forces including electric, and magnetic forces, the friction drag force, and Van der Waals force are the significant forces in studying the kinetic of the particle's motion in the flow.

The micro-channels used for mixing and segmented experiments in Chapter 2 were made of borosilicate glass that is in contact on the aqueous medium of water. The fluid has a $pH > 3$ which dissociate H^+ ions off the surface [46]. This results in a negative surface charge which is prone to the formation of a zeta potential on the glass surface [46] which results in an electric double layer. This is characterized by a Debye length, κ^{-1} , described by:

$$\kappa^{-1} = \frac{3.304}{Z\sqrt{M}} \times 10^{-10} \quad (3-14)$$

where Z and M are electric capacity and morality of the electrolyte for a symmetric electric charge solution for water liquid.

The calculated Debye length for the water with neutral electrolyte ($pH \approx 7$) and $0.01M(1:1)$ dissolved NaCl is calculated to be $\kappa^{-1} = 3.04 \times 10^{-9} m$. The electric double layer causes the distribution of ions in the electrolyte and forming an electric potential, ψ , near the surface and electric field, E , obtained by Poisson equation:

$$\vec{E} = -\nabla \psi \quad (3-15)$$

The particles suspended in the water demonstrated negative surface charge [47].

Therefore, the electric force on a particle is obtained by:

$$\vec{F}_e = \vec{E}q \quad (3-16)$$

where q is the surface charge of the suspended particle.

In addition, there exists a repulsive force among the charged particles describing by Coulomb's equation:

$$\vec{F}_e = \frac{q_1 q_2}{4\pi\epsilon_0} \frac{\vec{r}}{r^2} \quad (3-17)$$

where ϵ_0 is permeability constant, and r is the distance between two particles.

The direction of this force is in direction of the unit distance vector \vec{r} .

There is also a mutual attraction among particles and between particles and wall due to Van der Waals forces, F_{vw} . There is an approximation of this force is performed by Derjaguin between bodies of two spheres with diameter of R_1 and R_2 with the distance r :

$$F_{vw}(r) = \frac{A_H}{6} \left(\frac{R_1 R_2}{R_1 + R_2} \right) \frac{1}{r^2} \quad (3-18)$$

where A_H is Hamaker constant of the system.

Also, Van der Waals force between the channel walls and a tracer particle with diameter of a positioned at the distance r from the wall can be described by:

$$F_{vw}(r) = \frac{A_H R}{6r^2} \quad (3-19)$$

The drag force, F_D , on the fluorescent particles flowing in the Stokes flow sufficiently away from the wall (centerline of the channel) is described by:

$$\vec{F}_D = 6\pi\mu d_p \vec{V} \quad (3-20)$$

However, the drag force is different for the particles that are moving near the wall. The lag factor of the particle near the wall is significant due to hydrodynamic force between the particle and the wall [48]. The drag force on the particle due to the wall is corrected by a correction factor, K_1 , and described by:

$$\vec{F}_D = 6\pi\mu d_p \left(K_1 \vec{V}_p - K_2 \vec{V} \right) \quad (3-21)$$

The particles have the specific weight of 1.050 described in Table 2-1. Therefore, these suspended particles in fluid flow water can be considered to be neutrally buoyant. The above mentioned forces on tracer particle flowing in the micro-flow enter the particle dynamic motion equation [49]

3.4.3 Particles in PIV measurement

There is a basic assumption in all particle based measurement techniques that particles follow the flow faithfully. Velocity measurement of a particle or groups of particles describes the bulk of flow field velocity seeded by those particles. This assumption introduces a common source of uncertainty to all particle based

measurement techniques that describes how closely the particle velocity measurement would be to the actual fluid flow velocity.

The relation between Eulerian fluid velocity and Lagrangian particle velocity can be described by [49]:

$$\underbrace{\vec{V}(\vec{X}_p, t^*)}_{\text{Eulerian}} = \underbrace{\frac{\Delta \vec{X}_p}{\Delta t} + [\vec{X}_p - \vec{X}_p(t^*)] \cdot \nabla \vec{V} \Big|_{@ \vec{X}_p} - [\vec{V}_p(t^*) - \vec{b}] \vec{t}_p - \frac{1}{24} \vec{\ddot{V}}_p(t^*) \Delta t^2 + O(\Delta t^4)}_{\text{Lagrangian}} \quad (3-22)$$

where \vec{V} is the bulk fluid flow velocity, \vec{X}_p is particle average displacement, Δt is the time scale of the experiment. This velocity is estimated in PIV based techniques by dividing the average displacement of a group of seed particle [$\Delta \vec{X}_p = \vec{X}_p(t + \Delta t) - \vec{X}_p(t)$] between two corresponding images over the definite time scale (Δt). The potential difference of actual flow velocity and measured particle velocity by the measurement system illustrated in Figure 3- 1:. The straight line is the average displacement of the particle and the dashed line is the trajectory of the particle. This average velocity of the particle estimates the instantaneous velocity of the bulk flow at time $t^* = t + \Delta t / 2$ and average position

$$\text{of the particle } \vec{X}_p = \frac{\vec{X}_p(t + \Delta t) + \vec{X}_p(t)}{2}.$$

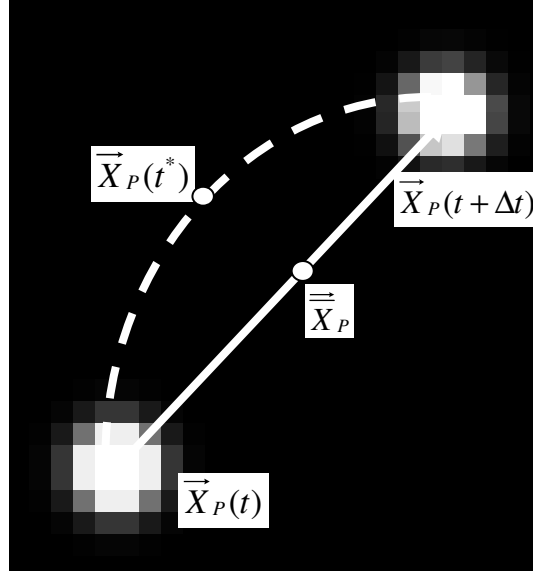


Figure 3- 1: Particle intensity displacement projected over the image

Similar to any PIV technique, the proposed 3C3D measurement calculates

the average velocity, $\frac{\Delta \vec{X}_P}{\Delta t}$, through the cross correlation two intensity volumes.

This calculated average velocity is the ratio of the average displacement, ΔX_p , between two corresponding correlated intensity volumes over the definite time intervals of the experiment, Δt . As equation (3- 22) shows in Lagrangian particle

velocity, there are other terms including the flow field gradient term over the particle displacement $[\vec{X}_P - \vec{X}_P(t^*)] \cdot \nabla \vec{u} \Big|_{@ X_P}$, the particle lag term

$-\vec{V}_P(t^*) - \vec{b} \tau_P$, and the particle jerk term, $\frac{1}{24} \vec{V}_P(t^*) \Delta t^2$; these parameters are

not measured during normal double-pulsed PIV cross correlation which may cause uncertainty in the measurement.

As it was discussed earlier, the flow is Stokes flow and the time scale of the measurement system is in order of $O(10^{-9})$ nano-seconds and as the velocity is in order of $O(10^{-6})$, the effect of particle lag term can be neglected. And typically, the effect of particle acceleration and jerk can be estimated by local acceleration and change of it for fluid flow, for the experimental flow measurement:

$$\vec{V}_p \approx \left. \frac{D\vec{V}}{Dt} \right|_{x=x_p} = \left[\frac{\partial \vec{V}}{\partial t} + \vec{V} \cdot \nabla \vec{V} \right]_{x=x_p} \quad (3-23)$$

and, in the experiment's micro-fluid flow, the flow was laminar, therefore, this effect can be ignored as well.

In addition, Brownian motion has a significant impact in studying the fluid flow using sub-micron seeded particles [6]. Brownian motion is the random thermal motion of a particle suspended in the flow field. The collisions between liquid molecules and particle molecules results in introducing high frequencies in the particle velocity motion. This statistical mean displacement, $\langle \Delta s \rangle^2$, at time scale of the experiment, Δt , due to molecular diffusion is expressed by:

$$\langle \Delta s \rangle^2 = 2D \cdot \Delta t \quad (3-24)$$

where D is diffusion coefficient obtained from the Stokes-Einstein equation:

$$D = \frac{K_B T}{6\pi\mu d_p} \quad (3- 25)$$

where K_B is the Boltzman constant and T is the mean temperature of the fluid flow . The diffusion coefficient, D , is calculated to be in the order of $10^{-14} \text{ m}^2/\text{s}$ for the polystyrene particle diameter of $1\mu\text{m}$ and room temperature of 20°C . The uncertainty due to Brownian motion in measuring the velocity $\vec{V}(u, v, w)$ is described with the following equations as a ratio of the mean displacement due to Brownian motion over the particle average displacement in the measurement for every component of the velocity in Cartesian coordinate system [6]:

$$\varepsilon_x = \frac{1}{u} \sqrt{\frac{2D}{\Delta t}}, \quad \varepsilon_y = \frac{1}{v} \sqrt{\frac{2D}{\Delta t}}, \quad \varepsilon_z = \frac{1}{w} \sqrt{\frac{2D}{\Delta t}} \quad (3- 26)$$

Brownian motion establishes a lower limit for measuring the velocity in the time scale of Δt . As the flow field velocity becomes smaller, the uncertainty due to Brownian motion increases. For instance, the smallest flow velocity component in the experimental flow field of water for a single particle uncertainty of 4% and particle diameter of $1\mu\text{m}$ for a camera frame rate of 210 fps (time scale of $\Delta t = 5\text{ms}$) is in the order of $10\mu\text{m} / \text{s}$. The Brownian diffusion uncertainty is an unbiased uncertainty and it can be significantly decreased by averaging over a high number of the particles [6]. Assuming that each particle has an independent contribution to the average velocity measurement, then the uncertainty due to Brownian motion for N number particles in one pair interrogation volume would be described by [6]:

$$\varepsilon_{total} = \varepsilon / \sqrt{N} \quad (3-27)$$

The size of the tracing particles in the flow has to be small enough that they follow the flow without disturbing the flow field while being large enough to be imaged and correlated in the processing algorithm

3.5 Experimental set-up:

There exists some uncertainty that is related to the imaging system and cross correlation algorithm. For instance, the uncertainty related to resolution of the particle image intensity, digitization of the image due to camera pixel size and non-uniform laser power. In this section, some of these uncertainties are discussed.

3.5.1 Experimental displacement uncertainty

There is a relation between a physical velocity of the particle to the image velocity of the particle that is expressed by the magnification factor, M_0 . For the in-plane displacement of a particle, Δx_p :

$$\frac{\Delta x_p}{\Delta t} = \frac{\Delta X_p}{M_0 \Delta t} \quad (3-28)$$

where ΔX_p is image particle displacement at Δt , time scale of the system.

Applying a perturbation in the physical particle velocity gives:

$$\delta\left(\frac{\Delta x_p}{\Delta t}\right) = \delta\left(\frac{\Delta X_p}{M_0 \Delta t}\right) \quad (3-29)$$

By taking the differential from right hand side and reorganize the formula:

$$\delta\left(\frac{\Delta x_p}{\Delta t}\right) = \frac{\Delta X_p}{M_0 \Delta t} \left(\frac{\delta \Delta X_p}{\Delta X} + \frac{\delta M_0}{M_0} + \frac{\delta \Delta t}{\Delta t} \right) \quad (3-30)$$

In order to explore the uncertainty further, the equation above is expressed as a standard uncertainty analysis (RMS):

$$\frac{\delta\left(\frac{\Delta x_p}{\Delta t}\right)^2}{\left(\frac{\Delta x_p}{\Delta t}\right)^2} = \underbrace{\left(\frac{\delta \Delta X_p}{\Delta X_p}\right)^2}_{\text{Random}} + \underbrace{\left(\frac{\delta M_0}{M_0}\right)^2 + \left(\frac{\delta \Delta t}{\Delta t}\right)^2}_{\text{Deterministic}} \quad (3-31)$$

The timing deterministic uncertainty is related to the imaging system. In the current set-up of the system (model piA640-210gm/gc, Basler camera Pioneer) the minimum input signal for camera to operate is 5 volts. Therefore, as soon as the trigger signal drops less than 5 volts, camera stops capturing images. The camera trigger signal with amplitude of 5 volts has a timing delay of rising signal of $1.5\mu s$ and the falling time delay of $1-20\mu s$ [50]. The falling signal has no impact on the timing uncertainty of the system; however, the rising time signal introduces a timing uncertainty to the measurement. The timing uncertainty is relatively small compared to the time scale of the system ($\Delta t \approx 5$ ms for camera maximum frame rate of 200 fps at full resolution), $\delta \Delta t \ll 1$, therefore, the timing uncertainty can be assumed to be negligible.

The magnification uncertainty can be assumed to be $\delta M_0 \approx 0$, because the magnification of optics of the system is a known value (for current set-up is $M = 5.4$ obtained from the calibration using a micro-calibration target) with a uniform volumetric illumination provided by the laser.

The only term of image uncertainty, $\delta \Delta X_p$, becomes significant in the uncertainty calculation of the system. This term depends on several parameters of the correlated intensity volumes including images' background noise that consist of volume correlation intensities, pixel resolution and cross correlation algorithm. The effect of collected image resolution is discussed in the next section. However, the effect of image background noise and cross correlation algorithm is discussed in chapter 4.

3.5.2 Camera pixel size

This type of uncertainty originates from discretizing the continuous 3D Gaussian intensity distribution emitted from the fluorescent particles over the image. There exists a minimum camera pixel size to provide the sufficient resolution of the system in PIV known as a Parzen bandwidth [49].

3.5.3 Fluorescent particle Gaussian intensity

In the proposed 3C3D micro-PIV measurement system, the illumination is provided uniformly volumetrically to the flow field. The intensity of the light captured from the fluorescent particles varies by the distance of the particle from

the focal plane [51]. Diffraction rings generated by out-of-focus fluorescent particles due to their distance from the focal plane contributes to the uncertainty of the flow measurement. Figure 3- 2 demonstrates the fluorescent particle (light source) positioned at the object plane at the distance S_0 from objective lens with aperture diameter of D_a . The out-of-plane displacement, in the direction of z -axis, produces the defocusing rings due to diffraction and spherical lens aberration on the image plane [13].

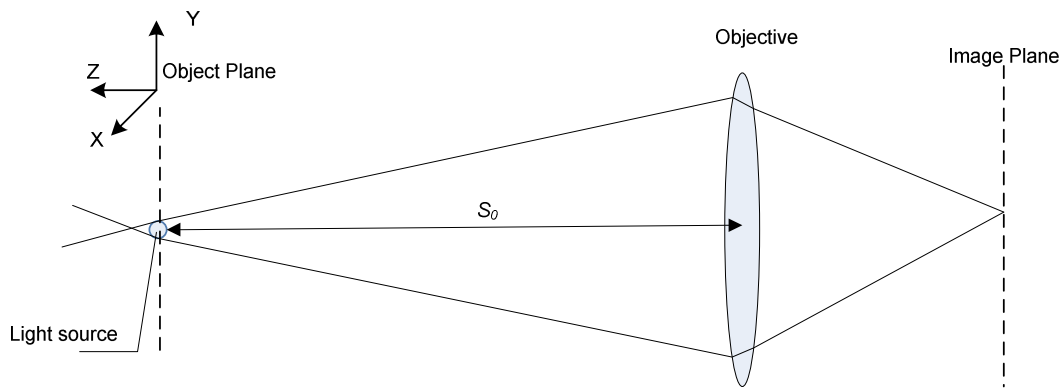


Figure 3- 2: Schematic of the optics of the measurement system

The intensity distribution over the depth, in the z direction, of the out-of-focus sub-micron fluorescent particles with diameter d_p is given in polar-coordinate system [52]:

$$I(r, z) = I_0 \exp\left(\frac{-4\beta^2 r^2}{d_e^2}\right) \quad (3-32)$$

where $I_0 = \frac{J_p D_a^2 \beta^2}{4\pi d_e^2 (s_0 + z)^2}$, r is in-plane radial position of the particle, and d_e is

effective diameter of the particle and calculated with [52]:

$$d_e^2(z) = M_0^2 d_p^2 + 5.95(M_0 + 1)^2 \lambda^2 f^{\#2} + \frac{M_0^2 z^2 D_a^2}{(s_0 + z)^2} \quad (3-33)$$

The effective diameter of the diffraction ring is a function of z (depth), λ , the wavelength of the laser, J_p , the light flux emitted from the particle, with the constant factor of $\beta^2 = 3.67$ [52]. The first term of the equation (3-33) describes the diameter of the particle in the image due to magnification. The contribution of the diffraction rings is the second term of the equation and the contribution of the defocusing is given by the third term of this equation [51]. This above equation describes the continuous Gaussian intensity emitted from the particle and this intensity is digitized by the camera pixels.

3.5.4 Pixilation of the particle's Gaussian intensity

Capturing images through the camera sensor is a process of converting a (continuous) Gaussian intensity signal emitted from fluorescent particles into a discrete numeric value spatially on a sensor with definite pixel size and pixel number. This spatial digitization of a signal occurs at a specific sampling frequency and size. Sampling frequency is the number of the recorded samples

per unit distance during digital-to-analog conversion. On the sensor this indicates spatially as number of the pixels that discretize a continuous Gaussian intensity of the fluorescent particles

Aliasing occurs due to too large sample size that results in small sampling frequency. In this condition, the relation between the 3D adjacent voxels is hardly related to describe the analog signal (Gaussian intensity emitted from fluorescent particle) is hardly recognizable. The camera pixel size is discretized the light over the pixels, and as the pixel size becomes larger, the number of illuminated pixels are reduced.

The Nyquist's criterion describes the minimum sampling frequency, $2W$:

$$Wd_r \leq \frac{1}{2} \quad (3- 34)$$

where d_r is the pixel size, for current CCD camera is $7.4\mu\text{m}$, and W is the optical band width that is followed by [49]:

$$W = \frac{D_a}{\lambda f (M_0 + 1)} \quad (3- 35)$$

then with the specification of system, $\lambda = 0.532 \text{ mm}$, $NA = 0.25$, $D_a = 9 \text{ mm}$, $M_0 = 5.4$, and focal length of $f = 10.6 \text{ mm}$, the $W = 249 \text{ mm}^{-1}$ and by checking the equation (3- 37), the current set-up of the system is below the Nyquist criteria. However, in PIV, the direct electronic imaging is not required to resolve the full optical bandwidth [49]. Therefore, Parzen Bandwidth was introduced as a criteria

for diffraction limited particle images which is one third of the optical bandwidth [49]:

$$W_p \cong 0.31 \frac{D_a}{\lambda f (M_0 + 1)} \quad (3-36)$$

that $W_p = 77.2 \text{ mm}^{-1}$ so that the minimum pixel size $6.5 \text{ }\mu\text{m}$, the current set-up almost meets this criteria and therefore, can be used for the PIV measurements. However, improving the optics of the system as well as the camera would benefit in flow measurement.

Obtaining more samples with the same number of photons for a signal improves the signal to noise ratio (SNR). However, if more samples result in the same quality in the results, then oversampling has occurred. Over sampling is computationally expensive and contains extra information.

In addition, there is a condition for resolving the particle image diameter over camera sensor that is the 2-3 pixels [53]. For the current set-up of the system, the effective particle diameter for the physical particle size of $1 \text{ }\mu\text{m}$ followed by equation (3-33) at $z=0$, where the particle is at sharp focus in the image plane, is $17.5 \text{ }\mu\text{m}$. This diameter can be resolved over 2 pixels for camera pixel size of $7.4 \text{ }\mu\text{m}$. This just satisfies the criteria for PIV cross correlation minimum resolution.

3.5.5 Sub-pixel displacement discretization

As the particle moves along the flow, the camera captures images of the flow field and the Gaussian intensity of the fluorescent particles is digitized by the camera

pixels. Figure 3- 3 shows that the distribution of the intensity of the light captured by camera sensor for a single particle at two distinct times by sub-pixel displacement is not quite preserved.

This shows that some part of the light emitted from the particle will be dissipated. Therefore, the illumination energy is not completely conserved and the shape of the particle's intensity changes in sub-pixel displacement. This can affect the search of the center of the particle intensity in PIV techniques.

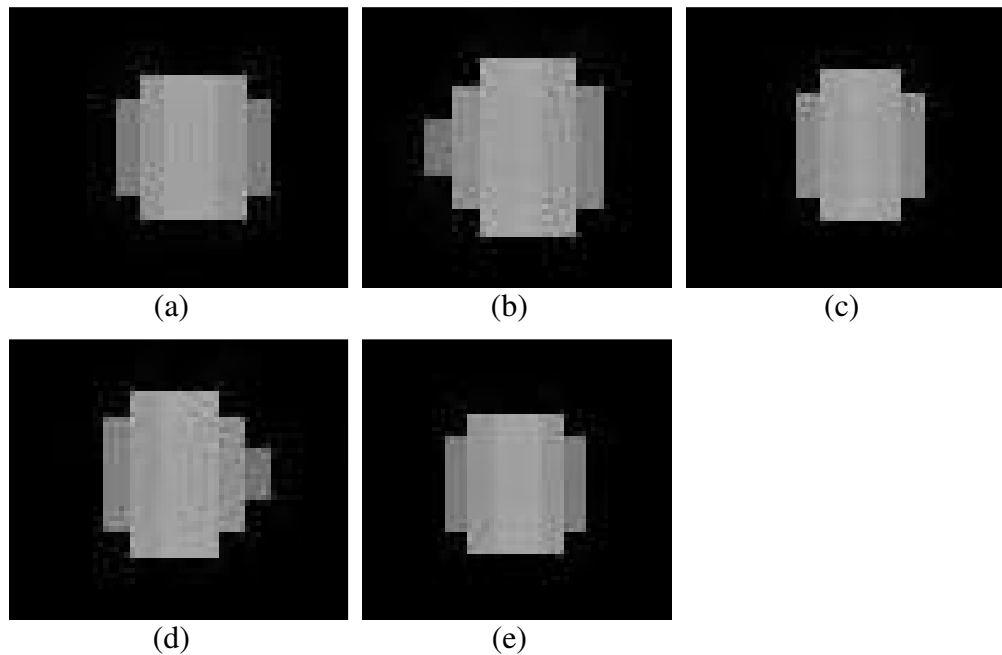


Figure 3- 3: Sub-pixel planar displacement of particle at definite depth (a) relative origin(0,0,0) (b) (0.25,0,0) pixel (c) (0.5, 0,0) pixel (d) (0.75,0,0) pixel (e) (1,0,0) pixel

3.5.6 Piezo-electric system

In addition to digitization of the signal in planar direction using imaging system, the 3D Gaussian intensity is discretized in the out-of-plane direction by the number of the images captured in depth. As the number of the images in the depth

direction increases, the spatial distance between two successive images decreases which results in the increase of the resolution of the measurement system in out-of-plane direction.

Figure 3- 4 shows the change in Gaussian intensity along depth obtained from a set of experimental images. It is observable that a 3D Gaussian intensity shape of the particle is preserved by the present sampling rate in depth, $f_{piezo} = 1Hz$. This results in the accuracy of $1\mu m$ in out-of-plane direction.

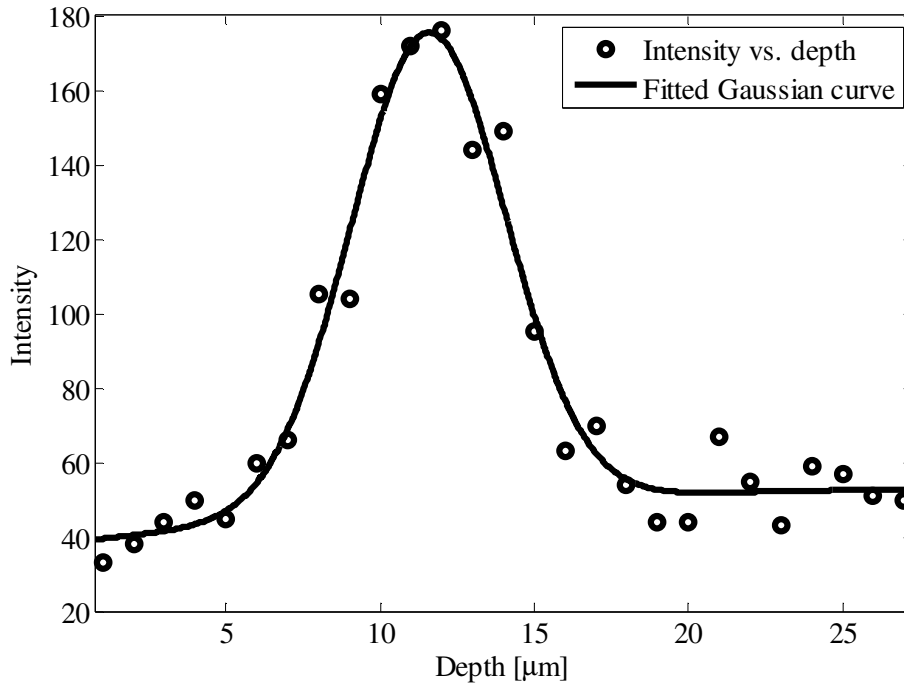


Figure 3- 4: The Gaussian intensity distribution of experimental data obtained from a $1\mu m$ particle positioned at depth of $12\mu m$ and was discretized by 27 slices that each positioned $1\mu m$ apart with the image depth of 8bits/pixels

3.5.7 Dynamic range in in-plane velocity

The maximum measurable in-plane velocity depends on the frequency of capturing the images which is restricted to the frequency of scanning, f_{piezo} , and frequency of camera frame rate, f_{camera} . Equation (3- 37) relates the measurable in-plane velocity, \vec{V} with the planar displacement of the particle across the interrogation window between two corresponding intensity volumes, $\Delta\vec{X}$, magnification of the system, M_0 and frequency of capturing the images, f .

$$\vec{V} = \Delta\vec{X}.f/M_0 \quad (3- 37)$$

The physical in-plane displacement of the particle is obtained through the division of the displacement in the image $\Delta\vec{X}$ by system magnification, M_0 . As equation (3- 37) describes the velocity is proportional to the system frequency and displacement. In order to maximize the measurable velocity, the frequency and the displacement has to be maximized. The maximum frequency, f_{max} , of the system is the minimum of the each maximum frequency of camera, f_{camera} , and piezo, f_{piezo} .

The scanning frequency rate, f_{piezo} , is determined by the piezo scanning system and the specification of the current piezo electric system (PZ100, Piezosystem Jena) is listed in the Table 3- 1:

Table 3- 1: Objective mass and resonance frequency of Piezo system Jena

Mass of objective	Resonance frequency of scanning
10X (68.1 g)	460 Hz
20X (70.4 g)	460 HZ
50 X (180 g)	300 HZ

Table 3- 1 indicates that as the mass of the objective attached to the piezo stage increases, the resonance frequency of the piezo decreases, which limits the working frequency of the piezo-stage. For the current set-up of the system with 10X objective, the maximum frequency of scanning is $f_{piezo_{max}} = 460\text{Hz}$.

In full resolution of the, the maximum camera frame rate is $f_{camera_{max}} = 200\text{fps}$. According to the above calculations and using the current system set-up with full resolution of the image, the time scale of the maximum velocity measurement is restricted by the minimum of the maximum frequencies in the system which is equal to $f_{max} = 200\text{Hz}$. However, there is also a possibility to increase the camera frame rate by decreasing the region of the interest in the camera image that results in reducing camera sensor readout time and eventually increasing the camera frequency higher than 200fps . The equation (3- 38) describes the relation between maximum camera frame rate and height of area of interest, h_{AOI} :

$$f_{camera} = \frac{1}{[h_{AOI} \times C_1] + C_2} \quad (3-38)$$

where C_1 and C_2 are the camera sensor's constants depending on the camera model, (piA640-210gm/gc, Basler Pioneer camera) are $8.03 \mu\text{s}$ and $908.82 \mu\text{s}$ respectively [50].

In addition, equation (3-37) describes that \bar{V} is proportional to ΔX , the particles displacement. The maximum displacement of the particles in an interrogation window is the size of interrogation window in the direction of displacement $X_{InterrogationWindowSize}$. Figure 3-5 shows the change in measuring the maximum in-plane-velocity with respect to size of interrogation window for the current-set up of the system by assuming of the full resolution of maximum frequency of 200Hz.

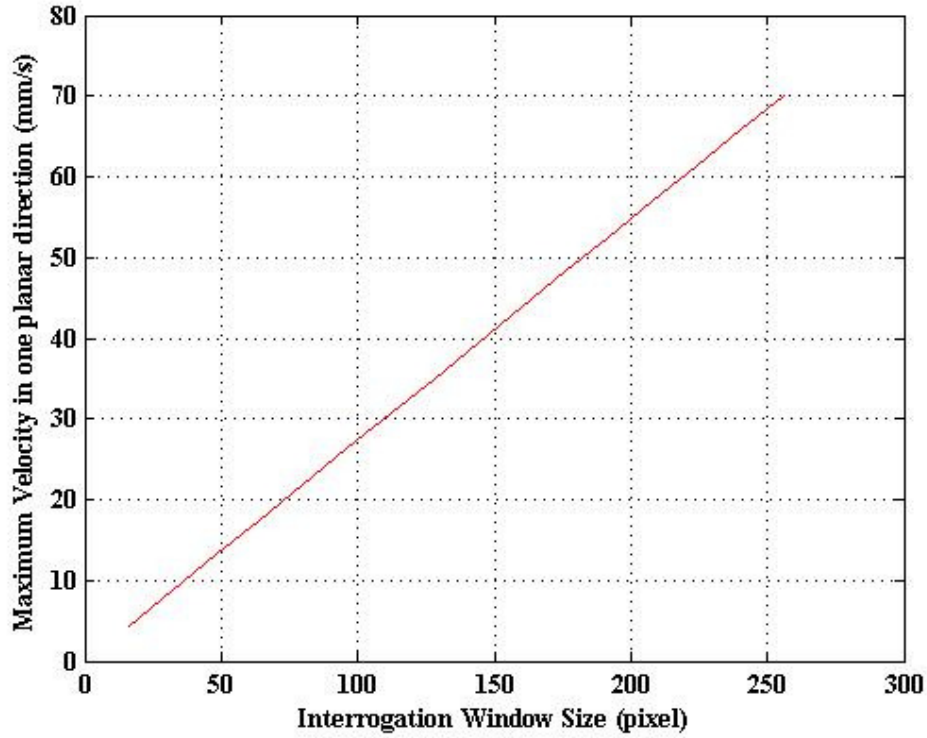


Figure 3- 5: Maximum in-plane velocity by the proposed 3C3D measurement system for $f=200\text{fps}$

The minimum displacement of the seeded particle in the flow field resolvable by system is the resolution of the system, one pixel or the size of the pixel in physical flow. Any displacement less than one pixel is calculated as maximum of one pixel in measurement system. Therefore, for the current set-up of the system, the minimum physical displacement, $\Delta x_{p,\min}$, of the particle is pixel size divided by magnification of the system ($M_0 = 5.4$):

$$\Delta x_{p,\min} = 1\text{pixel} \times 7.4 \mu\text{m} / M_0 = 1.37 \mu\text{m} \quad (3- 39)$$

Dynamic spatial range (DSR) of the system which is the division of field of view by the minimum resolvable scale. DSR determines the capability of the system to resolve the small scale variation of the flow in the larger scale flow motion. DSR is calculated by the following equation;

$$DSR = \frac{l_x}{\Delta x_{p \min}} = \frac{L_x/M_0}{\Delta x_{p \min}} \quad (3-40)$$

where L_x and L_y is the size of camera sensor that is calculated in x and y direction respectively in Cartesian coordinate system in equation (3-41):

$$L_x = 488 \text{ pixels} \times 7.4 \text{ } \mu\text{m} = 3611.2 \text{ } \mu\text{m} \quad (3-41)$$

$$L_y = 648 \text{ pixels} \times 7.4 \text{ } \mu\text{m} = 4795.2 \text{ } \mu\text{m}$$

Using the above values and substituting in equation (3-40), DSR is calculated to be 90.4 along x axis and 120 along y -axis for the current set-up of the system.

3.5.8 Dynamic range in out-of-plane

The maximum resolution in out-of-plane displacement measurement is assessed by the size of the selected interrogation window in depth. The minimum measureable displacement in depth is limited by the distance between two successive image slices in depth. The number of images captured in one entire scan in depth is restricted to scanning rate and camera frame rate. As the number of slices in an entire scan in depth increases, the physical space between each slice decreases, therefore, the resolution of the system in measuring the out-of-plane displacement improves. The current set-up of the system, the piezo scans

through depth of maximum $100\mu\text{m}$ with maximum amplitude of operation, 10 volt and by capturing 100 images in depth, the accuracy in out-of-plane direction is calculated to be $1\mu\text{m}$. In addition, to explore the out-of-plane displacement further, a perturbation analysis in measuring the out-of-plane displacement is performed in chapter 4.

3.6 Conclusions

In this chapter, the principals of the measurement system's uncertainty analysis were explained, followed by a discussion of an analytical approach towards the source of the uncertainties in the 3C3D measurement system. The sources of uncertainties in the system contain the experimental conditions, experimental set-up and processing algorithm. The experimental conditions introduce random sources of uncertainty to the measurement including the forces imposed on a suspended particle in the flow field. The experimental set-up uncertainty discussed the effects of planar digitization of the 3D continuous Gaussian intensity emitted from the particles over the camera pixel size, and the relation of the discretization of the particle's intensity in depth by the number of the slices captured in depth.

Dynamic velocity range and dynamic spatial resolution of the system is also determined by calculating the maximum and minimum displacement and time scale of the system. The maximum image displacement is equal to the size of the interrogation window in the processing algorithm and the minimum in-plane

displacement is the size of the resolution of the system, one pixel. However, the minimum out-of-plane displacement is related to the space between two successive images building the volume of the intensity, as the number of the images that build the volume increases the resolution of out-of-plane displacement increases. The maximum frequency of the operation of the system is restricted to the minimum of the maximum camera frame rate and maximum piezo scanning frequency.

Velocity vector field is obtained through a complex processing algorithm that includes image processing and data analysis. There are several parameters that are involved in processing algorithm including particle diameter, particle density, laser non-uniform illumination, white background noise in the images. In Chapter 4, the investigation of the processing algorithm is carried out by generating synthetic images that defined the volumetric intensity of the seeded flow field and developing a numerical processing algorithm including a 3D cross correlation over two corresponding volumetric intensities followed by a 3D peak detection to determine the average displacement between every volume of the intensity. The effect of each parameter on the velocity vector field is studied using perturbation computational analysis.

CHAPTER 4: Perturbation analysis of the proposed Three-component three-dimensional (3C3D) measurement system

4.1 Introduction

In the Chapter 3, sources of uncertainties in 3C3D velocity measurement system based on three the categories of experimental set-up, experimental conditions and data processing were discussed. The analytical uncertainty analysis in Chapter 3 provides useful information on investigating the uncertainty due to discretization of the Gaussian particle intensity with the 3C3D scanning imaging technique and the forces involved on a suspended seeded particle in the flow field. Some of the parameters involved in the uncertainty were developed through a formulation and contains biased uncertainty results in the systematic uncertainty of the measurement system, U_{bias} .

In this chapter a computational perturbation analysis using a Monte-Carlo simulation provides further information in investigating the impact of the parameters with complex formulation as well as those with highly random effects. This includes the investigation of uncertainty (U_{rms}) influenced by particle intensity shape, diameter, particle density in the flow field and out-of-plane displacement. The total uncertainty, U_{total} , in the measurement system can be

described by summation of the random and biased uncertainties on velocity measurement determined using the proposed 3C3D system by :

$$\mathbf{u}_{total} = \mathbf{u}_{bias} + \mathbf{u}_{rms} \quad (4-1)$$

As described earlier, the concept of the proposed 3C3D measurement technique is based on scanning through the depth of micro-channel with a thin focal plane. Then, the collected images are stacked together and the volume of intensity of particles is built. By stacking these images, the constructed volumetric intensity of a particle appears as a stretched rod of illumination with diffraction rings around it. Next, a 3D cross correlation is performed between these constructed rods instead of constrained semi-spherical particles built at a discrete time interval. One of the first main challenges of this technique is understanding the accuracy of correlating the intensity volumes appearing as a rod of illumination in three dimensional flow measurements.

In this chapter, the effect of spherical or cylindrical particles with finite length and diameter seeded in a uniform in-plane and out-of-plane flow field is investigated using synthetic images. A 3D cross correlation algorithm extended from the 2D normalized cross correlation followed by a three-point three dimensional Gaussian peak detection algorithm based on three-point two-dimensional Gaussian regression is used to obtain the velocity vector field.

In addition, a series of Monte-Carlo simulations is performed to investigate the effect of several parameters in velocity measurement using the proposed 3C3D

measurement system. This includes optimum particle image intensity voxel diameter, particle density, and effect of background noise.

4.2 Methodology

A Monte Carlo simulation has been widely used in uncertainty analysis of PIV by digitally generating synthetic images of flow field [54]. A conceptual flow map of the Monte Carlo simulation used here is shown in Figure 4- 1:. The simulation is based on investigating the uncertainty of the system output by perturbing every input parameter into the system. These include the shape, number density and intensity of the seeded particles, their displacement over a pair of images and background white noise in the image. A high number of simulations $O(200-800)$ is run for investigating the effect of every individual input in velocity calculation uncertainty of the system.

The present 3C3D velocity measurement technique has unique features and the approach for measurement of velocity in micro channel flows including the use of only a single camera to capture planar images of particle locations that are stacked and form the volumes of intensity. This is achieved by scanning through the depth of micro channel with a thin focal plane field-of-view and high scanning rate relative to the particles' speed. The volumetric data is analyzed using a three-dimensional cross correlation algorithm on two successive volumes that determines the average movement of a group of particles within sub-volumes. By knowing the time and calculating the displacement between the two captured

volume sets a velocity vector field can be determined. While the processing of the particle displacement field to a vector field is an extension of 2D PIV, the unique nature of the data captured introduces its own unique sources of uncertainty.

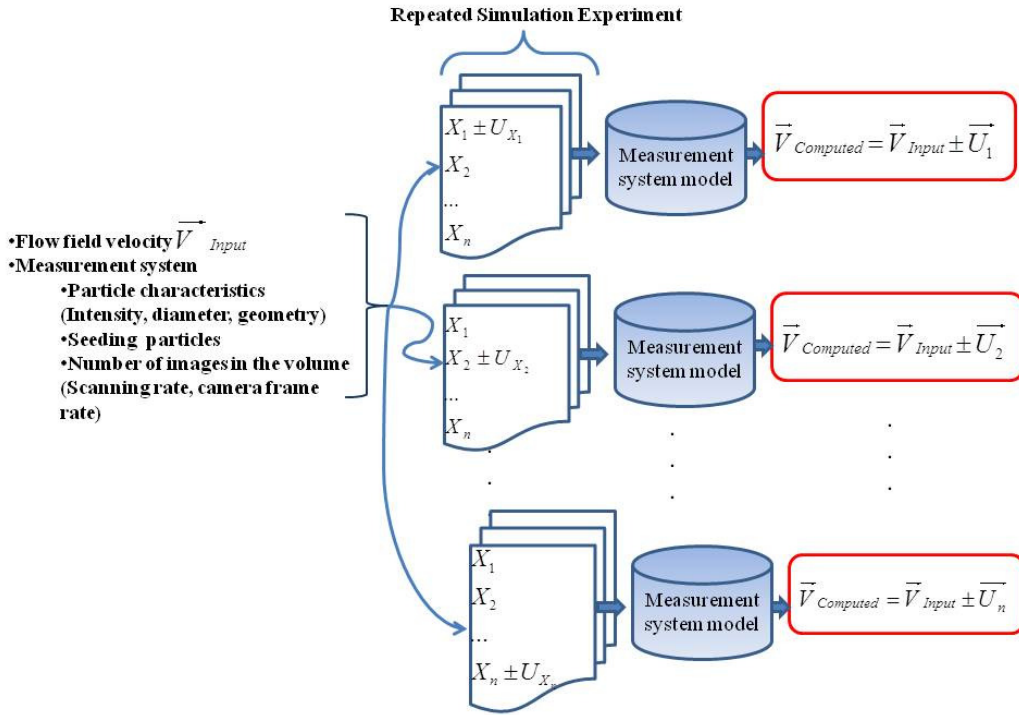


Figure 4- 1: A conceptual flow map of the Monte Carlo simulation used

The first main challenge in determining the uncertainty of the 3C3D measurement system is determining the accuracy of correlating the intensity volumes. The seeded particles fluoresce with a three-dimensional Gaussian intensity that the scanning system captures images of at discrete depths. By stacking these images, the constructed volumetric intensity of a particle appears as a stretched rod of illumination with diffraction rings around it. The first stage of

the uncertainty investigation is dedicated to the shape of the particle intensities. Synthetic images of the flow field are built using two types of particle intensity: with a 3D Gaussian intensity in a spherical geometry which models a more ideal case and a 2D Gaussian intensity in cylindrical geometry with finite length and diameter to better represent the real captured data. An investigation studying the shape of the correlation maps generated for the different shaped particles will be used to assess that ability of the cross correlation approach to determine the displacement of the particles. The generated 3D Gaussian intensity of spherical particles will be used as the ideal model to assess the impact of particle shape.

An uncertainty analysis using the 3D Gaussian intensity particles is also performed to investigate the effect of other parameters including particle density, background white noise and particle displacement perturbation on the calculated flow velocity vector field. The impact of these input perturbations on the overall uncertainty will be assessing along with the effect on the generated correlation maps.

A schematic of the general approach in the Monte Carlo simulation is shown in Figure 4- 2. A uniform in-plane and out-of-plane velocity flow field is modeled by displacing a particle field over two intensity volumes. The first volume is defined as a single interrogation window size of $64 \times 64 \times 64$ voxels, which typically used in PIV. This volume is randomly seeded with particles with defined size and Gaussian shape to represent the capture flux of light from a particle set. A second volume is generated of the same particles that have displaced

by the prescribed amount of the velocity field. Rather than working in real space, the simulation is conducted in voxel space for displacement and a single unit of time is used between the simulated volumes. The determined particle displacement is equal to the velocity, per unit time.

The three dimensional cross correlation algorithm used is extended from a 2D fast normalized cross correlation. The correlation maxima or peak represents the average displacement within the volume. This location is determined using a three-point volumetric Gaussian peak detection based on a three-point two-dimensional Gaussian regression. Finally, the velocity vector field is determined by relating the center of the flow field voxel to the detected peak.

Each of these steps is described in detail below. The aim here is to highlight important issues in the process of collecting data, processing and calculation of velocity.

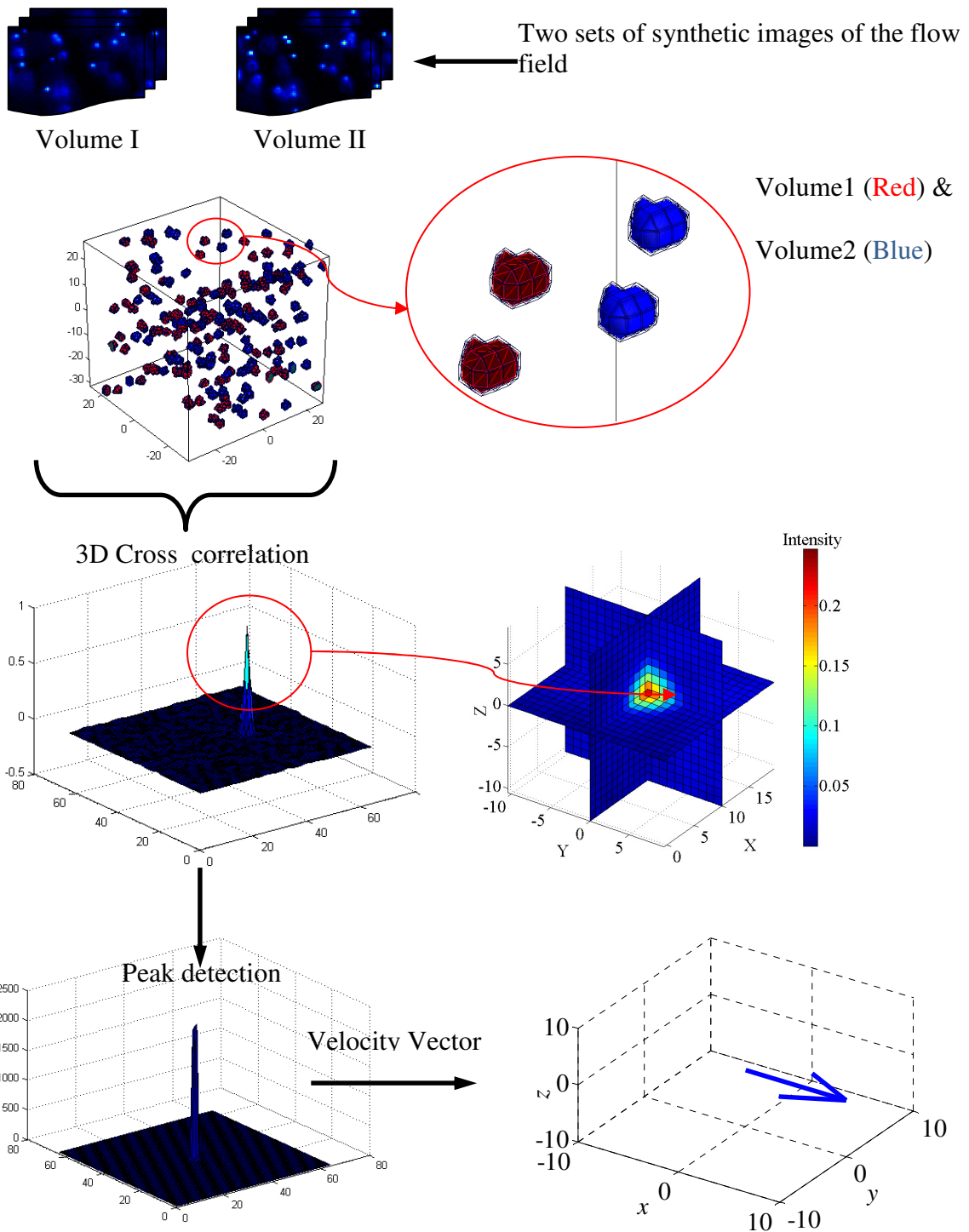


Figure 4- 2: Schematic of data generate and processing for the Monte Carlo simulation

4.3 Synthetic intensity volume generation

Approaches that could and have been used to generate synthetic images are described here. The first intensity volume is generated by randomly seeding the volume particle of known size with Gaussian intensity in the three-dimensional flow field. The second intensity volume is built by the displacement of the seeded particles in the first volume intensity over the definite time interval, here defined as one time unit. In each case the volume used is $64 \times 64 \times 64$ voxels.

4.4 Particle intensity construction

Fluorescent particles are used as seed particles in micro-velocity measurement techniques to achieve a sharp particle image against the bulk flow field and avoid optical imaging limitations of objects that are near the diffraction limit of the optics. To illustrate this, examples of experimentally collected images of particles are shown in Figure 4- 3.

Figure 4- 3(a) shows two images collected at two depths above and below focal plane where the particle is in sharp focus. The diffraction rings due to lens aberration of the defocused particle due the distance from the image plane is observable.

Figure 4- 3(b) shows the 3D Gaussian intensity obtained from a $1\mu\text{m}$ fluorescent particle. This volume of intensity for this single particle is constructed from

images collected from the system scanned through the entire volume of a diluted fluorescent particles solution placed stationary between two glass slides.

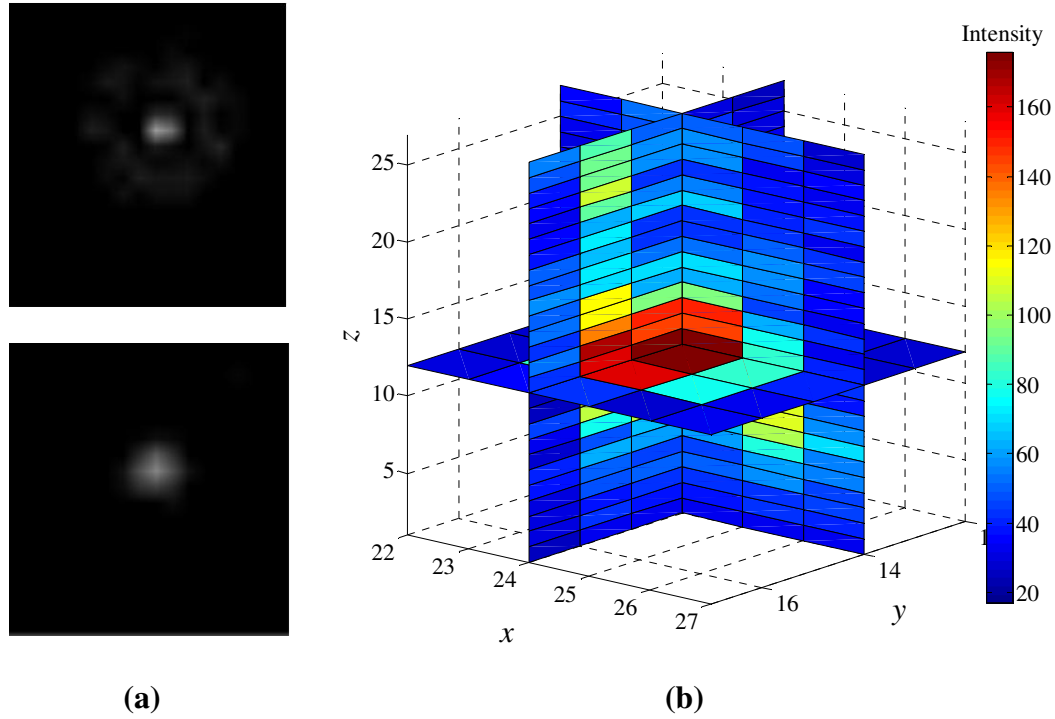


Figure 4- 3: (a) Images of a 1 μ m fluorescent particle at $z = -9\mu$ m below (top) and $z = 23\mu$ m above focal plane (bottom) (b) constructed 3D Gaussian intensity

Fluorescent particles that are seeded in the flow field are observed to demonstrate a three-dimensional Gaussian intensity. For the simulation using Gaussian particles the following equation is used to describe the particle intensity which is an extension of a 2D Gaussian intensity

$$I(x, y, z) = I_0 \exp \left[\frac{-(x-x_c)^2 - (y-y_c)^2 - (z-z_c)^2}{(1/8)d_\tau^2} \right] \quad (4- 2)$$

where I_0 is the peak intensity and (x_c, y_c, z_c) is the center of the particle in the intensity volume and d_r is the particle image diameter. Here, d_r is defined by e^{-2} of intensity value of the scattered Gaussian light.

In the scanning 3C3D technique, the illumination is provided volumetric by a continuous wave (CW) laser and the region-of-interest is defined by the position of the focal plane of the objective lens of the microscope. This is as opposed to standard PIV where the region-of-interest is defined by the viewing region of the camera and the position of a laser light sheet. Exposure time of the camera and laser power would be adjusted to maximize the signal level. Therefore, I_0 is assumed to be constant and equal to the constant of 255 in the simulation which is equivalent to the maximum signal from an 8 bit CCD.

To simplify the calculation in the simulation, the magnification factor is chosen to be unity, meaning that the physical dimension is equal to the dimension in the generated images Figure 4- 4(a) shows an example particle with the normalized volumetric Gaussian intensity of the light fluorescing from the spherical shape particle. It is observed that the light is illuminating a number of pixels more than the diameter of the physical particle. Slices of the in-plane field at different depths are shown in Figure 4- 4 (a), (b). Notice that there is also an effect of diffraction rings appearing in the captured images where depth = 0 denotes imaging within the focal plane and positive depths indicate being above the plane and vice versa. Taking slices of the images of the intensity of the semi-spherical

particle through depth and stacking them together to build a discretized volume of the intensity of the particles results in a semi-cylindrical intensity of the particle. In order to investigate the effect of parameters involved in the flow field measurement uncertainty, a Monte-Carlo simulation using 3D Gaussian intensity particles that is described by equation (4- 2) is carried out. In addition, in order to evaluate the effect of the 3D Gaussian intensity of the tracer particles in the proposed 3C3D system, two types of spherical and cylindrical particles are generated as well which described in the following sections.

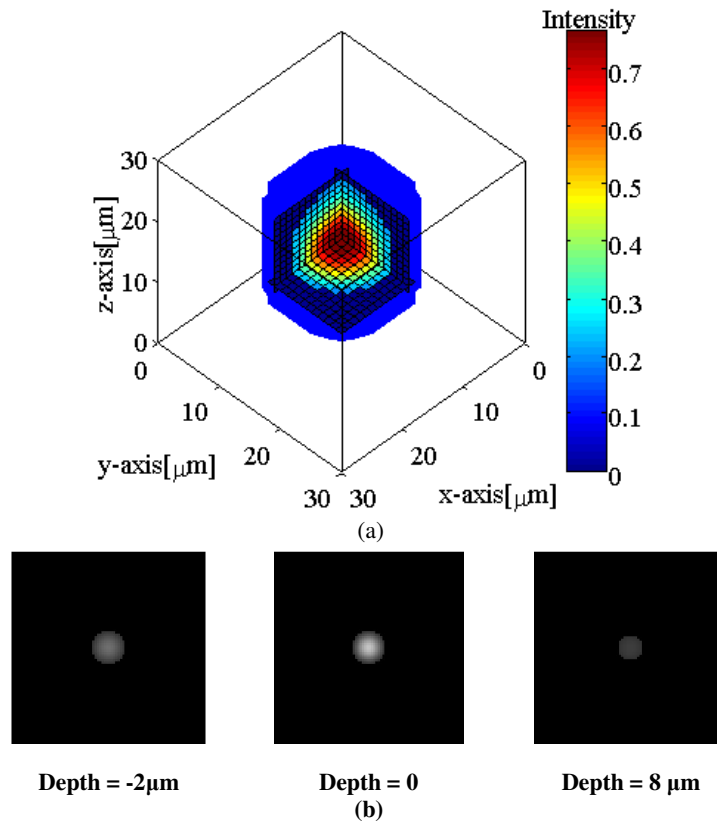


Figure 4- 4: Gaussian intensity particle (a) 3D shape(b)Image slices at different depths

4.5 Spherical intensity particle

Spherical particles are generated with a fitted 3D Gaussian intensity. The 3D Gaussian intensity function is described by:

$$I(x, y, z) = I_0 \exp(-[(x - x_c)^2 + (y - y_c)^2 + (z - z_c)^2]) \quad (4-3)$$

where I_0 is the maximum intensity observed by the optics.

This 3D Gaussian intensity is restricted in the spherical particle with physical diameter of d_p that is followed by:

$$(x - x_c)^2 + (y - y_c)^2 + (z - z_c)^2 \leq \frac{d_p^2}{4} \quad (4-4)$$

where the position of the particle is at coordinate system of (x_c, y_c, z_c) in the flow field. The three dimensional constructed intensity of a spherical particle with the diameter of $d_p = 3\mu m$ is shown in the Figure 4- 5.

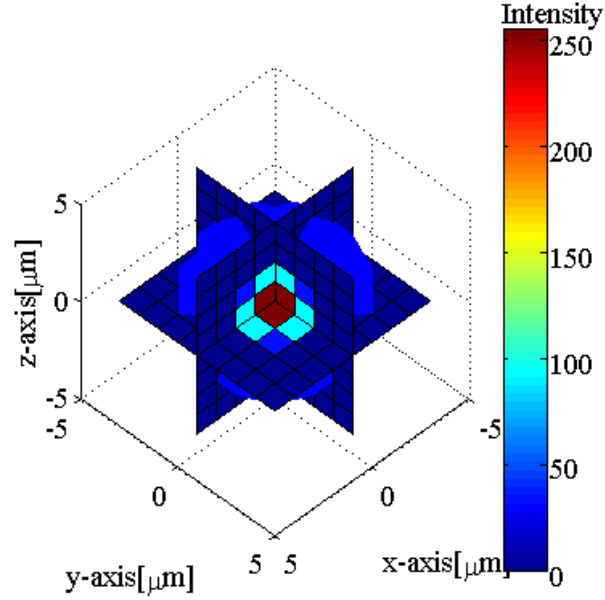


Figure 4- 5: 3D Spherical fluorescent particle

4.6 Cylindrical intensity particles

The constructed cylindrical intensity are generated using a 2D Gaussian intensity for spatial variables that are in-plane to the camera with the following equation that is then extruded through a depth with I_0 as the maximum intensity observed by the optics.

$$I(x, y, z) = I_0 \exp(-[(x - x_c)^2 + (y - y_c)^2]) \quad (4- 5)$$

The physical geometry of the cylinder with the length of l_z and diameter of d_p is such that:

$$(x - x_c)^2 + (y - y_c)^2 \leq \frac{d_p^2}{4} \text{ and } -\frac{l_z}{2} \leq z - z_c \leq \frac{l_z}{2} \quad (4-6)$$

As an example, volumetric constructed intensity of a cylindrical particle with the diameter of $d_p = 3\mu\text{m}$ and length of $l_z = 16\mu\text{m}$ is shown in the Figure 4- 6. The diameter and depth of this particle will be used to model particles that have been observed in experiments.

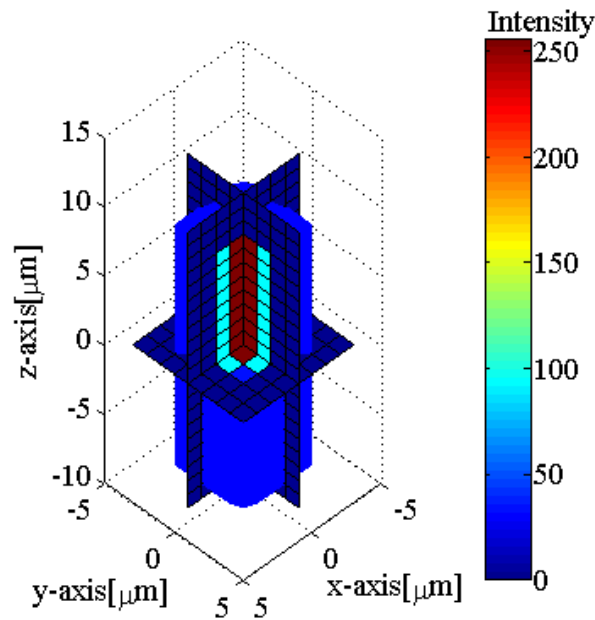


Figure 4- 6: cylindrical intensity particle

4.7 Seeded flow field

The idealized synthetic particles are uniformly seeded at random locations in the volumetric flow field disregarding inter particle forces. This was chosen to be

84×84×84 voxels, to provide a padded region around the interrogation volume of 64×64×64 voxels which was extracted from the center of the larger volume. The second volumetric particle field was determined by applying a known velocity (or displacement) field to the first volume of particles. The padded region allowed particles to move into and out of the region-of-interest depending on the velocity. Figure 4- 7 shows an example of two generated intensity volumes of the positions of the seeded particles intensities that show the first position in red and the second in blue. The region of interest is the size of interrogation window being used in cross correlation that results in obtaining one velocity vector. Therefore, in order to evaluate the accuracy of the measurement system only a uniform displacement with the region-of-interest is used because interrogation window only gives one vector which is from the center of the interrogation window to the highest peak. Therefore, for any other type of flow regimes the size of interrogation window can be changed and the velocity vectors describe the total flow velocity vectors.

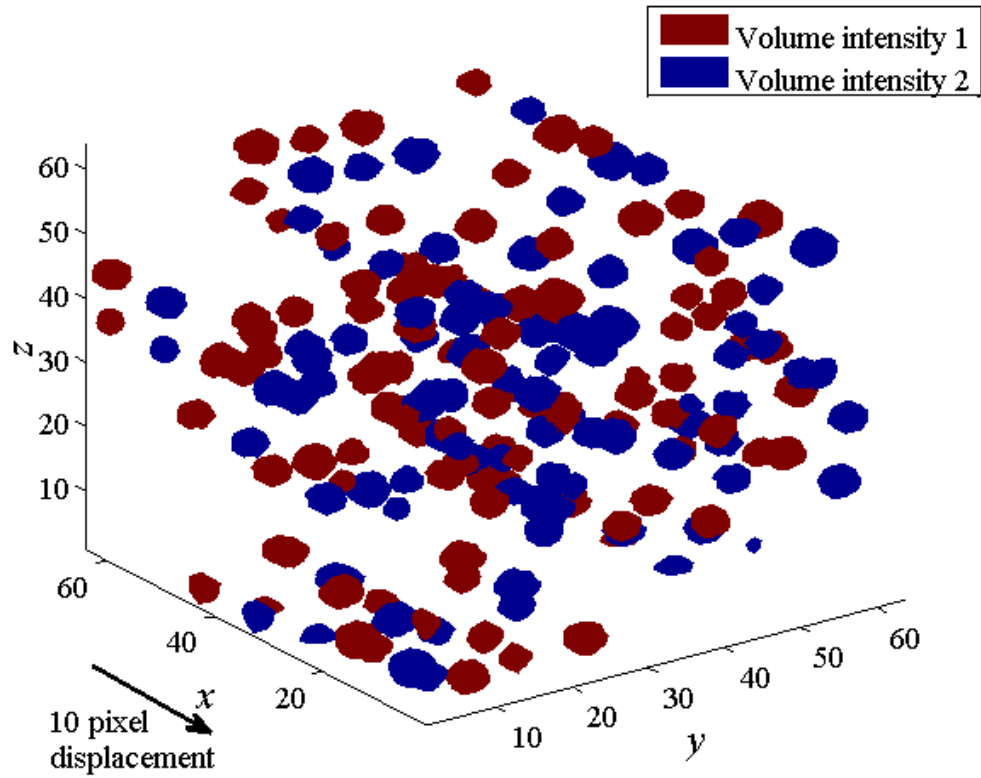


Figure 4- 7: Two volumes of intensities of the generated particles (Blue: initial, Red: the second positions of the particles)

Figure 4- 8 shows the images for two corresponding intensity volumes 1 and 2 at one depth. The shift of the particles between two images is observable in Figure 4- 8.

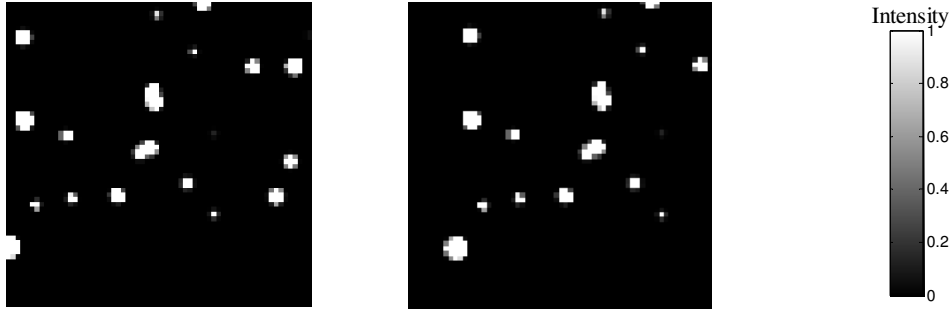


Figure 4- 8: synthetic images captured at one depth for two intensity volumes (a) 1st scan (b) 2nd scan

4.8 Three-dimensional cross correlation algorithm

The algorithm used here to determine the average displacement within the region-of-interest is a 3D fast normalized cross correlation. The motivation for this cross correlation is template matching by the Euclidean distant measurement. In equation (4- 7), the squared Euclidean distance, S^2 , for two three-dimensional functions $I(x, y, z)$ and $I'(x + \Delta x, y + \Delta y, z + \Delta z)$ is expressed as:

$$S_{I,I'}^2(x, y, z) = \sum_{x,y,z} [I(x, y, z) - I'(x + \Delta x, y + \Delta y, z + \Delta z)]^2 \quad (4- 7)$$

Given, I is the voxel intensity over the sum of x, y, z and I' voxel intensity over the sum of $x + \Delta x, y + \Delta y, z + \Delta z$, this equation can be expanded to

$$S_{I,I'}^2(x, y, z) = \sum_{x,y,z} [I^2(x, y, z) - 2I(x, y, z)I'(\Delta x, \Delta y, \Delta z) + I'^2(\Delta x, \Delta y, \Delta z)] \quad (4- 8)$$

The two terms of $\sum_{x,y,z} I^2(x, y, z)$, and $\sum_{x,y,z} I'^2(\Delta x, \Delta y, \Delta z)$ are approximately constant and therefore the cross correlation function is modified in the equation below to indicate the measure of the similarity between the image and feature.

$$S_{I,I'}^2(x, y, z) = \sum_{x,y,z} [I(x, y, z) - I'(x + \Delta x, y + \Delta y, z + \Delta z)]^2 \quad (4-9)$$

$$R(x, y, z) = \sum_{x,y,z} I(x, y, z) I'(\Delta x, \Delta y, \Delta z) \quad (4-10)$$

There are several disadvantages of using the equation (4-10) including a lack of invariant dependence of the correlation function, $R(x, y, z)$ to the size of the feature and to the non-uniform light condition of the template. Therefore, above cross correlation function is improved to the normalized cross-correlation function, a unit vector such that:

$$R(x, y, z) = \frac{\sum_{i,j,k} [I(x, y, z) - \bar{I}(x+i, y+j, z+k)][I'(i, j, k) - \bar{I}']}{\left\{ \sum_{i,j,k} [I(x, y, z) - \bar{I}(x+i, y+j, z+k)]^2 \sum_{i,j,k} [I'(i, j, k) - \bar{I}']^2 \right\}^{0.5}} \quad (4-11)$$

where \bar{I} and \bar{I}' are the mean of I and I' respectively.

The numerator of the normalized correlation function, $R(x, y, z)$, is computed by taking the Fourier transform of the feature and the conjugate template to expand it to the frequency domain and then by taking the inverse Fourier the equation, the results are explained in the time domain such that:

$$R_{\text{numerator}}(x, y, z) = F^{-1}\{F(I(x, y, z) - \bar{I}(x+i, y+j, z+k))F^*(I'(i, j, k) - \bar{I}')\}$$

(4-12)

where $F^*(g) = F(g^*)$.

The normalized cross correlation, $R(x, y, z)$, has been used in the velocity calculation of the flow field. For the cross correlation calculations performed in this thesis, the size of interrogation window remained the same, there was no overlaps between cross-correlation of two intensity volumes.

4.9 Peak detection

The maxima or peak in the correlation volume describes the average displacement, magnitude and direction from the center of the region-of-interest and by knowing the time scale of the experiment between the two particle volumes, the flow field velocity vector is obtained. In order to find the displacement with a sub-voxel accuracy, a 3D curve is fitted to the correlation volume function at the maximum point. Here, a multiple regression or multivariate regression analysis is performed to approximate the uncertainty of the fitting data to the curve function. A three-dimensional elliptical Gaussian function with sub-pixel resolution generalized from a two-dimensional Gaussian regression is fitted to the correlation map at the maximum value point. The peak is detected by using three-point curve fitting in the neighborhood of the found maximum point in the correlation map.

A three point estimator in a 2D-Gaussian curve fitted to correlation data at the highest value and to two neighborhoods was introduced that shown an estimation for 2D-particle displacement from a cross correlation algorithm in PIV measurement by using 2D-Gaussian regression explicit formulation [55]. In this study, the developed three-dimensional cross correlation function was in applying a 3D elliptical Gaussian intensity function to detect the cross correlation peak. Therefore, an explicit volumetric three point peak detection estimation is performed by developing formulation for a three point three- dimensional Gaussian regression.

Figure 4- 9 plots the three point estimator of an elliptical Gaussian fit in one direction. In this method, the maximum of the cross correlation data points is searched, then a 3D elliptical Gaussian intensity is fitted to the maximum point, f_0 , then the peak is estimated by using a three point estimation around this point using points f_{-1} and f_{+1} .

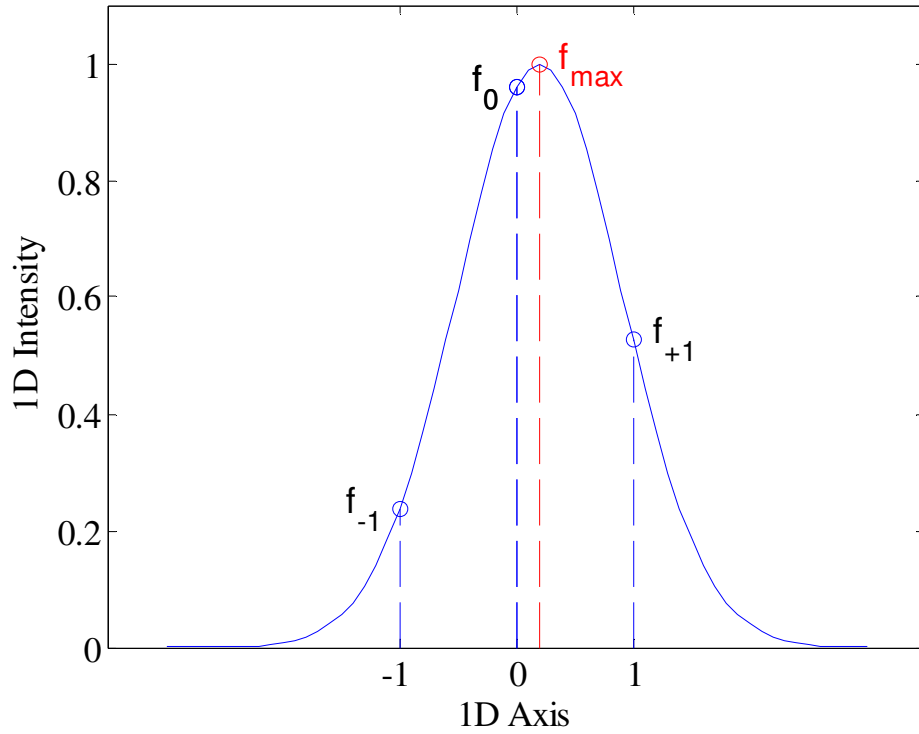


Figure 4- 9: Elliptical Gaussian curve, f , along x -axis fitted at the origin and finding the peak using three-point estimation

The detected peak is located at $[\Delta x, \Delta y, \Delta z]$ offset from the origin that the origin is the maximum points found in correlation function, (x_0, y_0, z_0) . The equation (4- 13) demonstrates the fitted three-point three-dimensional Gaussian intensity curve at the maximum point which is the origin of the function f .

$$f(x, y, z) = \beta \exp\{\alpha_{200}(x - \Delta x)^2 + \alpha_{020}(y - \Delta y)^2 + \alpha_{002}(z - \Delta z)^2 + \alpha_{110}(x - \Delta x)(y - \Delta y) + \alpha_{101}(x - \Delta x)(z - \Delta z) + \alpha_{011}(y - \Delta y)(z - \Delta z)\}$$

(4- 13)

where α_{ijk} is the coefficient of the elliptical term $x^i y^j z^k$ that $i, j, k = 0,1,2$ and β is the coefficient of the exponential Gaussian fitted function. Equation (4- 13) was expanded into the following equation:

$$f(x, y, z) = \exp[\beta_{000} + \beta_{100}x + \beta_{200}x^2 + \beta_{020}y^2 + \beta_{002}z^2 + \beta_{110}xy + \beta_{101}xz + \beta_{011}yz] \quad (4- 14)$$

where

$$\beta_{000} = \ln(\beta) + \alpha_{200}\Delta^2x + \alpha_{020}\Delta^2y + \alpha_{002}\Delta^2z + \alpha_{110}\Delta x\Delta y + \alpha_{101}\Delta x\Delta z + \alpha_{011}\Delta y\Delta z \quad (4-15)$$

$$\beta_{100} = -2\alpha_{200}\Delta x - \alpha_{110}\Delta y - \alpha_{101}\Delta z \quad (4-16)$$

$$\beta_{010} = -2\alpha_{020}\Delta y - \alpha_{110}\Delta x - \alpha_{011}\Delta z \quad (4-17)$$

$$\beta_{001} = -2\alpha_{002}\Delta z - \alpha_{011}\Delta y - \alpha_{101}\Delta x \quad (4-18)$$

and $\beta_{200} = \alpha_{200}$, $\beta_{020} = \alpha_{020}$, $\beta_{002} = \alpha_{002}$, $\beta_{110} = \alpha_{110}$, $\beta_{101} = \alpha_{101}$, $\beta_{011} = \alpha_{011}$.

The minimum of the Euclidean norm of the logarithmic intensity function, $f(x, y, z)$, gives:

$$L_2 = \sqrt{\sum_{i,j,k=-1}^1 [\beta_{000} + \beta_{200}i^2 + \beta_{100}i + \beta_{010}j + \beta_{020}j^2 + \beta_{001}k + \beta_{002}k^2 + \beta_{101}ik + \beta_{110}ij + \beta_{011}kj]^2 - \ln(f_{x+i,y+j,z+k})} \quad (4-19)$$

where

$$\beta_{100} = \frac{1}{6} \sum_{i,j,k=-1}^1 i \ln(f_{x+i,y+j,z+k}) \quad (4-20)$$

$$\beta_{010} = \frac{1}{6} \sum_{i,j,k=-1}^1 j \ln(f_{x+i,y+j,z+k}) \quad (4-21)$$

$$\beta_{001} = \frac{1}{6} \sum_{i,j,k=-1}^1 k \ln(f_{x+i,y+j,z+k}) \quad (4-22)$$

$$\beta_{110} = \frac{1}{4} \sum_{i,j,k=-1}^1 ij \ln(f_{x+i,y+j,z+k}) \quad (4-23)$$

$$\beta_{011} = \frac{1}{4} \sum_{i,j,k=-1}^1 jk \ln(f_{x+i,y+j,z+k}) \quad (4-24)$$

$$\beta_{101} = \frac{1}{4} \sum_{i,j,k=-1}^1 ik \ln(f_{x+i,y+j,z+k}) \quad (4-25)$$

$$\beta_{200} = \frac{1}{6} \sum_{i,j,k=-1}^1 (3i^2 - 2) \ln(f_{x+i,y+j,z+k}) \quad (4-26)$$

$$\beta_{020} = \frac{1}{6} \sum_{i,j,k=-1}^1 (3j^2 - 2) \ln(f_{x+i,y+j,z+k}) \quad (4-27)$$

$$\beta_{002} = \frac{1}{6} \sum_{i,j,k=-1}^1 (3k^2 - 2) \ln(f_{x+i,y+j,z+k}) \quad (4-28)$$

$$\beta_{000} = \frac{1}{9} \sum_{i,j,k=-1}^1 (5 - 3i^2 - 3j^2 - 3k^2) \ln(f_{x+i,y+j,z+k}) \quad (4-29)$$

From above equations, the peak distance from the maximum of the correlation function is determined:

$$\Delta x = \frac{\beta_{100}(4\beta_{002}\beta_{020} - \beta_{011}^2)}{2(\beta_{200}\beta_{011}^2 - \beta_{011}\beta_{101}\beta_{110} + \beta_{020}\beta_{101}^2 + \beta_{002}\beta_{110}^2 - 4\beta_{002}\beta_{020}\beta_{200})} \quad (4-30)$$

$$- \frac{\beta_{010}(2\beta_{002}\beta_{110} - \beta_{011}\beta_{101})}{2(\beta_{200}\beta_{011}^2 - \beta_{011}\beta_{101}\beta_{110} + \beta_{020}\beta_{101}^2 + \beta_{002}\beta_{110}^2 - 4\beta_{002}\beta_{020}\beta_{200})}$$

$$+ \frac{\beta_{001}(\beta_{011}\beta_{110} - 2\beta_{020}\beta_{101})}{2(\beta_{200}\beta_{011}^2 - \beta_{011}\beta_{101}\beta_{110} + \beta_{020}\beta_{101}^2 + \beta_{002}\beta_{110}^2 - 4\beta_{002}\beta_{020}\beta_{200})}$$

$$\Delta y = \frac{\beta_{010}(4\beta_{002}\beta_{020} - \beta_{011}^2)}{2(\beta_{200}\beta_{011}^2 - \beta_{011}\beta_{101}\beta_{110} + \beta_{020}\beta_{101}^2 + \beta_{002}\beta_{110}^2 - 4\beta_{002}\beta_{020}\beta_{200})} \quad (4-31)$$

$$- \frac{\beta_{100}(2\beta_{002}\beta_{110} - \beta_{011}\beta_{101})}{2(\beta_{200}\beta_{011}^2 - \beta_{011}\beta_{101}\beta_{110} + \beta_{020}\beta_{101}^2 + \beta_{002}\beta_{110}^2 - 4\beta_{002}\beta_{020}\beta_{200})}$$

$$+ \frac{\beta_{001}(2\beta_{011}\beta_{200} - \beta_{101}\beta_{110})}{2(\beta_{200}\beta_{011}^2 - \beta_{011}\beta_{101}\beta_{110} + \beta_{020}\beta_{101}^2 + \beta_{002}\beta_{110}^2 - 4\beta_{002}\beta_{020}\beta_{200})}$$

$$\Delta z = \frac{\beta_{001}(4\beta_{002}\beta_{200} - \beta_{110}^2)}{2(\beta_{200}\beta_{011}^2 - \beta_{011}\beta_{101}\beta_{110} + \beta_{020}\beta_{101}^2 + \beta_{002}\beta_{110}^2 - 4\beta_{002}\beta_{020}\beta_{200})} \quad (4-32)$$

$$+ \frac{\beta_{100}(\beta_{011}\beta_{110} - 2\beta_{020}\beta_{101})}{2(\beta_{200}\beta_{011}^2 - \beta_{011}\beta_{101}\beta_{110} + \beta_{020}\beta_{101}^2 + \beta_{002}\beta_{110}^2 - 4\beta_{002}\beta_{020}\beta_{200})}$$

$$- \frac{\beta_{010}(2\beta_{011}\beta_{200} - \beta_{101}\beta_{110})}{2(\beta_{200}\beta_{011}^2 - \beta_{011}\beta_{101}\beta_{110} + \beta_{020}\beta_{101}^2 + \beta_{002}\beta_{110}^2 - 4\beta_{002}\beta_{020}\beta_{200})}$$

The peak height is calculated to be obtained from equation (4-33):

$$h = \exp(\beta_{000} - \beta_{200}\Delta^2 x - \beta_{020}\Delta^2 y - \beta_{002}\Delta^2 z - \beta_{110}\Delta x \Delta y - \beta_{101}\Delta x \Delta z - \beta_{011}\Delta y \Delta z)$$

(4-33)

The location of the peak is:

$$x_{peak} = x_0 + \Delta x$$

$$y_{peak} = y_0 + \Delta y \quad (4-34)$$

$$z_{peak} = z_0 + \Delta z$$

The accuracy of the peak detection function can be increased by increasing the number of point estimator. For instance, by adding two points in every direction, a five point Gaussian curve fitting approximation can be developed.

4.10 The Monte Carlo simulation

The Monte-Carlo simulation provides a beneficial understanding of uncertainty to the variations of the input parameters of the system. The generated artificial images of the seeded particle intensities with the known properties that include particle diameter, shape, density, displacement and background white noise are used for the simulation. By perturbing every individual parameter one at a time, artificial images of the particle intensity of the flow field are generated, processed and analyzed. The reliable measurement is obtained by the random seeding of the particles and the high number of simulation runs (O[200-800]). The equation below describes the effect of the number of the runs in the reliability of the measurement, as by defining Monte-Carlo standard uncertainty, u [7]:

$$u = \frac{z\sigma}{\sqrt{N}} \quad (4-35)$$

where $z=2$ suggests the confidence in the reliability of the results 95% and $z=3$ proposes a 99% confident in the reliability of the result. The standard deviation of the output parameter is σ with the number of simulation runs of N . To improve the Monte-Carlo uncertainty by 1%, the number of simulations must increase 10,000 times assuming that the standard deviation remains constant. The number of the runs for the simulations is selected to be at least in the order of a couple of hundred for the standard deviation of less than 0.01 for acquiring of 95% reliability [40].

The RMS uncertainty for the calculated flow field velocity, the main evaluation parameter used in the study is defined according to:

$$V_{RMS} = \sqrt{\frac{\sum_{j=1}^N (u_j - \bar{u})^2 + \sum_{j=1}^N (v_j - \bar{v})^2 + \sum_{j=1}^N (w_j - \bar{w})^2}{N}} \quad (4-36)$$

where V_{RMS} is calculated in 3D for each component of the velocity in Cartesian coordinate system, $\vec{V} = (u_{x,y,z}, v_{x,y,z}, w_{x,y,z})$, using Monte-Carlo analysis for N runs.

4.11 Results

In this section, the results of Monte-Carlo simulation are discussed in comparison of the correlation volumes, the particle density, the particle shapes and the input velocity perturbation, as well as the effect of background noise.

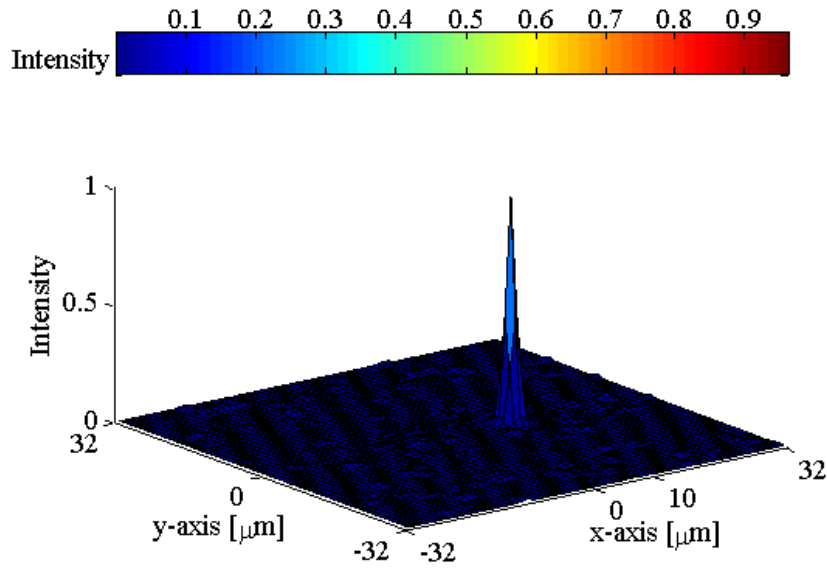
4.11.1 Effects of particle shape

In order to investigate the effect of stretched intensities of the particles in 3C3D scanning measurement technique, two types of particle intensities: 3D Gaussian spherical and 2D Gaussian cylindrical particle intensities are simulated. Then, the correlation volumes that result from these two types of particle intensities are compared. The effect on the shape correlation volume can have important implications of how well the peak detection operates and hence the uncertainty of displacement (velocity) estimation.

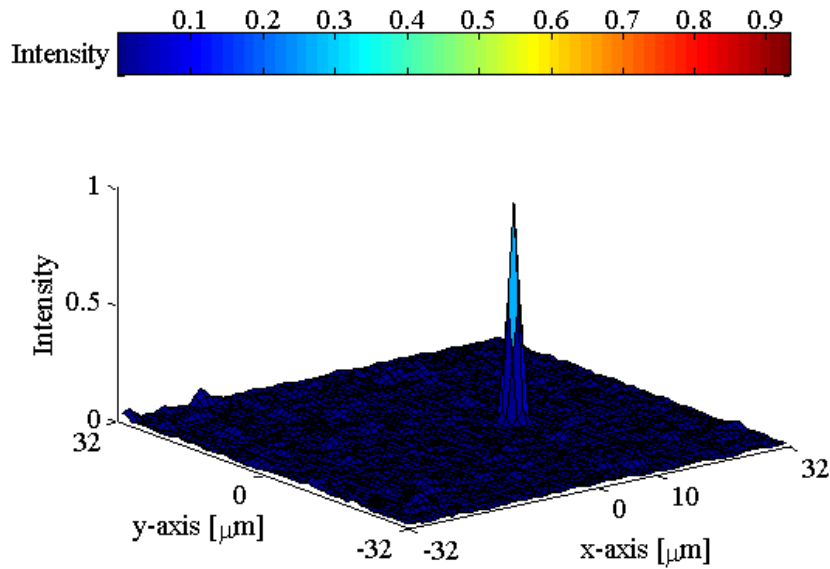
4.11.2 Correlation maps

In Figure 4- 10 (a) the planar ($x - y$) correlation maps for spherical, Figure 4- 10(b) cylindrical particles are plotted and these are compared to correlation maps in the out-of-plane direction ($y - z$) in Figure 4- 11. This comparison of the correlation maps expresses that the correlation map is stretched out along the depth, z -axis, i.e. the cylindrical particles' length. This is due to the uniform illumination in the z direction of the cylindrical particles. However, the location of the peak of the correlation map in both spherical and cylindrical particles is the

same in all three directions and is equal to the flow field displacement between two correlated intensity volumes.

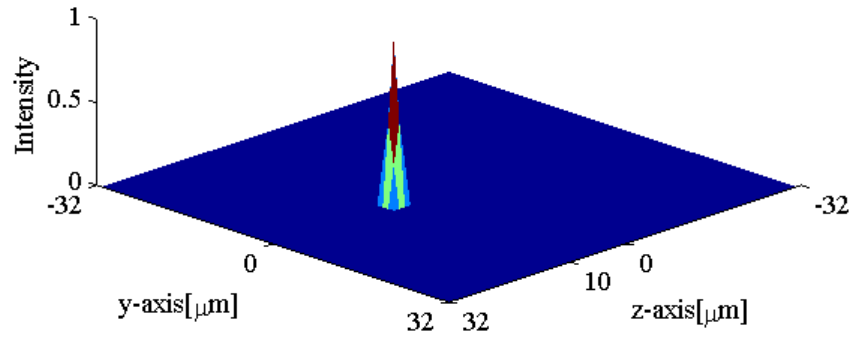


(a)

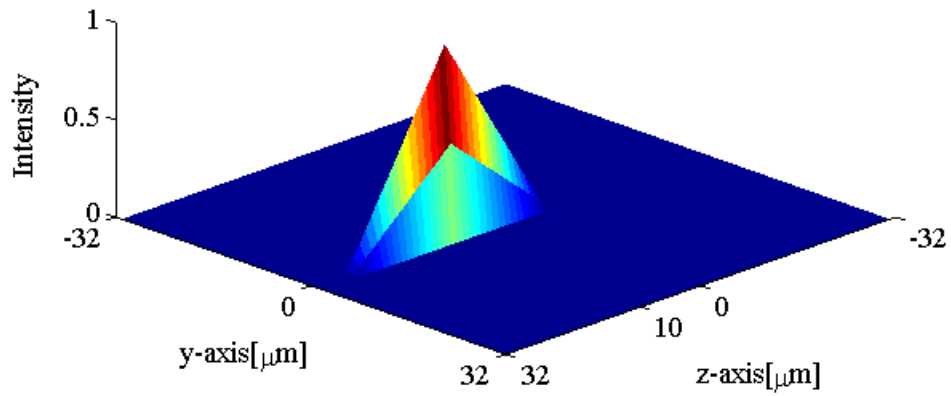


(b)

Figure 4- 10: Correlation map in x - y plane for velocity of $[10,0,0] \mu\text{m/s}$ obtained by synthetic images seeded by (a) spherical (b) cylindrical particle intensities at peak x coordinate



(a)



(b)

Figure 4- 11: Correlation maps in y-z plane at detected peak x coordinate for velocity of $[0,0,10] \mu\text{m/s}$ obtained from synthetic images using (a) spherical (b) cylindrical intensity volumes

To highlight the stretching of the correlation function, a 1D plot of the change of the correlation map's intensity along the depth, z , is plotted in Figure 4- 12. It is shown that the displacement value is the same for both plots and the intensity function is broader over the depth for the cylindrical case. The comparison between the full width of half maximum width (FWHM), $W_{50\% peak}$, for cylindrical and spherical in z direction has shown the difference between the two cases obtained by:

$$\frac{W_{50\% peak_cylindrical}}{W_{50\% peak_spherical}} = 7.08 \quad (4-37)$$

This shows that the cylindrical correlation map in z direction is stretched almost 7 times more than spherical case.

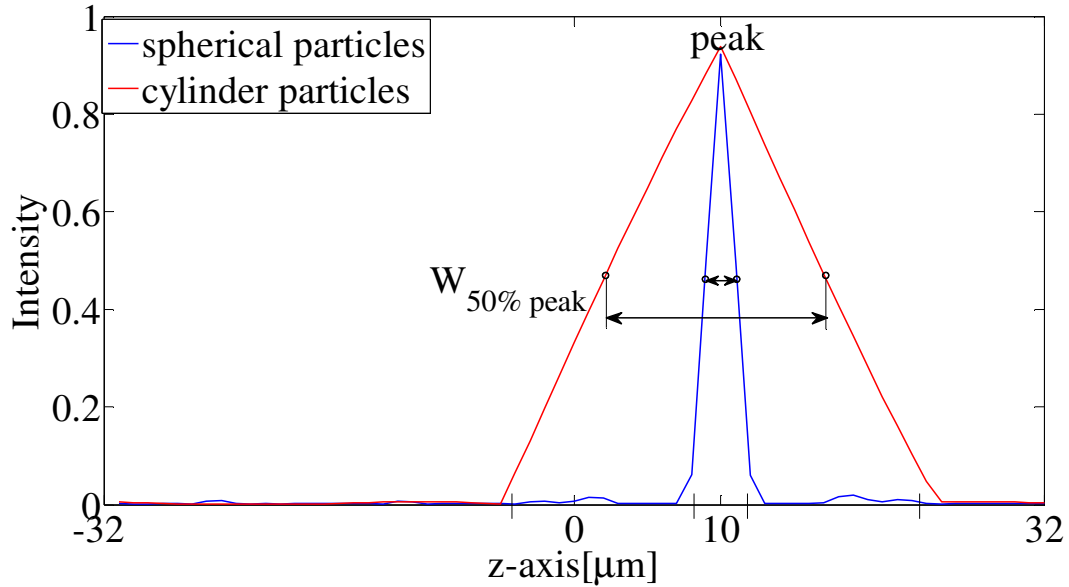
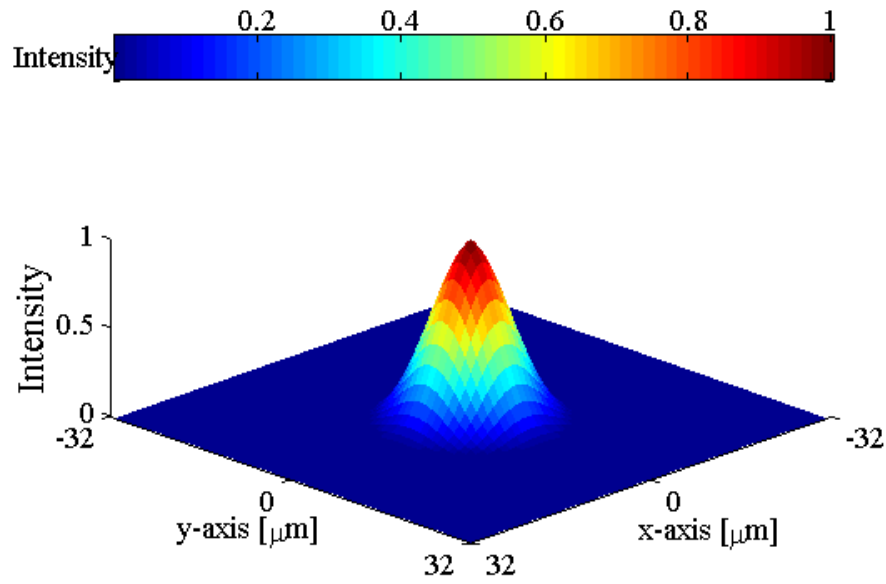
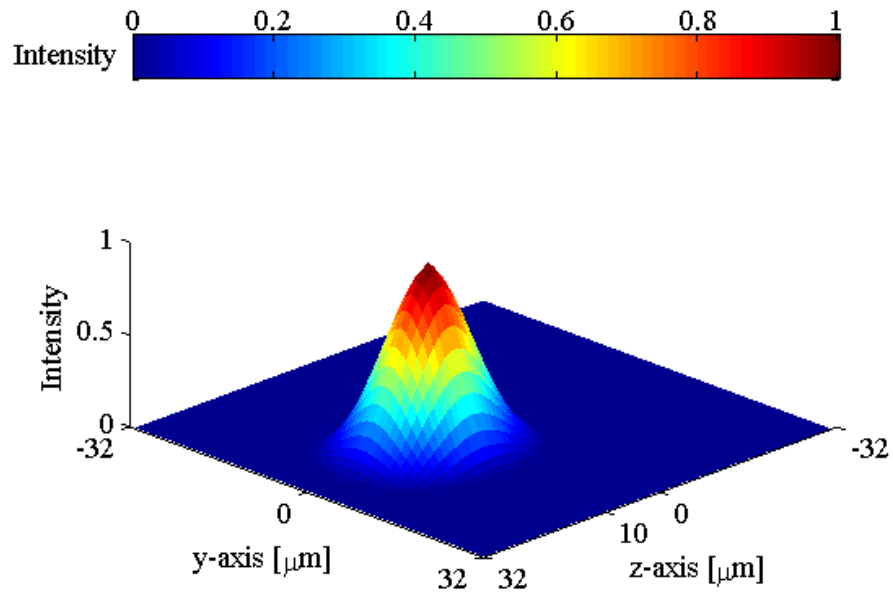


Figure 4- 12: 1D plot of correlation map along depth, z , at x, y detected peak coordinates for velocity of $[0,0,10]$ $\mu\text{m/s}$ for two particle intensity of spherical and cylindrical

3D Gaussian particles intensity particles developed by equation (4- 2) and shown in Figure 4- 4 are used for seeding the flow field. The correlation maps obtained from cross correlating this seeded flow field and is shown in Figure 4- 13 in $x-y$ and $y-z$ planes. As it is observable, the correlation maps are stretched along x , y , and z axes. This confirms the effect of the triangle correlation maps for the flow field seeded with cylindrical tracers that the stretched of the intensity was along the length of the cylinder.



(a)



(b)

Figure 4- 13 : Correlation maps in x - y plane at detected peak x coordinate for velocity of $[0,0,10] \mu\text{m/s}$ obtained from synthetic images using a 3D Gaussian particle with particle diameter of $d_\tau = 3$ voxel

4.11.3 Effect of particle diameter

Figure 4- 14 shows the effect of the particle image diameter on the uncertainty calculation of velocity using the developed 3D cross correlation algorithm and three-point three dimensional Gaussian peak detection. As the particle diameter increases from sub-voxel, 0.1, to over one voxel size for a fixed particle per voxel density (PPV), the uncertainty decreases. The smaller particle size raises the effect that the displacement becomes biased towards the integral values. This is compounded by only using a three-point Gaussian peak detection with sub-pixel resolution that estimates the particle's position with higher uncertainty for the small size particles.

The uncertainty increases with the increase of particle diameter to the value over 2 voxels. The particle image diameter of 10 pixels results in 0.1 uncertainties in velocity measurement and this increase in uncertainty is due to overlapping the particles illumination for the fixed amount of particle density.

This observation suggests a range for optimum particle image diameter in velocity measurement that the uncertainty contains the minimum value. The optimum particle diameter is between $d_r = 1.5 - 2$ voxels. This result is comparable to the results obtained from Monte-Carlo simulation on digital cross correlation PIV with simulation parameters of no noise, optimum exposure, top-hat light sheet profile, and image depth of $QL = 8$ bits/pixels. Using the single exposure/double frame PIV synthetic imaging evaluated the optimum particle

diameter of slightly more than 2 pixels; however, the double exposure/single frame PIV imaging showed the optimum diameter around 1.5 pixels. The significant conclusion from this result is particle image size of 2-3 voxels in 3D cross correlation and three-point peak detection gives the uncertainty less than 0.01.

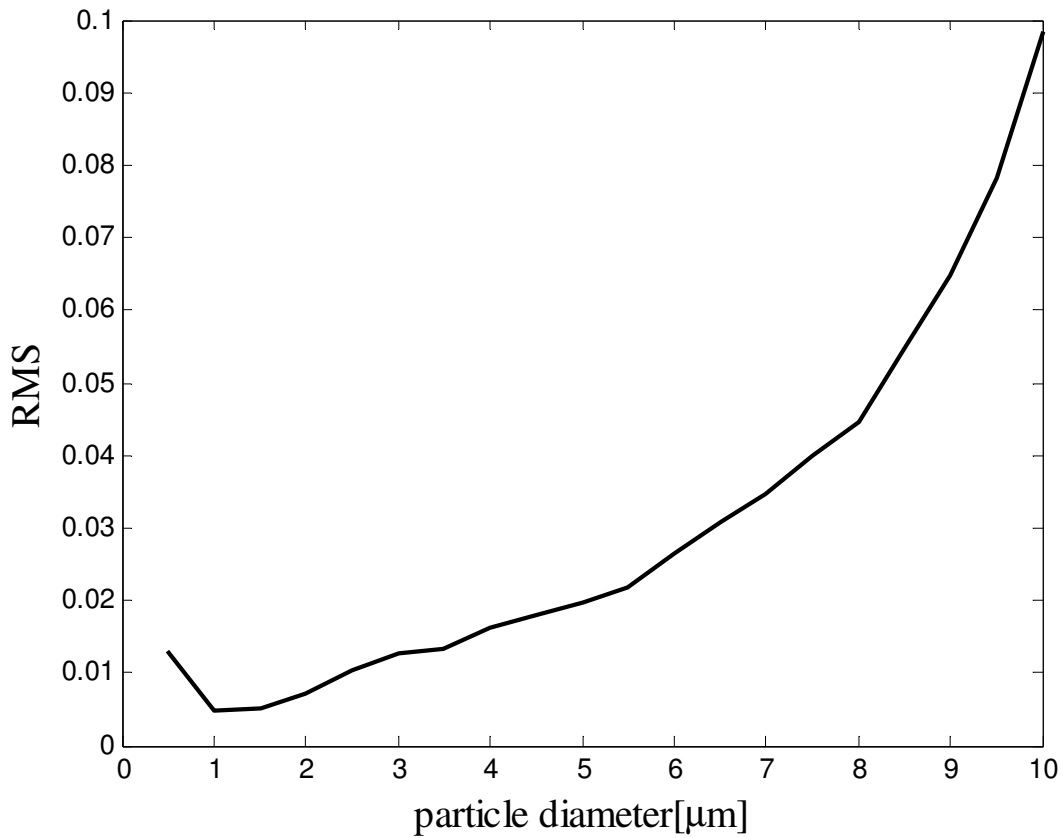


Figure 4- 14: Uncertainty measurement (RMS uncertainty) as a function of particle image diameter, d_p , with Monte-Carlo simulation parameters: number of simulation runs of $N = 200$, particle density of 1.1×10^{-3} PPV, $QL=8\text{bits/pixel}$, no noise

4.11.4 Effect of particle density

Particle density provides beneficial information in evaluating the operation of any 3C3D technique including providing sufficient data for cross correlation with the least uncertainty for both in-plane and out-of-plane displacement. Figure 4- 15 shows the change of RMS uncertainties versus the particle per voxel density. The minimum required number of particles for the conditions described in the simulation that include particles of diameter 2 voxels and $QL = 8$ bits/ pixels that the RMS uncertainty becomes stable to the value less than 0.01 was obtained to be $0.001\mu m^{-3}$. This is equivalent to 300 particles in the $64 \times 64 \times 64$ voxels of the region-of-interest. The effect of the high particle density causes higher spatial sampling rate of the flow followed by the higher spatial resolution. This also results in the higher signal ratios for the correlating intensities' volumes that increase the strength of the peak signal in the correlation volume.

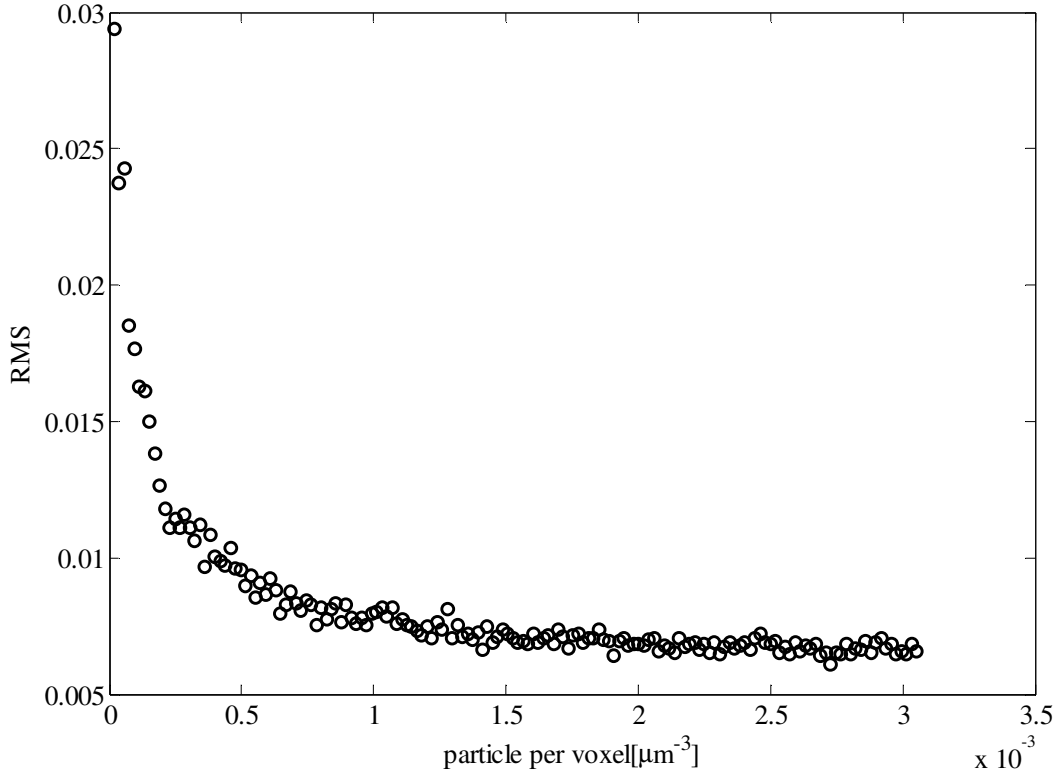


Figure 4- 15: Uncertainty measurement (RMS uncertainty) as a function of particle density per voxel (PPV) with Monte-Carlo simulation parameters: $d_\tau = 2.0$ voxel, QL= 8bits/pixel, $N = 200$ and $\vec{V} = [10,0,0]$ $\mu\text{m/s}$, no noise

4.11.5 Effect of particle displacement perturbation

The 3C3D cross correlation algorithm is a statistical displacement measurement due to the nature of cross correlation of two intensity volumes. This expresses the fact that all the particles that are appeared in the first intensity volume are not necessarily appear in the second intensity volume and have a standard deviation from flow field bulk velocity although the mean displacement per second of each particle is about the flow field velocity. Therefore, a set of simulations is performed for the different standard deviation distributed over the seeded particles

velocity in the flow field and the results are presented in Figure 4- 16. It is observed that by increasing the standard deviation of the seeded particles in the flow field the RMS is also increased by a lower ratio. This is almost a linear relation between the calculated measurement uncertainty (RMS) and the input standard deviation of the flow field.

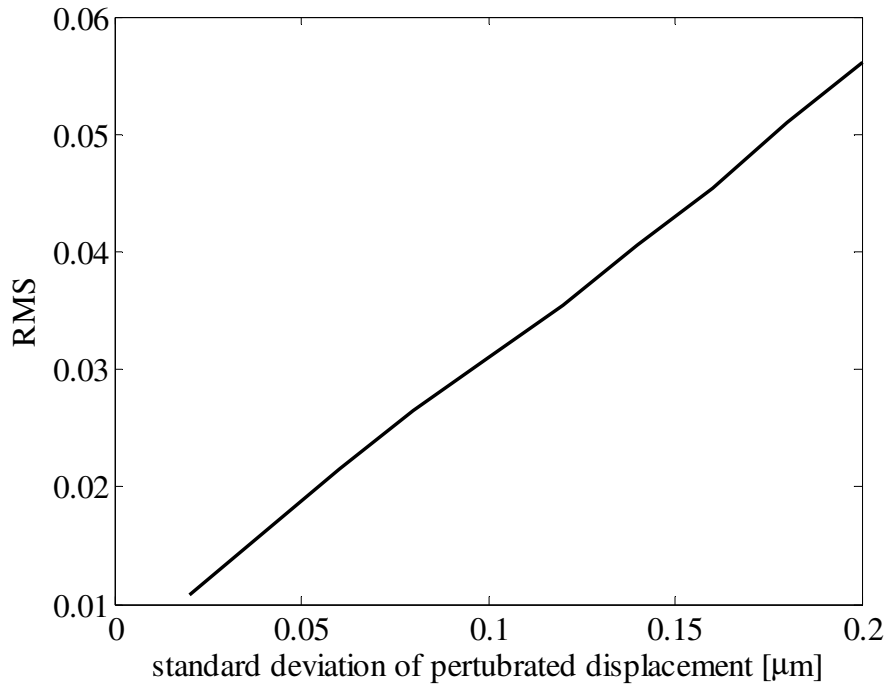


Figure 4- 16: Uncertainty measurement (RMS uncertainty) as a function of perturbed particle image displacement for Monte-Carlo simulation parameters: $d_{\tau} = 3.0$ voxel, particle density of 1.1×10^{-3} PPV, QL= 8bits/pixel, $N = 200$ and $\vec{V} = [10,0,0]$ μm/s, no noise

4.11.6 Effect of background noise

The Gaussian background noise is often observed in the experimental images due to thermal noise of the CCD, noise introduced by non-uniform laser power. In order to investigate the effect of this parameter, a Gaussian white noise with zero

mean and various standard deviations is added to the synthetic images constructing intensity volumes and the impact of noise on shape of correlation map, optimum particle diameter and particle density are studied in this section. Specifically, a normally distributed set of values is generated using a built-in MATLAB function, `imnoise`, and is then point wise added to the image data to model the effect of additive white noise.

Figure 4- 17 shows the images taken at one depth of the particle volume without and with 5% background noise for the particle image diameter of 2 voxels.

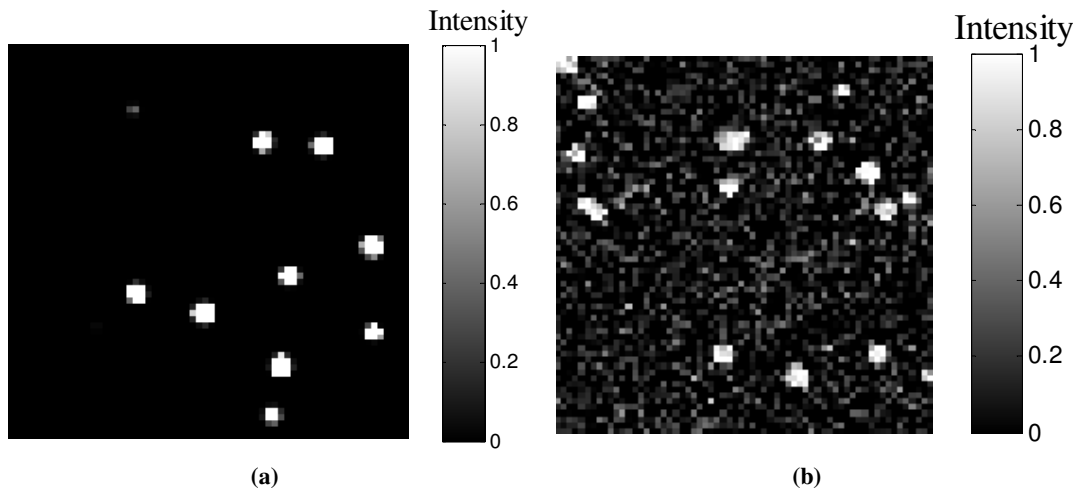


**Figure 4- 17: Synthetic images at one depth with $d_{\tau} = 2.0$ voxel (a)without noise and (b):
5% noise**

Figure 4- 18 shows a one-dimensional intensity of the synthetic images at the middle of the image for the case with/without noise in synthetic images.

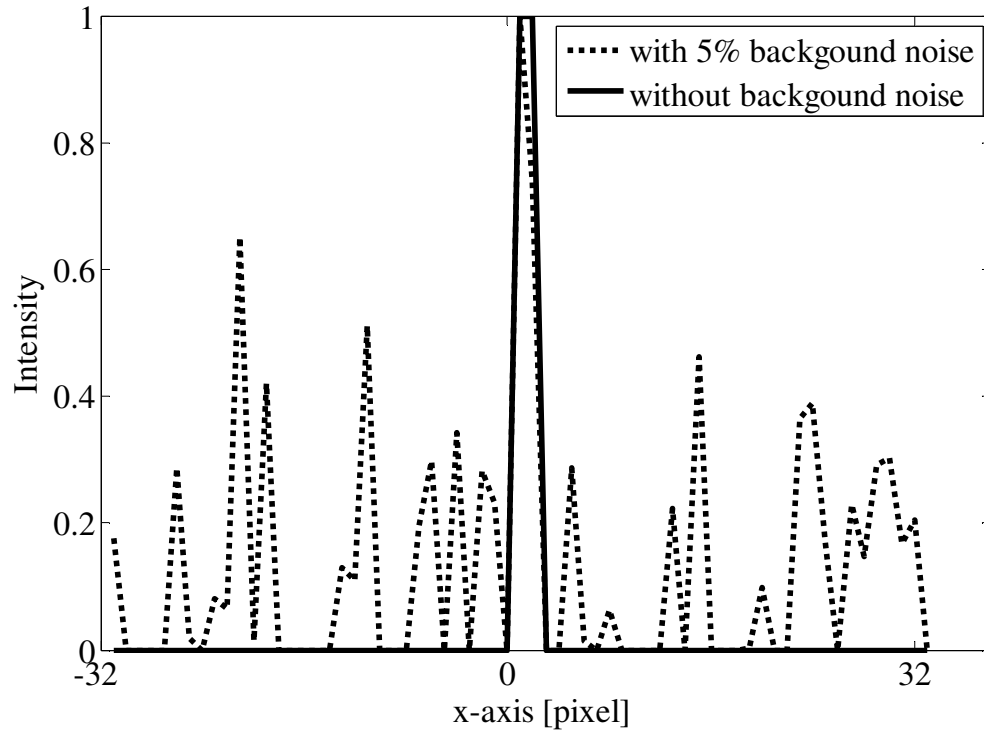


Figure 4- 18: Effect of background noise on image intensity signal along one direction for particle image size of $d_{\tau} = 2.0$ voxel positioned at the center

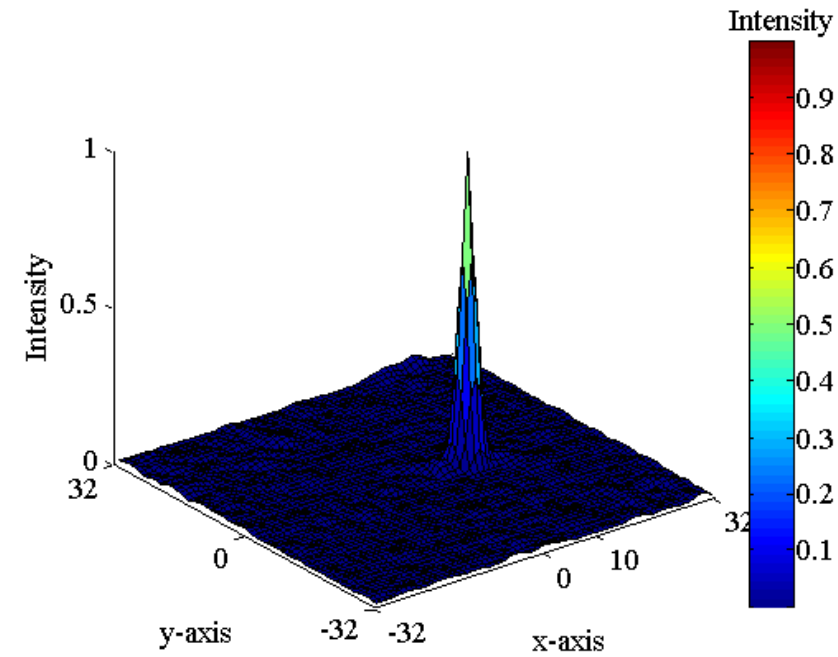
The correlation volumes in x - y plane describing with synthetic images of 0% noise and 50% noise is plotted in the Figure 4- 19. There are two significant observations from the correlation volumes; the peak height reduces in the correlation map as the level of noise increases and second, the appearance of the smaller peaks in the correlation maps. These two main observations may result in increasing the uncertainty in the velocity measurement by having a reduced prominence of the peak and potentially false peak detection if the noise is higher.

In order to explore the effect of noise on the correlation peak further, Figure 4- 20 shows the comparison of correlation maps along the x -axis with

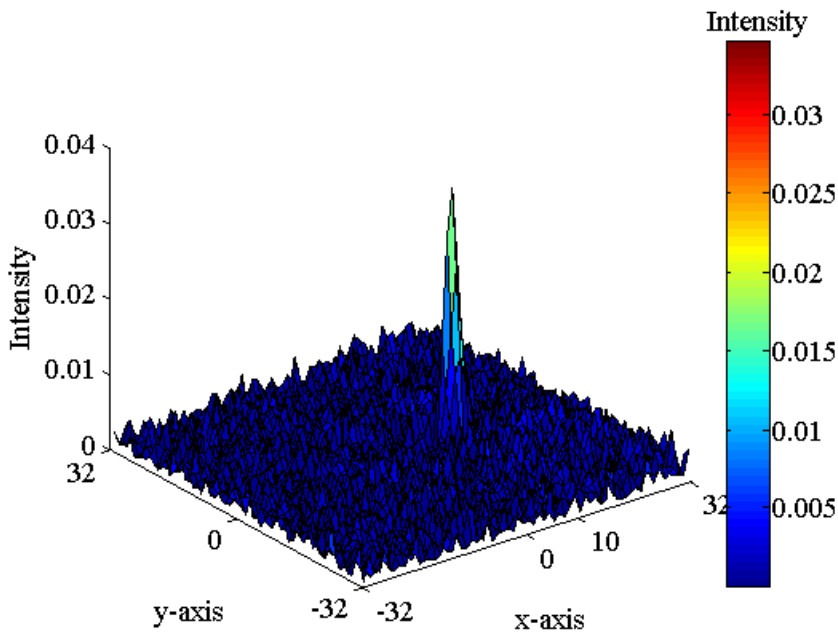
various levels of noise in the synthetic images. It is observed that the height of peak decreases as the level of noise increases. Also, images with background noises result in the increase of peak width. The calculated 50% peak width for each of the correlation maps with the calculated RMS is presented in Table 4- 1. It is clear from the table that the 50% peak width increases as the noise level increases. In addition, the effect of change in the correlation map results in increasing the uncertainty in the measurement system.

Table 4- 1: Effect of adding various noise levels to synthetic images on correlation maps ‘peak width for the simulation parameters: $N = 100$, $d_\tau = 2.0$ voxel, particle density of 1.1×10^{-3} PPV, $QL = 8$ bits/pixel and $\vec{V} = [10,0,0]$ $\mu\text{m/s}$

	0% noise	5% noise	10% noise	25% noise	50% noise
Peak width 50%	2.9941	3.0167	3.0392	3.1450	3.1779
RMS	0.0071	0.0133	0.0191	0.0422	0.0827



(a)



(b)

Figure 4- 19: Effect of adding noise to synthetic images on correlation maps in x-y plane (a): without noise (b): with 50% background noise with simulation parameters: $d_t = 2.0$ voxel, particle density of 1.1×10^{-3} PPV, QL= 8bits/pixel and $\vec{V} = [10,0,0]$ $\mu\text{m/s}$

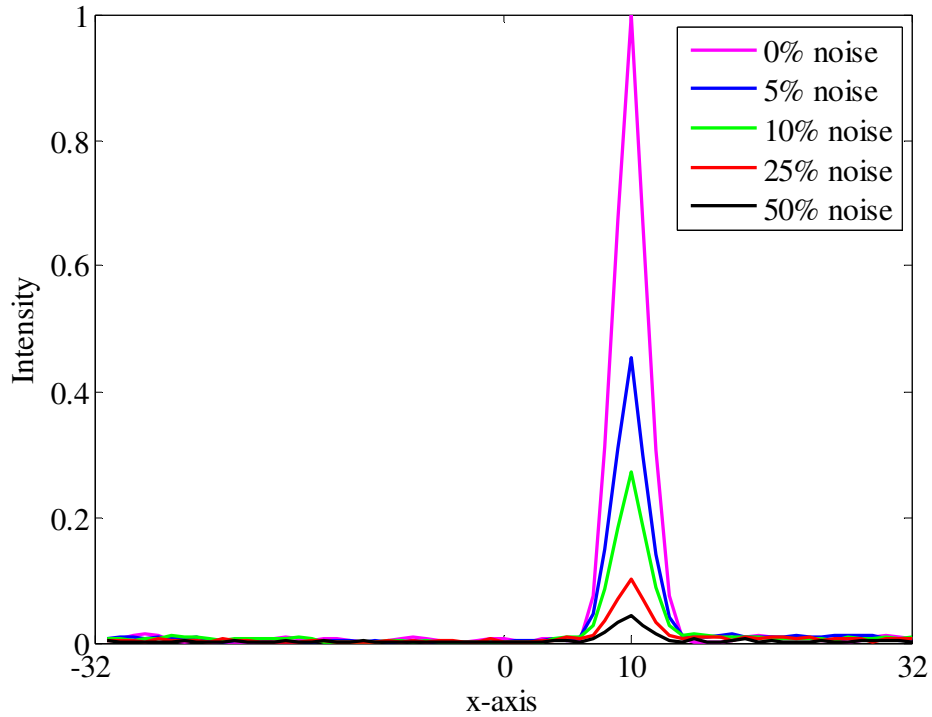


Figure 4- 20: Effect of adding various noise levels to synthetic images on correlation maps ‘peak reduction along x-axis for simulation parameters: $d_{\tau} = 2.0$ voxel, particle density of 1.1×10^{-3} PPV, QL= 8bits/pixel and $\vec{v} = [10,0,0]$ $\mu\text{m/s}$

4.11.7 Effect of noise on optimum particle diameter

Smaller size particle provides less illumination in the imaging system and if the noise added to the background of the image there is the probability of increasing unwanted signals in the image. Therefore, there is an optimum particle diameter for the level of added noise to the synthetic images. Figure 4- 21 shows the optimum diameter of the particle in the image for the different levels of noise in the synthetic images. For the image without any background noise, the optimum diameter of the particle is calculated to be around 1.5 voxels. By adding noise to

the imaging system, the optimum particle diameter increases. In addition, the level of the uncertainty in the measurement system increases for every particle size by the increase of the level of noise in the imaging system. For 5% noise added to imaging system, the particle diameter increases to 2 voxels across. The optimum particle diameter for the 10%, 25%, and 50% percent noise increases to 3 voxels, 4 voxels and 5 voxels across in particle diameter respectively.

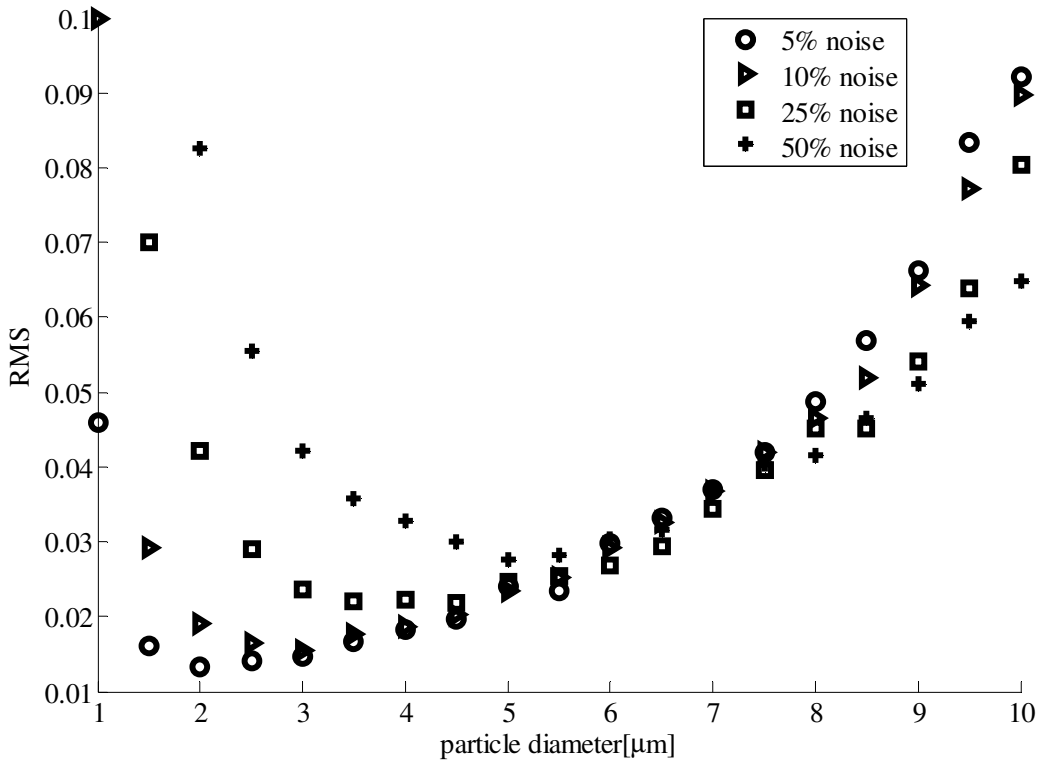


Figure 4- 21: Measurement uncertainty (RMS uncertainty) as a function of particle intensity diameter, d_{τ} , with simulation parameters: $N = 200$, particle density of 1.1×10^{-3} PPV, $QL = 8$ bits/pixel and $\vec{V} = [10, 0, 0]$ μm/s

4.11.8 Effect noise on particle density

In this section, the effect of noise in obtaining the optimum particle density is calculated. Figure 4- 22 shows the result of simulation for the particle image diameter of 2 voxels for the various levels of noise. The uncertainty of the measurement decreases as the particle density increases; however, as the level of noise added to the synthetic images increases, the uncertainty increases as well. The optimum particle density for having the uncertainty less than 0.1 is calculated to be $0.0015\mu\text{m}^{-3}$. This is equivalent to 400 particles in the $64\times 64\times 64$ voxel region of interest. Also, the scattered uncertainty at 50% case with 0.75PPV can be due to the very low signal to noise ratio occurred at low particle density and high noise.

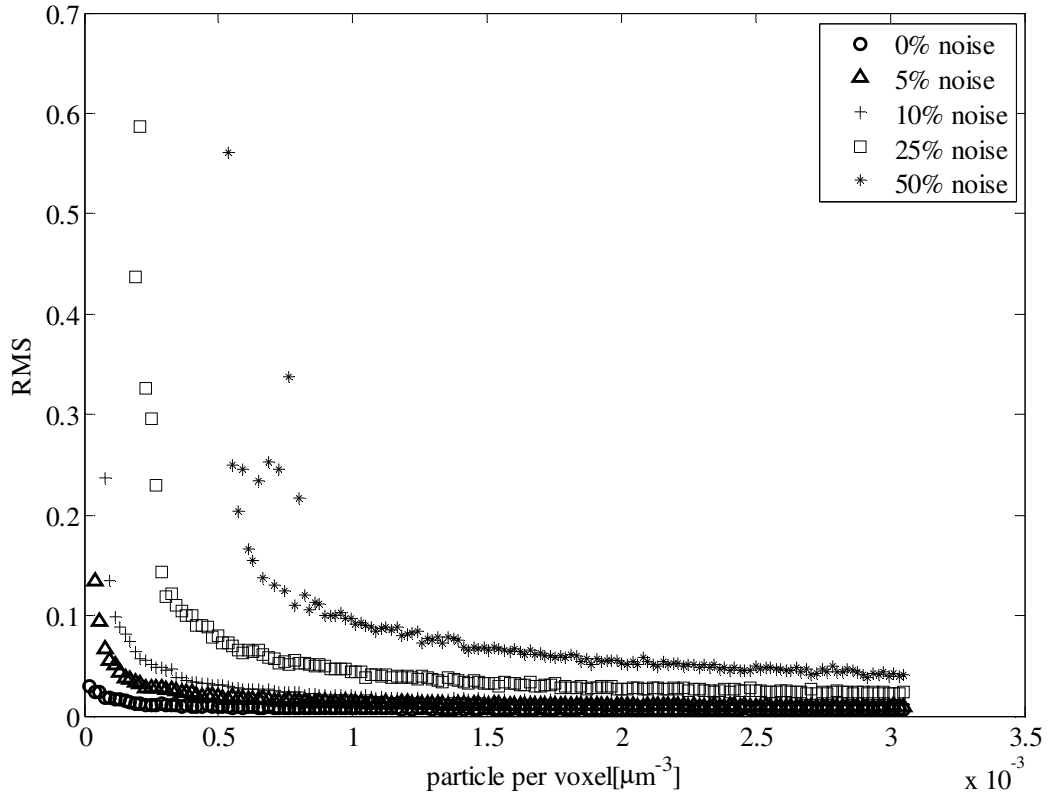


Figure 4- 22: Uncertainty measurement (RMS uncertainty) for various noise levels as a function of particle density per voxel (PPV) with the simulation parameters: $N = 200$, $d_{\tau} = 2.0$ voxel, $QL = 8$ bits/pixel and $\vec{V} = [10,0,0]$ $\mu\text{m/s}$

4.11.9 Effect of out-of-plane motion

The capability of the 3C3D measurement system in measuring the out-of-plane component of the velocity is presented in Figure 4- 23. The uncertainty of the system in measuring the out-of-plane velocity increases as the magnitude of the out-of-plane velocity increases, and almost it follows a linear trend.

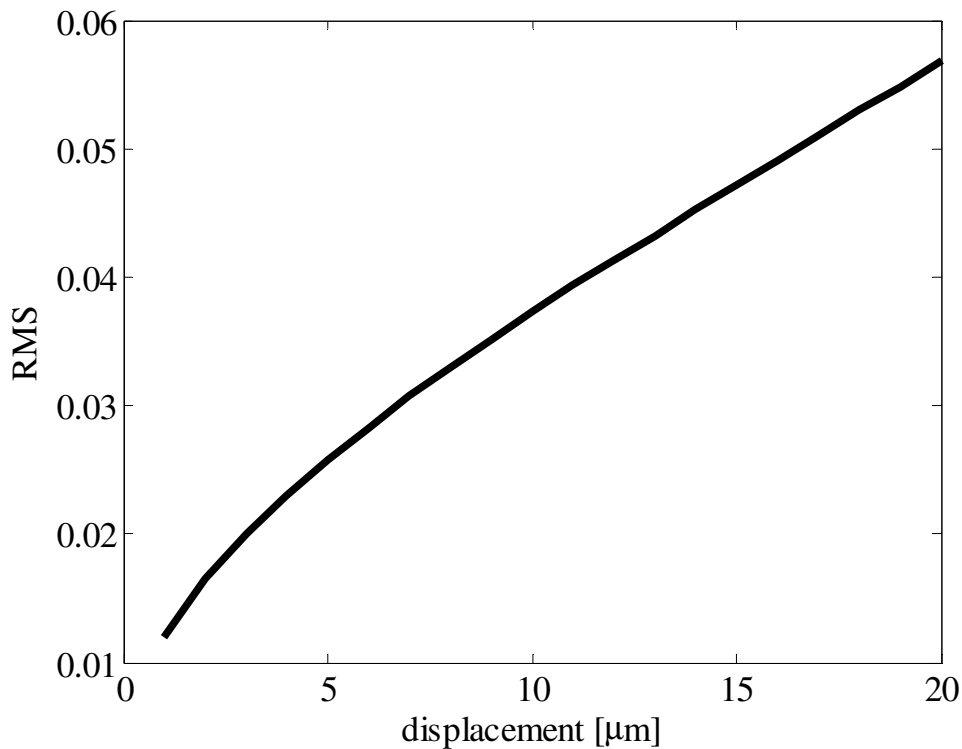


Figure 4- 23: Measurement of uncertainty (RMS uncertainty) as a function of out-of-plane displacement with Monte-Carlo simulation parameters: $N = 700$, $d_\tau = 3.0$ voxel, particle density of 1.1×10^{-3} PPV, QL= 8bits/pixel, noise 0%

Figure 4- 24 shows the effect of adding background noise in measuring the out-of-plane displacement. As the level of background noise increases, the level of uncertainty for the certain velocity increases. However, there is still a linear

relationship between measurement uncertainty and out-of-plane displacement. The further exploration about the out-of plane displacement is discussed in the future work of this study.

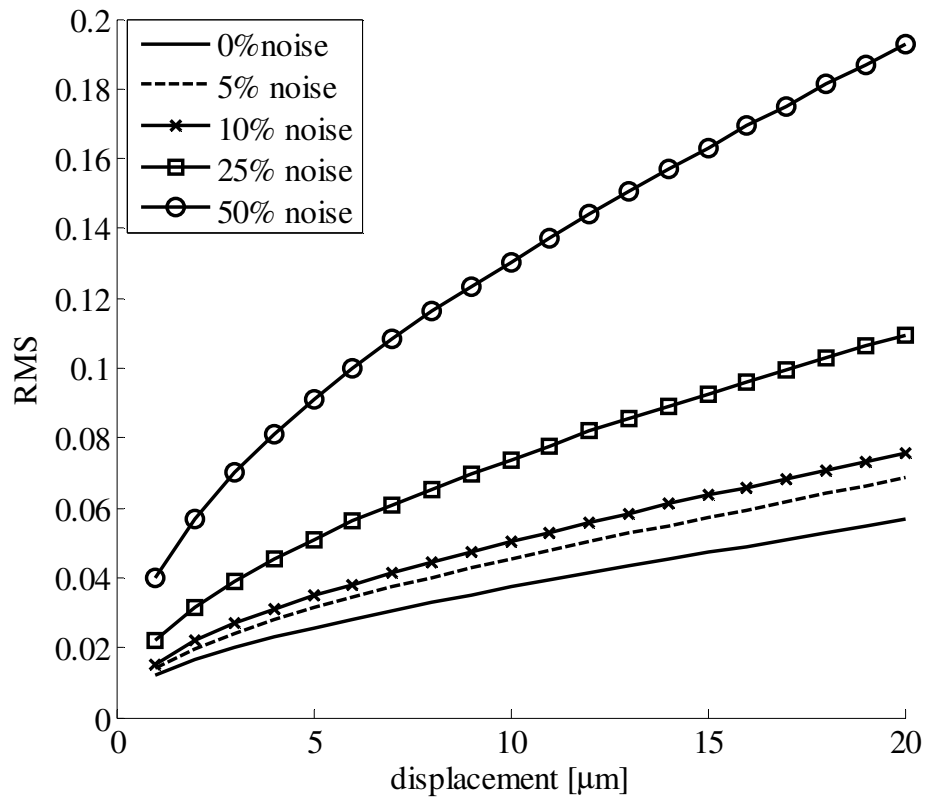


Figure 4- 24: Measurement of uncertainty (RMS uncertainty) as a function of out-of-plane displacement with Monte-Carlo simulation parameters: $N = 700$, $d_{\tau} = 3.0$ voxel, particle density of 1.1×10^{-3} PPV, QL= 8bits/pixel, noise 5%, 10%, 25%, 50%

4.12 Conclusions

In this study, a validation towards development of a three-dimensional three-component (3C3D) particle velocity measurement system in determining micro flow field velocity vectors based on computational perturbation Monte-Carlo simulation was performed. The 3C3D technique is based on 3D cross correlation of the volume of intensities of seeded particles in the flow field at a unit time interval. Important aspects of how the experimental technique captures particles intensity volumes are explored. In the experiment, the intensity volumes are built by capturing images of flow field at discrete channel depths using a scanning system and stacking the images together. Each seeded fluorescent particle has a 3D Gaussian intensity that constructs the intensity volume when scanning along the depth, such that the constructed intensity volume of a particle appears as a rod of illumination.

In order to investigate the effect of stretched intensities of the semi-spherical particles in 3C3D measurement, two types of particle intensities: 3D Gaussian spherical and 2D Gaussian cylindrical for two types of uniform in-plane and out-of-plane flow fields were simulated using synthetic images. The correlation maps of the cylindrical cases were observed to be stretched in out-of-plane direction in contrast to the spherical case. Furthermore, a comparison between the flow field with seeded spherical, cylindrical and 3D Gaussian intensities demonstrated that correlation maps are elongated in the direction of the

stretched illuminated light. For the case of the Gaussian intensity particles, it is volumetrically stretched, however, the peak location for all three types of particles is the same and it is equal to the flow field displacement.

A Monte-Carlo analysis for studying the effect of particle density on measurement uncertainty (RMS) for both types of in-plane and out-of-plane flow fields using 3D Gaussian intensity particles was simulated. The measurement uncertainty was calculated through investigating the effect of the parameters of the study including particle diameter, seeding density, input velocity perturbation and out-of-plane displacement, as well as the background white noise in the synthetic images in calculating the velocity vector field. There is an optimum particle diameter for having the minimum measurement uncertainty for a fixed seeding density. By adding background noise, this optimum particle diameter for the same amount of seeding density increases. Also, the level of uncertainty increases as the percentage of background noise increases. There is also a minimum particle density for a fixed particle diameter that the uncertainty remains plateau. As the background noise is added to the system, the minimum particle density per voxel for a fixed particle diameter increases. There was a linear relationship between the measurement uncertainty and out-of-plane displacement. As the out-of-plane velocity increases the uncertainty of the measurement system increases linearly. Also, adding the background noise to the out-of-plane velocity measurement causes to the increase in the measurement uncertainty. There exist several other parameters that may affect the measurement

uncertainty that can be studied in the future investigations. This chapter opens a window in using Monte-Carlo simulation and applying the developed 3D cross correlation and volumetric peak detection to determine the velocity vectors in the proposed 3C3D velocity measurement system.

CHAPTER 5: Conclusions and Future Work

An assessment of a micro-fluidic measurement technique capable of measuring three components of the velocity in the micro-channel has been developed in this study. In the measurement system, a high speed CCD camera takes slices of planar (x,y) images in the micro channel while a piezoelectric scans the focal plane with an infinity corrected objective through the volume in the z -direction. The time series data set constructs individual scanned intensity volumes which are cross-correlated using a 3D algorithm. This leads to obtaining a near instantaneous three-dimensional velocity vector field. A benefit of this approach is that a large number of velocity vectors are generated to define the flow motion in comparison to the defocusing or off-focus methods.

The scanning 3C3D technique has been used to obtain the 3D velocity vector of flow in micro-channel including mixing flow, flow in porous media and segmented flow. The experiments demonstrated a highly 3D motion of gas-bubble segmented flow, streaklines of fluid flow in mixing chamber and the 3D flow field between glass beads in porous media flow. Using 3C3D measurement system highlights the potential of measuring 3D micro-flow fields; however, using the scanning 3C3D measurement system introduces challenges and uncertainty that are unique to this particular approach.

The measurement uncertainty and dynamic range of 3D velocity vector depends on the experiments' conditions, experimental set-up and processing algorithm. That includes effects from the fluorescent particle size, depth of focus

of the system optics, frame rate of the single CCD detector, camera pixel size, and the scan rate and number of the image slices of the piezo-electric scanning system. Using fluorescent particles in micro-flow field introduces some uncertainty to the measurement due to colloidal particle dynamics in micro-flow that includes Brownian motion of the particles, particle lag factor, and particle acceleration. As the particle size becomes smaller the effect of Brownian motion increases which this uncertainty depends on particle's diffusion coefficient, time scale of the experiment reversely, and number of the particles averaged in interrogation volume. Particle lag factor determines how quickly the particle responds to flow changes and it defines by particle relaxation time that varies proportional to particle diameter and density and inversely to fluid viscosity. The smaller the relaxation time, the quicker the particle responds to the fluid flow changes.

The experimental equipment introduce some uncertainties to the measurement due to the accuracy of the measurement system's set-up including CCD camera, piezo electric stage, CW laser and optic of the system. The parameters involved in measurement uncertainty using a CCD camera contains camera pixel size, exposure time, and frame rate. Image pixilation occurs due to a finite camera pixel size by digitizing the continuous signal of the particles. This limits the accuracy of the measurement system in determining the center of particle image. The imaging exposure time has a direct effect on camera frame

rate. The higher the camera frame rate reflects directly on the frequency of imaging, the higher the maximum measurable flow rate.

A significant effect of piezo-electric stage in 3C3D measurement uncertainty is the number of the image slices in depth that acquired by piezo electric system scanning in the depth of the channel. This determines the spatial resolution of measuring the out-of-plane displacement of flow field. The higher number of slices results in reducing the spatial distance between two subsequent slices and consequently increases the spatial resolution of the system in depth.

The 3C3D technique is based on a 3D cross correlation of the volume of intensities of seeded particles in the flow field at a known time interval. The intensity volumes are built by capturing images of flow field at discrete channel depths using a scanning system and stacking the images together. Each seeded fluorescent particle has a 3D Gaussian intensity that constructs the intensity volume when scanning along the depth, such that the constructed intensity volume of a particle appears as a rod of illumination. In order to investigate the effect of the shape of intensity particles in the proposed 3C3D measurement, two types of particle intensities: 3D Gaussian spherical and 2D Gaussian cylindrical particles are simulated using synthetic images. The correlation maps of the cylindrical cases are observed to be stretched in out-of-plane direction in contrast to the spherical case. This is due to stretched intensity of cylindrical particles along out-of-plane direction. This observation was also compared to the correlation map obtained from the flow field seeded by 3D Gaussian particles that the correlation

maps stretched in three dimensional and along the direction that the Gaussian intensity of the particle is stretched.

The calculated displacement accuracy is also dependent on the correlated intensity images or volumes including image background noise, pixel resolution, and cross correlation algorithm. In order to investigate the effect of the related experimental parameters in 3C3D velocity measurement, a Monte-Carlo analysis was performed and the measurement uncertainty (RMS) was calculated.

Investigating the effect of particle diameters on the measurement uncertainty showed that there is an optimum particle diameter for fixed particle's densities. This diameter is estimated to be between 1.5-2 voxels across and by adding noise to the synthetic images, the optimum tracer particle's diameter increases along with the increase in the level of uncertainty. The minimum required particle density for a fixed diameter of the seeded particles is calculated to be 0.001 #/voxel (300 particles in $64 \times 64 \times 64$ voxel) that the measurement uncertainty remains plateau to less than 0.01 and as the introduced noise to the synthetic images increases the level of particle's density for a uniform uncertainty increases. It is also observed that the level of uncertainty of the measurement system decreases by adding noise to the synthetic images. Studying the correlation maps of the intensity volumes with and without adding noise shows that the correlation peak decreases as the level of noise increases and small peaks appear in the correlation maps; this might be the reason of the increased uncertainty in the measurement system after adding noise to the synthetic images.

The nature of particle based measurement techniques including the scanning 3C3D measurement system is stochastic. Therefore, an investigation based on perturbation of displacement of individual particle in the synthetic images is performed such that the mean displacement of each particle is equal to the bulk flow field displacement and various standard deviations. The results of this study showed that there is a linear relation between the standard deviation of displacement of seeded particles and uncertainty of the measurement system. However, the slope of the increase of the uncertainty is 25% of the increase in standard deviation of the particles' displacement.

Another significant investigation was studying the uncertainty of the system in measuring the out-of-plane displacement. It was observed that uncertainty increased with the ratio of 0.25% as the out-of-plane displacement increases. It was also observed that as the background noise is added to the scanned images, the level of uncertainty in the measurement increases. However, the relationship between uncertainty and out-of-plane displacement remains linear.

It was observed that the measurement system dynamic spatial resolution is the image pixel size for in-plane and the spatial distance between two successive slices built the intensity volumes in out-of-plane displacement's calculation. Dynamic velocity range of the system for measuring the maximum in-plane and out-of-plane displacement is limited to the displacement of the particle across the interrogation window size in planar and depth direction respectively.

5.1 Future work

The validation of the scanning 3C3D velocity measurement technique is completed by obtaining the velocity profile of the various flow fields for example by investigating a Couette flow, parabolic flow and shear flow using synthetic images. In addition, the processing algorithm can be investigated further by studying the effect of changing the interrogation window size of the synthetic images and study several other dependent parameters.

Finally, there is a distortion in the correlation time between two constructed intensity volumes. This is due to the fact that each intensity volume is built through scanning along depth and there is an accumulating time difference between successive slices related to the scanning rate. The time between adjacent slices is related to the scanning rate. Therefore, another significant enhancement in the simulation would be investigating the relative scanning rate to the out-of-plane flow motion.

REFERENCE LIST

- [1] H. Chen and J.-C. Meiners, "Topologic mixing on a microfluidic chip," *Applied Physics Letters*, vol. 84, no. 12, pp. 2193-5, 2004.
- [2] S. Molla and S. Bhattacharjee, "Dielectrophoretic levitation in the presence of shear flow: implications for colloidal fouling of filtration membranes.," *Langmuir: the ACS journal of surfaces and colloids*, vol. 23, no. 21, pp. 10618-27, Oct. 2007.
- [3] D. S. Nobes, M. Abdolrazaghi, and S. Mitra, "Image-Based Photonic Techniques for Microfluidics," in *Microfluidics and Nanofluidics Handbook*, S. Mitra and S. K. Chakraborty, Eds. CRC Press, 2011, pp. 1-52.
- [4] C. Kleinstreuer, *Modern Fluid Dynamics*, vol. 87. Dordrecht: Springer Netherlands, 2009.
- [5] Y. K. Morishima K., Fukuda T., Arai F., "Microflow system and transportation of DNA molecule by dielectrophoretic force utilizing the conformational transition in the higher order structure of DNA molecule," *Proceedings of the IEEE Tenth Annual International Workshop on Micro Electro Mechanical Systems*, pp. 5-10, 1997.
- [6] Santiago, S. T. Wereley, C. D. Meinhart, D. J. Beebe, and R. J. Adrian, "A particle image velocimetry system for microfluidics," *Experiments in Fluids*, vol. 25, no. 4, pp. 316-319, Sep. 1998.
- [7] Meinhart, S. Wereley, and J. Santiago, "PIV measurements of a microchannel flow," *Experiments in Fluids*, vol. 27, no. 5, pp. 414-419, Oct. 1999.
- [8] R. Lindken, J. Westerweel, and B. Wieneke, "Stereoscopic micro particle image velocimetry," *Experiments in Fluids*, vol. 41, no. 2, pp. 161-171, May 2006.
- [9] S. Y. Yoon and K. C. Kim, "3D particle position and 3D velocity field measurement in a microvolume via the defocusing concept," *Measurement Science and Technology*, vol. 17, no. 11, pp. 2897-2905, Nov. 2006.

- [10] M. Speidel, A. Jonás, and E.-L. Florin, "Three-dimensional tracking of fluorescent nanoparticles with subnanometer precision by use of off-focus imaging.," *Optics letters*, vol. 28, no. 2, pp. 69-71, Jan. 2003.
- [11] N. J. Lawson and J. Wu, "Three-dimensional particle image velocimetry : experimental error analysis of a digital angular stereoscopic system," *Victoria*, vol. 1455, 1997.
- [12] C. E. Willert and M. Gharib, "Three-dimensional particle imaging with a single camera," *Experiments in Fluids*, vol. 12, no. 6, pp. 353-358, 1992.
- [13] Wu, J. W. Roberts, and M. Buckley, "Three-dimensional fluorescent particle tracking at micron-scale using a single camera," *Experiments in Fluids*, vol. 38, no. 4, pp. 461-465, Feb. 2005.
- [14] R. Luo, X. Y. Yang, X. F. Peng, and Y. F. Sun, "Three-dimensional tracking of fluorescent particles applied to micro-fluidic measurements," *Journal of Micromechanics and Microengineering*, vol. 16, no. 8, pp. 1689-1699, Aug. 2006.
- [15] A. Ould, E. Moctar, N. Aubry, J. Batton, R. June, and A. September, "Electro-hydrodynamic micro-fluidic mixer," *Mechanical Engineering*, no. September, pp. 273-280, 2003.
- [16] Z. Yang, H. Goto, M. Matsumoto, and R. Maeda, "Ultrasonic micromixer for microfluidic systems," *Proceedings IEEE Thirteenth Annual International Conference on Micro Electro Mechanical Systems Cat No00CH36308*, vol. 93, no. 3, pp. 80-85, 2001.
- [17] H. H. Bau, J. Zhong, and M. Yi, "A minute magneto hydro dynamic (MHD) mixer," *Sensors and Actuators B: Chemical*, vol. 79, no. 2-3, pp. 207-215, 2001.
- [18] I. Glasgow and N. Aubry, "Enhancement of microfluidic mixing using time pulsing.," *Lab on a Chip*, vol. 3, no. 2, pp. 114-120, 2003.
- [19] W. Ehrfeld, K. Golbig, V. Hessel, H. Löwe, and T. Richter, "Characterization of Mixing in Micromixers by a Test Reaction: Single Mixing Units and Mixer Arrays," *Industrial & Engineering Chemistry Research*, vol. 38, no. 3, pp. 1075-1082, 1999.

- [20] C.-C. Hong, J.-W. Choi, and C. H. Ahn, "A novel in-plane passive microfluidic mixer with modified Tesla structures.," *Lab on a Chip*, vol. 4, no. 2, pp. 109-113, 2004.
- [21] Y.-C. Chung, Y.-L. Hsu, C.-P. Jen, M.-C. Lu, and Y.-C. Lin, "Design of passive mixers utilizing microfluidic self-circulation in the mixing chamber.," *Lab on a Chip*, vol. 4, no. 1, pp. 70-77, 2004.
- [22] J. Melin, G. Giménez, N. Roxhed, W. Van Der Wijngaart, and G. Stemme, "A fast passive and planar liquid sample micromixer.," *Lab on a Chip*, vol. 4, no. 3, pp. 214-219, 2004.
- [23] Y. T. Chew, H. M. Xia, C. Shu, and S. Y. M. Wan, "Techniques to enhance fluid micro-mixing and chaotic micromixers," *Modern Physics Letters*, vol. 19, no. 28-29, pp. 1567-1570, 2005.
- [24] A. Günther, S. A. Khan, M. Thalmann, F. Trachsel, and K. F. Jensen, "Transport and reaction in microscale segmented gas-liquid flow.," *Lab on a Chip*, vol. 4, no. 4, pp. 278-286, 2004.
- [25] J. M. Macinnes, A. Vikhansky, and R. W. K. Allen, "Numerical characterisation of folding flow microchannel mixers," *Chemical Engineering Science*, vol. 62, no. 10, pp. 2718-2727, 2007.
- [26] D. S. Nobes, M. Abdolrazaghi, and D. L. N. Homeniuk, "Three-component , three-dimensional velocity measurement technique for micro- channel applications using a scanning μ PIV," in *15th Int Symp on Applications of Laser Techniques to Fluid Mechanics*, 2010.
- [27] T. Cubaud and C.-M. Ho, "Transport of bubbles in square microchannels," *Physics of Fluids*, vol. 16, no. 12, p. 4575, 2004.
- [28] N.-T. Nguyen and S. T. Wereley, *Fundamentals and applications of MicroFluids*, 2nd ed. Norwood: ARTECH House Inc., 2006.
- [29] D. R. Link, S. L. Anna, D. A. Weitz, and H. A. Stone, "Geometrically mediated breakup of drops in microfluidic devices.," *Physical Review Letters*, vol. 92, no. 5, p. 054503, 2004.
- [30] J. J. Heras, A. J. Sederman, and L. F. Gladden, "Ultrafast velocity imaging of single- and two-phase flows in a ceramic monolith.," *Magnetic Resonance Imaging*, vol. 23, no. 2, pp. 387-389, 2005.

- [31] S. Waelchli and P. Rudolfvonrohr, "Two-phase flow characteristics in gas-liquid microreactors," *International Journal of Multiphase Flow*, vol. 32, no. 7, pp. 791-806, 2006.
- [32] M. A. Le Gros, G. McDermott, and C. A. Larabell, "X-ray tomography of whole cells.," *Current Opinion in Structural Biology*, vol. 15, no. 5, pp. 593-600, 2005.
- [33] N. De Mas, A. Günther, T. Kraus, M. A. Schmidt, and K. F. Jensen, "Scaled-Out Multilayer Gas-Liquid Microreactor with Integrated Velocimetry Sensors," *Industrial & Engineering Chemistry Research*, vol. 44, no. 24, pp. 8997-9013, 2005.
- [34] T. Kraus, A. Gnther, N. De Mas, M. A. Schmidt, and K. F. Jensen, "An integrated multiphase flow sensor for microchannels," *Experiments in Fluids*, vol. 36, no. 6, pp. 819-832, 2004.
- [35] A. Günther and K. F. Jensen, "Multiphase microfluidics: from flow characteristics to chemical and materials synthesis.," *Lab on a Chip*, vol. 6, no. 12, pp. 1487-1503, 2006.
- [36] M. Abdolrazaghi and D. S. Nobes, "Investigation of the 3D Velocity field of a segmented flow utilizing a novel 3C3D micro-PIV approach," in *International Mechanical Engineering Congress and Exposition , IMECE2010-38710*, 2010, pp. 2-6.
- [37] N. J. Hadia, L. S. Chaudhari, S. K. Mitra, M. Vinjamur, and R. Singh, "Experimental investigation of use of horizontal wells in waterflooding," *Journal of Petroleum Science and Engineering*, vol. 56, no. 4, pp. 303-310, 2007.
- [38] D. Sen, D. S. Nobes, and S. K. Mitra, "Optical measurement of pore scale velocity field inside microporous media," *Microfluidics and Nanofluidics*, 2011.
- [39] M. Sen D., Abdolrazaghi and S. Nobes, D., Mitra, "Investigation of interstitial velocity field inside micro-porous media," in *International Mechanical Engineering Congress and Exposition , IMECE2010-38347*, 2010, pp. 1-6.
- [40] B. N. Taylor and C. E. Kuyatt, *Guidelines for Evaluating and Expressing the Uncertainty of NIST Measurement Results (rev*, vol. 12972nded, no. 1297. DIANE Publishing, 1994, p. 2.

- [41] G. E. Elsinga, F. Scarano, B. Wieneke, and B. W. Oudheusden, "Tomographic particle image velocimetry," *Experiments in Fluids*, vol. 41, no. 6, pp. 933-947, Oct. 2006.
- [42] A. Fouras, D. Lo Jacono, C. V. Nguyen, and K. Hourigan, "Volumetric correlation PIV: a new technique for 3D velocity vector field measurement," *Experiments in Fluids*, vol. 47, no. 4-5, pp. 569-577, Feb. 2009.
- [43] S. M. Pommer, R. A. Kieh, G. Soni, S. N. Dakessian, and D. C. Meinhart, "A 3D-3C Micro-PIV Method," *2007 2nd IEEE International Conference on Nano/Micro Engineered and Molecular Systems*, pp. 1196-1201, Jan. 2007.
- [44] K. Shinohara, Y. Sugii, J. H. Jeong, and K. Okamoto, "Development of a three-dimensional scanning microparticle image velocimetry system using a piezo actuator," *Review of Scientific Instruments*, vol. 76, no. 10, p. 106109, 2005.
- [45] G. Recktenwald, "Uncertainty Estimation and Calculation Phases of an Experiment," 2006.
- [46] J. H. Masliyah and S. Bhattacharjee, "Electrokinetic and colloid transport phenomena electrokinetic and colloid transport," *Cell*, 2005.
- [47] S. Habicht, R. J. Nemanich, and a Gruverman, "Physical adsorption on ferroelectric surfaces: photoinduced and thermal effects," *Nanotechnology*, vol. 19, no. 49, p. 495303, Dec. 2008.
- [48] N. Al Quddus, W. a Moussa, and S. Bhattacharjee, "Motion of a spherical particle in a cylindrical channel using arbitrary Lagrangian-Eulerian method.," *Journal of colloid and interface science*, vol. 317, no. 2, pp. 620-30, Jan. 2008.
- [49] R. J. Adrian and J. Westerweel, *Particle Image Velocimetry*. Cambridge University Press, 2010, p. 558.
- [50] M. For and G. Vision, "User's Manual for GigE Vision Cameras, Basler pilot," 2008.
- [51] M. Olsen and R. J. Adrian, "Out-of-focus effects on particle image visibility and correlation in microscopic particle image velocimetry," *Exp Fluid*, vol. 29, pp. 166-174.

- [52] R. Adrian and C. Yao, "Pulsed laser technique application to liquid and gaseous flows and the scattering power of seed materials," *Appl Optics*, vol. 24, pp. 42–52, 1985.
- [53] R. Lindken, M. Rossi, S. Grosse, and J. Westerweel, "Micro-Particle Image Velocimetry (microPIV): recent developments, applications, and guidelines.," *Lab on a chip*, vol. 9, no. 17, pp. 2551-67, Sep. 2009.
- [54] J. Raffel, M., Willert, C.E., Wereley, S.T., Kompenhans, *Particle image velocimetry: A practical Guide*. 2007.
- [55] H. Nobach and M. Honkanen, "Two-dimensional Gaussian regression for sub-pixel displacement estimation in particle image velocimetry or particle position estimation in particle tracking velocimetry," *Experiments in Fluids*, vol. 38, no. 4, pp. 511-515, Mar. 2005.

APPENDIX A

3D Normalized cross correlation source code in MATLAB:

```
function I_NCC = normxcorr3(varargin)
% This work is an extended version of the normalized 2D cross-
% correlation MATLAB (The MathWorks Inc., Natick, Massachusetts)
% algorithm "normxcorr2" based on
%
% "Fast Normalized Cross-Correlation", by J. P. Lewis, Industrial
% Light &
% Magic. http://www.idiom.com/~zilla/Papers/nvisionInterface/nip.html
% Haralick, Robert M., and Linda G. Shapiro, Computer and Robot
% Vision, Volume II, Addison-Wesley, 1992, pp. 316-317.
%
% Author: Mona Abdolrazaghi
% Email: mona.abdolrazaghi@gmail.com

%NORMXCORR3 Normalized three-dimensional cross-correlation.
% C = NORMXCORR3(TEMPLATE,A) computes the 3D normalized cross-
% correlation of
% matrices TEMPLATE and A. The matrix A must be larger than the
% matrix
% TEMPLATE for the normalization to be meaningful. The values
% of TEMPLATE
% cannot all be the same. The resulting matrix C contains
% correlation
% coefficients and its values may range from -1.0 to 1.0.
%
% Class Support
% -----
% The input matrices can be numeric. The output matrix C is
% double.
%
% Input-output specs
% -----
% T: 3-D, real, full matrix
%    logical, uint8, uint16, or double
%    no NaNs, no Infs
%    prod(size(T)) >= 3
%    std(T(:))~0
%
% A: 3-D, real, full matrix
%    logical, uint8, uint16, or double
%    no NaNs, no Infs
%    size(A,1) >= size(T,1)
%    size(A,2) >= size(T,2)
%    size(A,3) >= size(T,3)
% C: double

[T, A] = ParseInputs(varargin{:});
% T=Intensity_flow_scan1;
```

```

% A=Intensity_flow_scan2;

%
xcorr_TA = xcorr3_fast(T,A);
%Icorr=xcorr_TA;

[m n p] = size(T);
mnp = m*n*p;

local_sum_A = local_sum(A,m,n,p);
%Idata.LocalSumI=local_sum_A;

local_sum_A2 = local_sum(A.*A,m,n,p);

% Note: diff_local_sums should be nonnegative, but may have
negative
% values due to round off errors. Below, we use max to ensure the
% radicand is nonnegative.
diff_local_sums = ( local_sum_A2 - (local_sum_A.^2)/mnp );
%Idata.stdI=diff_local_sums;

denom_A = sqrt( max(diff_local_sums,0) );

denom_T = sqrt(mnp-1)*std(T(:));%STD T
denom = denom_T*denom_A;
numerator = abs((xcorr_TA - local_sum_A*sum(T(:))/mnp
));%considering the absolute value in order to obtain the
positive part only.

% We know denom_T~=0 from input parsing;
% so denom is only zero where denom_A is zero, and in
% these locations, C is also zero.
C = zeros(size(numerator));
tol = 1000*eps( max(abs(denom(:))) );%Floating-point relative
accuracy
i_nonzero = find(denom > tol);
C(i_nonzero) = numerator(i_nonzero) ./ denom(i_nonzero);
% Remove padding
I_NCC=unpadarray(C, size(A));

%-----
% Function local_sum
%
function local_sum_A = local_sum(A,m,n,p)

B = padarray(A,[m n p]);%make the size of B the same size of A
and zeros at the beginning
%B=A;

```

```

s = cumsum(B,1);%returns the cumulative sum along different
dimensions of an array, 1= column

c = s(1+m:end-1, :, :)-s(1:end-m-1, :, :);

s = cumsum(c,2);
c = s(:, 1+n:end-1, :)-s(:, 1:end-n-1, :);

s = cumsum(c,3);
local_sum_A = s(:, :, 1+p:end-1)-s(:, :, 1:end-p-1);

%-----
% Function  xcorr3_fast
%
function cross_corr = xcorr3_fast(T,A)

T_size = size(T);
A_size = size(A);
outside = A_size + T_size - 1;

%figure out when to use spatial domain vs. freq domain
%conv_time = time_conv3(T_size,A_size); % 1 conv2
%fft_time = 3*time_fft3(outside); % 2 fft2 + 1 ifft2

%if (conv_time < fft_time)
    % cross_corr = conv(conj(T),A);
%else
    cross_corr = freqxcorr(T,A,outside);
%end

%-----
% Function  freqxcorr
%
function xcorr_ab = freqxcorr(a,b,outsize)
Fa=fftn(rot90_3D(a), [outsize(1), outsize(2), outsize(3)]);%(rot90(a
,2));%, outsize(1), outsize(2));
    Fb = fftn(b, [outsize(1), outsize(2), outsize(3)]);
xcorr_ab = real(ifftn(Fa .* Fb));

function [T, A] = ParseInputs(varargin)
%
    iptchecknargin(2,2,nargin,mfilename)%Check number of input
arguments;
                                %iptchecknargin(low, high,
num_inputs, func_name)
%
    T = varargin{1};%first Matrix
    A = varargin{2};%second matrix
%
```

```

iptcheckinput(T,{'logical','numeric'},{'real','nonsparse','3d','finite'},mfilename,'T',1)

iptcheckinput(A,{'logical','numeric'},{'real','nonsparse','3d','finite'},mfilename,'A',2)
%
    checkSizesTandA(T,A)
%
% % See geck 342320. If either A or T has a minimum value which
% % need to shift the array so all values are positive to ensure
% % numerically
% % robust results for the normalized cross-correlation.
    A = shiftData(A);
    T = shiftData(T);
%
    checkIfFlat(T);

%-----
-----
function B = shiftData(A)

B = double(A);

is_unsigned = isa(A,'uint8') || isa(A,'uint16') ||
isa(A,'uint32');
if ~is_unsigned

    min_B = min(B(:));

    if min_B < 0
        B = B - min_B;
    end

end

%-----
-----
function checkSizesTandA(T,A)

if numel(T) < 3
    eid = sprintf('Images:%s:invalidTemplate',mfilename);
    msg = 'TEMPLATE must contain at least 2 elements.';
    error(eid,'%s',msg);
end

if size(A,1)<size(T,1) || size(A,2)<size(T,2)
    eid = sprintf('Images:%s:invalidSizeForA',mfilename);
    msg = 'A must be the same size or larger than TEMPLATE.';
    error(eid,'%s',msg);
end

```

```

end

%-----
-----
function checkIfFlat(T)

if std(T(:)) == 0
    eid = sprintf('Images:%s:sameElementsInTemplate',mfilename);
    msg = 'The values of TEMPLATE cannot all be the same.';
    error(eid, '%s', msg);
end
%-----
-----

function B=unpadarray(A,Bsize)
Bstart=ceil((size(A)-Bsize)/2)+1;
Bend=Bstart+Bsize-1;
if(ndims(A)==2)
    B=A(Bstart(1):Bend(1),Bstart(2):Bend(2));
elseif(ndims(A)==3)
    B=A(Bstart(1):Bend(1),Bstart(2):Bend(2),Bstart(3):Bend(3));
end

%_____
_____
function T=rot90_3D(T)
T=flipdim(flipdim(flipdim(T,1),2),3);

```